

Non-Linear Finite Element Analysis and Parametric Study of Four-Pile Pile Caps

Selam Getahun Asefa
August, 2020

Non-linear finite element analysis and parametric study of four-pile pile caps

A thesis submitted to the Delft University of Technology in partial fulfillment of the requirements for the degree of

Master of Science in Structural Engineering

by

Selam Asefa

August 2020

Supervisors:	Dr. Ir. Max Hendriks	Chair of the Committee
	Dr. Ir. Lex van der Meer	Daily Supervisor
	Dr. Ir. Pierre Hoogenboom	Supervisor
	Dr. Ir. Eva Lantsoght	Supervisor

Preface

This thesis project is part of my 2 years master program in civil engineering at Delft University of Technology. The past two years have been challenging and rewarding both academically and personally. The experience has pushed me to strive to overcome my self-doubt, helped me rediscover my passion and gave me a clarity on my career goals.

I would like to express my immense gratitude to the Delft Global Initiative for awarding me with the Sub-Saharan Africa excellence scholarship and enabling me to study at such a top tier university as Delft University of Technology. This honor has helped me focus on my masters without any financial burden and has continuously been a source of motivation to work harder towards my goals.

I would also like to express my deep appreciation and gratitude to the chair of my masters thesis committee Max Hendriks for his invaluable insights and critical remarks. I would like to thank him for being accommodating and supportive throughout my thesis project. I would also like to thank my company supervisor Lex van der Meer who gave me regular supervision and guidance. It has been an enriching learning experience to work with both of them. In addition I would like to thank Eva Lantsoght and Pierre Hoogenboom for agreeing to join my committee and for their critical comments and insight through out my thesis project. Their inputs and guidance have been invaluable.

I would like to extend a special thanks and appreciation to Kris Riemens, from ABT, for always being available for consultation and providing constructive feedback every step of the way. His intellectual inputs and appreciative comments have inspired me to push my limits during the course of the research.

I would like to thank God for his continued blessings and being my constant source of strength. I would also like to thank my family for their unconditional love and support throughout this two years. I would like to thank my friends Shozab Mustafa, Shantanu Singh and Samyuktha Sivaram for their support throughout my thesis. Last, but not least, I would like to thank my friends, colleagues and all the connections I made during this period that have made this experience worth the while!

Selam Getahun Asefa
Delft, August 2020

Abstract

Piles and pile caps are commonly used in the Netherlands due to the soft shallow subsurface soil that is predominant in the country which does not have sufficient bearing capacity to support heavy structures. Pile caps are currently designed analytically using the strut and tie model (STM). This is believed to be conservative and results in an over-reinforced structure with higher cost and unsustainable design due to inefficient use of materials. The main objective of this thesis is to investigate the application of Non Linear Finite Element Analysis (NLFEA) to design pile caps.

Five experiments were selected from literature and modelled in DIANA. These pile caps had flexural, corner shear, flexure-induced punching and combined flexure and corner shear failure modes. Quarter of the pile caps were modelled using Finite Element Model (FEM) as it saves computational time and cost by making use of symmetry while still predicting the failure mechanism and failure load within 99% of the full model. The reinforcement was modelled using both embedded and Shima bond-slip.

The FEM results were subsequently compared with the experiment to gain insight into how accurately FEM can capture the structural response of pile caps. The comparison shows that failure mechanism and crack pattern can be accurately predicted for all pile caps. However, the accuracy of the failure load depends on the failure modes of the pile cap as ductile failures are captured more accurately than those with brittle failure. The difference between the peak load in the FEM and the experiment is observed to be 5 - 7% for ductile failures while it varies between 25 - 42% for brittle failures. These differences are liberal estimates.

Moreover, three pile caps that were designed using STM were modelled numerically to obtain the design resistance and compare the results. The comparison show that STM overestimates the stresses in the concrete by 40% – 70% as well as the crack width by 60 – 65%. This is because the effect flank reinforcement and post cracking contribution of concrete are not accounted in the STM. Numerical model results are also closer to the experimental results than analytical calculations by 50% on average.

The comparison between STM and numerical model revealed that optimization of pile caps is possible. Subsequently, four parameters: pile cap geometry, bottom rebar percentage, number of flank rebar and concrete quality were reduced to evaluate the effect on the structural response of pile cap. These parameters were selected based on the interview with experts and results of the comparison between the FEM and experimental results. The parametric study was performed on a pile cap with punching failure.

It was found that reducing the pile cap depth by 0.1m increases the rebar stress by 25 - 35% and reduces the failure load by 2 - 8%. Reduction of the bottom rebar percentage by 10% increases the crack width by 15 - 30% and lowers the failure load by 2 - 8%. A 50% decrease in the number of flanks is found to increase the stress in the bottom reinforcement by 20 - 25% but not affect the failure load significantly. Change in these three parameters does not change the failure mode and the failure load remained greater than the design load. However, decreasing

concrete quality accelerates the onset of crack which decreases failure load and changes the failure mechanism from punching to corner shear.

Cost analysis and environmental impact assessment also show that geometry optimization has more environmental and cost advantage than reducing the reinforcement. For every 0.1 meter reduction in depth, there is a 6% reduction in cost per pile cap and a 70 - 200 kg reduction in the CO₂ footprint.

Two sets of experiments were designed to validate the key findings of this thesis. The first set was designed to investigate if punching failure can be accurately predicted by FEM. This will be conducted on a scaled down pile cap with expected punching failure. A second set of experiment was designed to explore if the optimization observed in the numerical models can be achieved in reality. Two pile caps, with brittle and ductile failure were selected. Each will have a variable geometry, bottom rebar percentage, flank reinforcement and concrete quality.

The current STM approach does not capture all the failure modes of pile caps since the unity check does not distinguish between certain failures such as concrete crushing and punching. It also does not account for the contribution of flank reinforcement and concrete contribution to the tensile strength post-cracking. Therefore, future designs of pile caps should take these parameters into account to obtain a safe design without underestimating the capacity of the pile cap. This would result in a more efficient design with lesser material and lower cost.

Contents

1	Introduction	1
1.1	Background and Motivation	1
1.2	Scope and objective of research	2
1.3	Research questions	3
1.4	Research Methodology	3
1.5	Report outline	4
2	Literature Review	5
2.1	Strut-and-tie model	5
2.2	Current pile cap design approaches	7
2.3	Non-linear Finite Element Analysis	9
2.3.1	Material Models for Concrete	10
2.3.2	Effect of Confinement	13
2.3.3	Approach to Model Bond in Reinforced Concrete	17
2.3.4	Safety Formats	20
2.3.5	Previous Pile Cap Models	21
2.4	Practical insight from experts	23
2.4.1	Summary of interview responses	23
2.4.2	Past ABT projects	25
2.5	Experiments on pile cap	27
2.5.1	Experimental studies	27
2.5.2	Selected experiments for FEM design	32
2.5.3	Experimental program	34
2.5.4	Overview of Failure Modes	34
3	Comparison of FEM Models with Experimental Results	37
3.1	Description of Generic Finite Element Model	37
3.1.1	Material properties	37
3.1.2	Support and boundary condition	38
3.1.3	Loading	38
3.1.4	Meshing	39
3.1.5	Iterative procedures	39
3.2	Initial investigations	42
3.2.1	Size of the model	42
3.2.2	Material model	44
3.2.3	Confinement	47
3.2.4	Mesh Size	48
3.2.5	Load Step Size	49
3.2.6	Reinforcement type	49

3.3	FEM models of experimental pile caps	51
3.3.1	Suzuki et al.	51
3.3.2	Lucia et al.	54
3.3.3	Comparison with strut-and-tie calculations and experiments	62
4	Comparison of FEM Models with STM Results	65
4.1	Feringa Building	67
4.2	Kloosterboer Vastgoed	68
4.3	Comparison between Numerical Model and STM Calculation	69
4.3.1	Compressive Stress in Concrete	69
4.3.2	Internal Lever Arm	70
4.3.3	Stress in Reinforcement at ULS	71
4.3.4	Crack Width and Steel Stress at SLS	72
5	Parametric study	75
5.1	Pile cap geometry	75
5.2	Bottom reinforcement percentage	77
5.3	Number of flank reinforcement	79
5.4	Concrete quality	80
6	Proposal for experimental research	83
6.1	Purpose of experimental study	83
6.2	Experimental specimens	83
6.2.1	Experiment Set 1	83
6.2.2	Experiment Set 2	85
6.3	Preliminary study	89
6.3.1	Mix Design and Initial Tests	89
6.3.2	Experimental Set-up	89
6.3.3	Analysis of test results	94
7	Conclusion and Recommendation	95
7.1	Conclusion	95
7.2	Recommendation	97
Appendix A	Past ABT Projects Overview	102
Appendix B	Experimental Data	104
Appendix C	DIANA Script	108
Appendix D	Cost calculation	118

List of Figures

- 1.1 a) Pile cap design using beam theory b) 2D strut-and-tie model for pile cap c) forces idealized in truss system [1] 2
- 1.2 Research methodology 3
- 2.1 Disturbed and Bernoulli region in a simply supported beam [15] 5
- 2.2 a) Three-dimensional STM for four-pile pile caps [19] 6
- 2.3 Schematic representation of calculated reinforcement in four-pile pile cap [8] 8
- 2.4 Two types of crack modelling [29] 11
- 2.5 Concrete material properties [9] 11
- 2.6 Modified stress strain diagram for confined concrete [30] 14
- 2.7 Test model for confinement study 15
- 2.8 Compression stress-strain diagram 16
- 2.9 influence of pile cap depth on column load [40] 17
- 2.10 Shear traction-slip graphs 20
- 2.11 Internal Lever Arm in Manual Calculation [8] 22
- 2.12 Schematic representation of calculated reinforcement in four-pile pile cap [8] 22
- 2.13 Diameter of anchorage bend [8] 24
- 2.14 Longitudinal reinforcement layouts used by Blévoit and Frémy [48] 27
- 2.15 Crack pattern of pile caps tested by Suzuki et al. [50]) 28
- 2.16 Types of four-pile pile caps tested by Suzuki et. al. [53] 29
- 2.17 Strain distribution of reinforcing bars [54] 29
- 2.18 Reinforcement layout Gu, et al. in experiment [55] 30
- 2.19 Test arrangements of selected experiments 34
- 3.1 Top and side view of the reinforcement layout [53] 37
- 3.2 Tying on the top face of the column 38
- 3.3 CQ48I – 3D Plane quadrilateral interface elements (8+8 nodes) [9] 39
- 3.4 Geometry and mesh size of pile cap BDA-40-25-90-1 42
- 3.5 Load deformation graphs 42
- 3.6 Crack patterns at the bottom of the pile cap 43
- 3.7 Crack pattern of numerical model and experiment 44
- 3.8 Effect of compressive strength reduction due to lateral cracking 44
- 3.9 Total Strain Crack Model graphs for 45mm crack band-width 45
- 3.10 Load-deformation graph using different material model 45
- 3.11 Comparison of initial crack patterns between the two models 46
- 3.12 Kotosovos material model study 46
- 3.13 Compression stresses at displacement 3mm 47
- 3.14 Load-deformation graph for confinement vs unconfined 48
- 3.15 Stresses in the compression strut 48
- 3.16 Load-deformation graph of models with different mesh sizes 49
- 3.17 Load-deformation graph of models with different load step sizes 49

3.18	Load-deformation graph of models with different reinforcement types	50
3.19	Stresses and strains in embedded and bond-slip reinforcement types	50
3.20	Load-deformation graph for pile cap BDA-40-70-1	51
3.21	Crack pattern of experiment and numerical model for BDA-40-70-1	52
3.22	Load-deformation graph of pile cap BP-30-30-2	53
3.23	Principal tensile stresses in numerical models	53
3.24	Crack patterns on BP-30-30 in the experiment and numerical models	54
3.25	Geometry and reinforcement layout of Lucia et al. [58]	55
3.26	Reinforcement detail of the selected pile caps [58]	55
3.27	Load-deformation graph of pile cap 4P-N-A3	56
3.28	Crack patterns and failure surface on 4P-N-A3 in the experiment [58]	57
3.29	Crack patterns on 4P-N-A3 in the bond-slip model	58
3.30	Strain in 4P-N-A3 in the numerical model and experiment	58
3.31	Load-deformation graph of pile cap 4P-N-B2	59
3.32	Strain in 4P-N-B2 in the numerical model and experiment	59
3.33	Crack patterns on 4P-N-B2 in the experiment [58]	60
3.34	Crack patterns on 4P-N-B2 in the numerical models	60
3.35	Failure modes in pile caps [58]	61
3.36	Load-deformation graph of variation models of pile cap 4P-N-B2	61
4.1	Geometry of pile cap NFB-1 [64]	67
4.2	Reinforcement layout in pile cap NFB-1 [64])	68
4.3	Geometry of pile cap NFB-2 [64]	68
4.4	Reinforcement layout in pile cap NK-1 [65]	69
4.5	CCC-node in STM and numerical model	70
4.6	Lever arm calculation in numerical model	71
4.7	Example of stress in main reinforcement	72
4.8	Failure mode of pile cap NFB-1 (scaled view)	73
5.1	Crack pattern at ULS for pile caps with different depth	76
5.2	Crack pattern at failure for pile caps with different rebar percentage	78
5.3	Stress in main rebar at ULS for pile caps with different rebar percentage	78
5.4	Stress in flank rebar at ULS for pile caps with different number of flanks	79
5.5	Load-deformation graph of pile caps with various concrete quality	80
5.6	Crack pattern at ULS for pile caps with different concrete quality	81
6.1	Geometry of scaled NFB-1	84
6.2	Expected failure mode and load capacity of scaled NFB-1	84
6.3	Expected experimental load deflection diagram of 4P-N-C3	85
6.4	Placement of LDVTs and Strain Gauges	90
6.5	Schematic representation of crack pattern to be drawn	92

List of Tables

- 2.1 Overview of comparison of current design guidelines and approaches 9
- 2.2 Material property of confinement test model 15
- 2.3 Parameters defining the mean bond stress–slip relationship of ribbed bars [18] 19
- 2.4 Detailed data of selected past project 26
- 2.5 Global overview of available experimental data 31
- 2.6 Property of selected experimental pile caps (1/2) 33
- 2.7 Property of selected experimental pile caps (2/2) 33

- 3.1 Material properties of column and pile cap 38
- 3.2 Convergence criteria 40
- 3.3 Summary of finite element modeling choices 41
- 3.4 Concrete and reinforcement material properties 52
- 3.5 Concrete material properties 56
- 3.6 Comparison of yielding and ultimate load of 4P-N-A3 57
- 3.7 Comparison of failure load between numerical, STM and experimental results 62
- 3.8 Ratio of experimental failure load and numerical and STM results 62
- 3.9 Comparison of yielding load between numerical, STM and experimental results 63

- 4.1 Concrete inputs for safety formats 65
- 4.2 Summary of FEM choices for STM designed pile caps 66
- 4.3 Comparison between numerical and STM results for stress in concrete 70
- 4.4 Comparison between numerical and STM results of internal lever arm 71
- 4.5 Comparison between numerical and STM results of stress in rebars at ULS 72
- 4.6 Comparison between numerical and STM results at SLS 74
- 4.7 Unity check comparing numerical and STM 74

- 5.1 Comparison between results for pile cap of various depth 75
- 5.2 Comparison between results for pile cap of various reinforcement percentage 77
- 5.3 Comparison between results for pile cap of various number of flank re-bars 79
- 5.4 Comparison between results for pile cap of various concrete quality 80

- 6.1 Unity check of scaled NFB-1 at calculated failure load using STM 85
- 6.2 Variable parameters in Experiment Set 2 86
- 6.3 Experiment set 1 and 2 overview (1/2) 87
- 6.4 Experiment set 1 and 2 overview (2/2) 88
- 6.5 Measurements to be taken per pile cap 93

- A.1 Pile caps from past ABT projects 103
- B.1 Pile cap data from experiments 105

Notations

Roman upper case letters

$A_{c,eff}$	Effective concrete area
A_{sB}	Cross sectional area of main bottom reinforcement
A_{sH}	Cross sectional area of secondary bottom reinforcement
A_{sV}	Cross sectional area of shear reinforcement
E_c	Young's modulus of concrete
E_s	Young's modulus of reinforcement
E_0	Initial young's modulus
F_d	Design value of actions
G_0	Initial shear modulus
K_0	Initial bulk modulus
G_S	Secant shear modulus
G_c	Compressive fracture energy
G_f	Tensile fracture energy
I_1	First invariant of stress tensor
K_S	Secant bulk modulus
P	Applied load
P_{cr}	Cracking load
P_y	Yield load
P_{ult}, V_u	Failure load
R_d	Design resistance
R_u	Maximum reaction of the pile that fails first
$S_{r,max}$	Maximum crack spacing
$V_{y,B}$	Yield load of the main longitudinal reinforcement
$V_{y,V}$	Yield load of the stirrup

Roman lower case letters

c	Concrete cover
d	Effective depth
e	Pile center distance from the edge of the pile cap
f_c	Specified concrete compressive strength
f'_c	Specified concrete compressive strength
f_{cd}	Design value of concrete compressive strength
f_{ck}	Characteristic value of concrete compressive strength
f_{cm}	Mean value of concrete compressive strength
f_{ct}	Specified value of concrete tensile strength
f_{ctd}	Design value of concrete tensile strength

f_{ctk}	Characteristic value of concrete tensile strength
f_{ctm}	Mean value of concrete tensile strength
f_{c3}	Compressive principal stress in concrete
f_p	Peak stress in confined concrete
f_y	Specified yield strength of steel
f_{yd}	Design yield strength of steel
f_{yk}	Characteristic yield strength of steel
f_{ym}	Mean yield strength of steel
f_u	Ultimate strength of steel
k_c, k_n	Reduction factors in strut-and-tie model calculation according to FIB model code
l_{bpt}	Transfer length of reinforcement
h_c	Crack band width
t_t	Shear traction
w_k	Crack width
z	Lever arm

Greek letters

α_e	Ratio of the steel and concrete young's modulus
β	Shear retention factor
ϵ_p	Peak strain in confined concrete
ϵ_{cm}	Mean strain in concrete
ϵ_{sm}	Mean strain in reinforcement
σ_c	Compressive stress in the concrete
$\sigma_{c1}, \sigma_{c2}, \sigma_{c3}$	Principal stresses in the concrete
σ_{id}	Equivalent internal hydrostatic stress for change in volume due to deviatoric loading
σ_{oct}	Hydrostatic stress
$\sigma_{Rd,max}$	Design strength for concrete struts or node
σ_s	Stress in the reinforcement
σ_{SLS}	Stress in serviceability limit state
σ_{ULS}	Stress in ultimate limit state
$\rho_{p,eff}$	Rebar ratio
δ_{ij}	Kronecker delta
Δu_t	Relative displacement (slip) between concrete and reinforcement
τ	Shear stress
τ_b	Bond stress for a given slip
τ_{bf}	Minimum friction traction stress
$\tau_{b,max}$	Maximum bond-stress
$\tau_{oct,u}$	Critical octahedral shear stress
\varnothing	Diameter of reinforcing bar

1. Introduction

1.1 Background and Motivation

Pile caps are thick concrete structures used to transfer axial loads and bending moments from piers and columns to pile foundations. Their geometry and dimension depends on the number of piles in the pile group and the spacing between them. The depth is determined by geotechnical factors such as swelling of the soil and the groundwater table as well as structural factors such as punching shear and anchorage. Pile caps must have sufficient capacity to withstand bending moment and shear force as well as sufficient depth to provide adequate bond length for the pile reinforcement and pier or column starter bars [1]. Since the soft shallow sub surface soil that is predominant in the Netherlands does not have sufficient bearing capacity to support heavy structures, piles and pile caps are commonly used in construction. Thus, accurate design of concrete pile caps is significant for an efficient design of building and bridge foundations.

The two common methods of pile cap design are the beam theory and the truss analogy i.e. the strut-and-tie model. The former is also known as sectional approach as the area of the pile cap is divided into rectangular beams. It assumes pile caps as large beams spanning between piles and designed similar to two way slabs or shallow footing. Beam flexure theory is applied to compute the longitudinal reinforcement at the critical section and concrete contribution alone is considered for shear resistance. The critical section for shear is assumed to be located at 20% of the pile diameter while the critical moment is the product of the pile reaction and the distance from pile center to the face of the column as shown in [Figure 1.1](#) [2].

For structures with span-to-depth ratio less than 2, the truss analogy is adopted as the beam theory is no longer appropriate. This is because the sectional approach fails to capture the complex strain variation forming a compressive strut in pile caps which leads to overly conservative design. The strut-and-tie model is a lower-bound plasticity-based design method that uses the truss analogy to visualize the flow of forces within a structure. The model states that compressive struts are carried by concrete compressive struts while tensile forces are resisted by steel reinforcement ties. Several researches such as Clarke et al. [3] and Ahmad et al. [4] have shown that the strut-and-tie model is a better approach to analyse pile caps and calculate the required reinforcement.

In the Netherlands, pile caps are currently designed following Eurocode (NEN-EN 1992-1-1:2005) [5] guidelines using the strut-and-tie model (STM). The code outlines reinforcement design in the tensile ties for partial and full discontinuity regions, design strength for a concrete strut and rules for designing the nodes. The EC 2 in de Praktijk is a document that interprets the NEN-EN 1992-1-1:2005 regulations using practical examples. It provides detailed examples of two-pile and four-pile pile cap design following the same principle. Recently, however, there have been several discussions among engineers about the accuracy of the strut-and-tie model as it is expected to be conservative. The approach is expected to result in an over-reinforced structure which translates as higher cost for the client and unsustainable design due to inef-

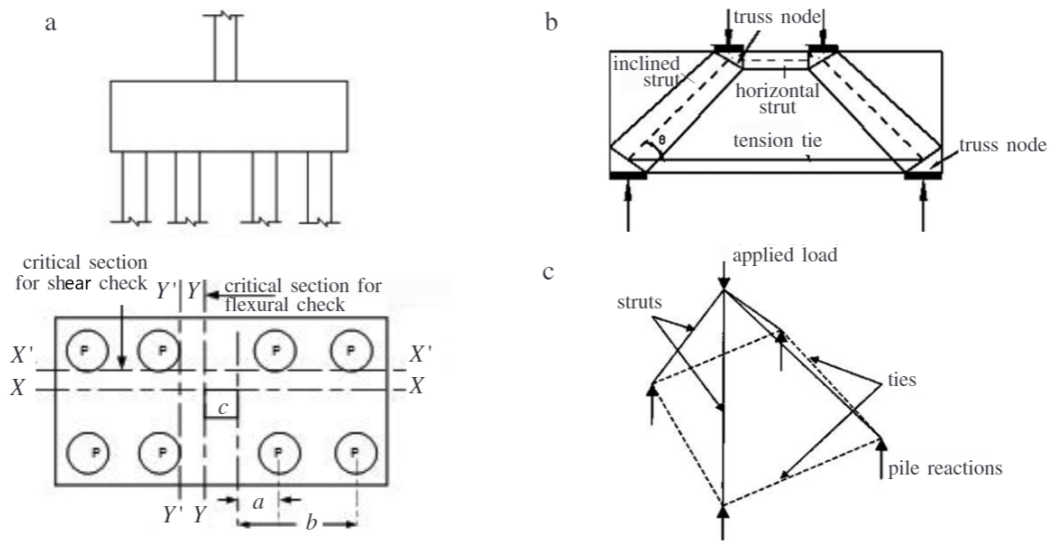


Figure 1.1: a) Pile cap design using beam theory b) 2D strut-and-tie model for pile cap c) forces idealized in truss system [1]

efficient use of materials.

Non-linear finite element analysis (NLFEA) is the simulation of physical structures by converting them to mechanical and finite element model based on discretization of elements. It is an important computational tool for predicting the capacity and structural response of reinforced concrete. It includes idealization, discretization, defining the constitutive model and solution procedure. NLFEA will be used to assess the hypothesis

Shozab Mustafa [6] and Jayant Srivastava [7] investigated this hypothesis in their internship. They explored the optimization of reinforcement in two and four-pile pile caps respectively by analyzing the examples from EC 2 in de Praktijk [8] in DIANA and comparing the results between the manual results and numerical analysis. The results from both researches corroborated the hypothesis by showing that the manual calculations underestimate the pile cap lever arm which results in higher forces in the tensile tie and subsequently higher reinforcement. The results also showed that crack width and stresses in reinforcements are over estimated in the manual calculation as compared to numerical analysis. It must be noted however that these findings are specific to the examples from EC 2 in de Praktijk.

The motivation for this thesis is therefore to generalize these findings by performing NLFEA on experiments from literature and investigating the difference between experimental, numerical and manual calculations. A range of experiments and practical examples shall be analyzed to estimate how realistic the current pile cap design is and to understand the key parameters that affect the structural response. Despite significantly advancing in recent years, application of FEA still faces some challenges as the results are affected by numerous aspects of the analysis such as the selected constitutive model, mesh size and load step. Thus the research in this thesis will also help understand how realistic the numerical analysis is to determine the ultimate capacity and failure mode of concrete pile caps.

1.2 Scope and objective of research

The scope of this research is limited to the non-linear finite element analysis and parametric study of rectangular or square four-pile pile caps. Pile caps with taper or geometrical irregularities will not be considered. The selected pile caps are designed using the strut-and-tie model

using any design code. Pile caps designed using sectional approach will not be considered.

Moreover, the finite element model are developed in 3D environment using DIANA FEA 10.3 [9]. Experiments will not be conducted during the course of this research but test results from experiments from various literature and examples from past projects in ABT will be studied and modelled.

1.3 Research questions

The main objective of this thesis is to investigate the application of NLFEA to the design of pile caps. To fulfil this objective, the following research questions shall be answered.

- How can non-linear finite element analysis be used to improve the current design of pile caps?
 1. How realistic is nonlinear finite element analysis compared to experiments?
 2. How do numerical models compare to analytical calculations?
 3. What are the main parameters that affect the structural response of the pile cap? How do these parameters affect the response?
 4. What kind of experiments can be designed to get deeper insight into the structural response of pile caps as well as validate the key findings of this research?

1.4 Research Methodology

The research methodology is divided into five phases in order to achieve the above mentioned research goals and to answer the research questions.

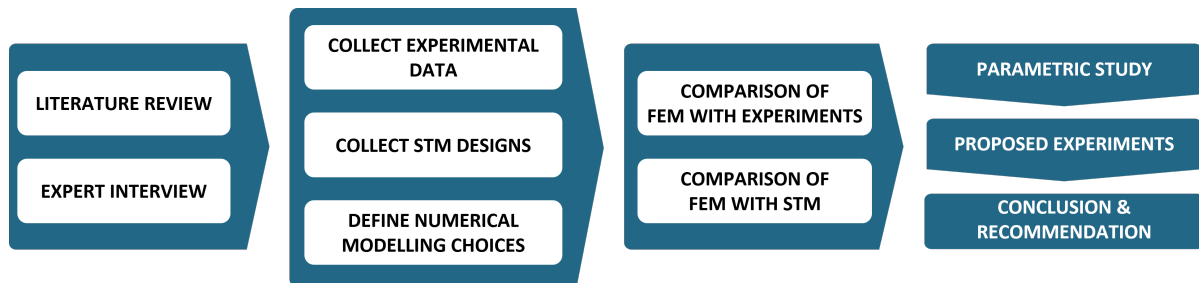


Figure 1.2: Research methodology

Literature study

- The current design practices of pile cap design using strut-and-tie model shall be studied to understand the underlying theory and its application. Various literature on STM including current code provisions such as Eurocode and FIB Model Code shall be reviewed.
- Total Strain Crack Model and Kotsovos Concrete Model will also be explored. Apart from reading literature and DIANA manual, a pile cap shall also be modelled to view the effect of each material model on the results. This is to understand the applied theories in the software and select the most appropriate one to obtain the most realistic result.
- Furthermore, experiments with reliable data will also be researched and selected. Primary selection criteria will be based on similarity of the experiment setup to the MSc project scope and how complete the relevant data is logged and presented.

Practical insight from experts

- Experts from ABT who are or have been involved in the structural analysis of pile caps in practical projects will be interviewed. This will help understand the practical aspect of pile cap design and construction and the differences between the theory and practice.
- Moreover, practical examples of pile caps that have been in ABT projects in the last 5-10 years will be collected which will be modelled using DIANA and 3-5 examples will be selected for NLFEA.

Analysis of pile caps

- The draft model code 2020 specifies the first step of NLFEA analysis as making an outline plan of the solution technique, material model and constitutive relation. Thus, appropriate solution and relevant models shall be defined initially.
- Subsequently, the collected practical examples and experiments will be modelled in DIANA and compared with manual calculations or experimental results. This will provide insight into the accuracy of the manual calculations and NLFEA.
- Analysis outputs will then be post processed and conclusions will be drawn based on these models regarding best practice for pile cap design. Moreover, one pile cap design will be selected for the parametric study.

Parametric study

- A parametric model will be developed for the pile cap selected to perform a parameter study and gain insight in the influence of various parameters on the structural behavior such as the ultimate load capacity and stress in bottom reinforcement. This is to understand how much these parameters affect the structure.

Proposal for experimental research

- Based on the previous studies, experiments will be designed to validate the results of the drawn conclusions in this thesis.

1.5 Report outline

Chapter 1 is the introduction of the document with the background and motivation of the research. It will also define the research questions and the scope.

Chapter 2 discusses the literature review exploring various studies and experiments conducted on four-pile pile caps as well as experts interviews on the current design approach.

Chapter 3 mainly discusses the numerical techniques used to model the pile caps and the results of the FEM design followed by their comparison to the experimental data.

Chapter 4 discusses results from the FEM model of pile caps designed using STM calculations and the subsequent comparison of the results.

Chapter 5 discusses the effect of changing pile cap parameters such as the geometry and concrete quality on the overall structural response.

Chapter 6 focuses on designing experiments that can be conducted to verify the results of this research.

Chapter 7 outlines the key conclusions of this research and proposes recommendations for future studies.

2. Literature Review

2.1 Strut-and-tie model

The strut-and-tie model (STM) is a lower-bound plasticity-based design method and currently the main procedure used for pile cap design as recommended by NEN-EN 1992-1-1:2005 [5]. Ritter and Morsch [10] proposed the classical truss analogy at the turn of the last century for the design of reinforced concrete members. The method was refined and expanded Leonhardt [11] and other researchers until Thurlimann along with Marti and Mueller [12], created the scientific basis for application relating it to the theory of plasticity. This broadened application of STM to almost all concrete structures and not just beams as used previously. Leonhardt [11], Kupfer [13] and Thurlimann [12] then showed that the model could be applied to deep beams and corbels in various applications [14].

Load and geometric discontinuities cause a nonlinear distribution of strains to develop within the surrounding region. The strut-and-tie model enables the sectional design of these disturbed regions (D-regions) as the assumptions of the traditional beam theory “plane sections remain plane” no longer remain true. St. Venant’s principle stipulates that linear stress distribution can be assumed at about one member depth from a load or geometric discontinuity. Thus, D-regions are assumed to extend distance d from the applied load or support reaction where d is the distance between the extreme compression fiber and primary longitudinal reinforcement as shown in 2.1 [15].

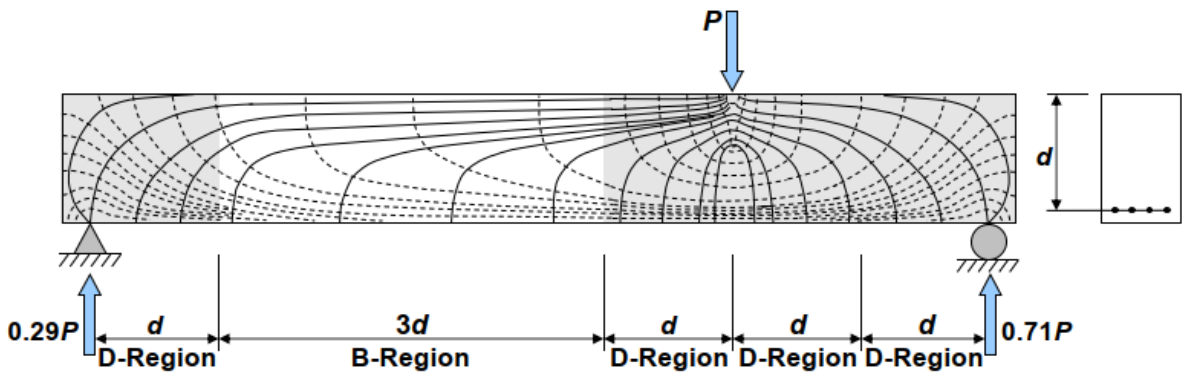


Figure 2.1: Disturbed and Bernoulli region in a simply supported beam [15]

Furthermore, a region of structural member is assumed to have predominantly non-linear stress distribution if the shear span (a), which is the distance between the point of load application and the nearest support, is less than 2–2.5 times the member depth d . In cases like this, the span will be entirely disturbed which is referred to as deep beam behavior exhibited in the right side of the beam in Figure 2.1. STM helps idealize the deep beam action in pile caps based

on the principle that “the loads applied on the structure is transferred to the supports using the shortest paths” [16]. The internal load path in reinforced concrete is therefore approximated by an idealized truss where concrete zones with primarily unidirectional compressive stresses are modelled by compression struts, main reinforcements are modelled using tension ties and nodal zones (areas where strut-and-tie meet) are analogous to joints of a truss [17]. The FIB Model Code [18] describes nodes as highly bi- or triaxially stressed zones within a stress field. STM generally obeys two principles: the truss model is in equilibrium with external forces and concrete member has sufficient deformation capacity to accommodate the assumed force distribution [14].

The strength of concrete in the compression strut or nodes depends on the multi-axial state of stress (transverse compression and tension) and disturbances from cracks particularly those not parallel to the compressive stress. Schlaich et al. [14] provides two criteria for optimizing STM model: minimizing the length of the reinforcement and the strain in the tensile ties. Two-dimensional truss analogy considers the resultant of the strut-and-tie forces in the same plane. However, this method has limitations when several struts are joined in the same node or nodal zones subjected to complex three dimensional states of stress. Schlaich et al. [14] stated that “If the state of stress is not predominantly plane, as for example in the case with punching or concentrated loads, three-dimensional strut-and-tie models should be used”. Hence, many researchers have explored various types of three-dimensional STM models for pile cap design.

Yun et al. [19] proposed employing a statically indeterminate three-dimensional STM with diagonal ties to accommodate the load-carrying capacity of some regions in tension. The degree of confinement from the reinforcement and three-dimensional stress states are also accounted for when determining the strength of three-dimensional struts and nodal zones. An iterative technique is used to determine load carrying capacity of strut-and-ties. The methodology was applied on 115 reinforced concrete pile caps and the results were compared with ACI 318-19 code provisions. The results from the proposed method were much more closer to experimental results than ACI 318-19 as the latter resulted in over conservative design.

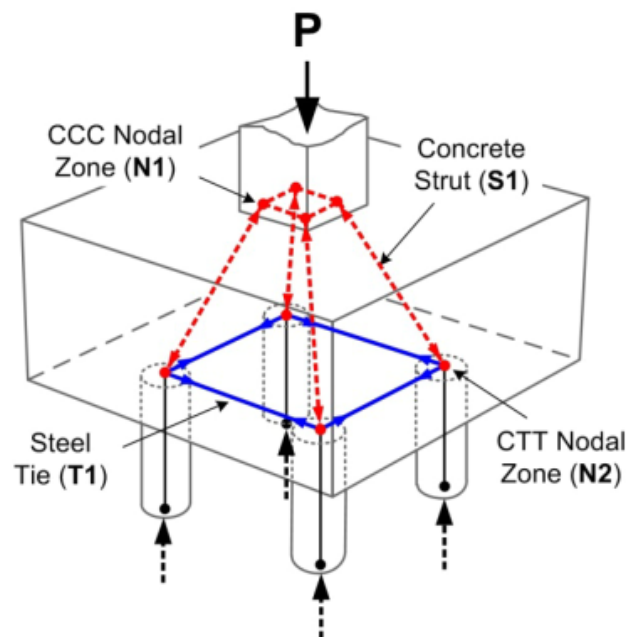


Figure 2.2: a) Three-dimensional STM for four-pile pile caps [19]

Mathern and Chantelot [20] proposed a model with an iterative procedure to find the optimal position of the members by refining nodal zone dimensions with respect to concrete strength under triaxial stress. The method assumes the loading area (columns), bearing areas (piles) and the height of the node to be known. The height of the node is defined as two times the distance from the edge to the axis of the strut. The shape of the struts is determined using the known or assumed corners of the nodal zone and the strut axis. Strength criterion is also formulated for combined strut splitting and crushing confined by plain concrete for regions away from the nodal zone. The comparison of this methodology with experimental results and design codes such as Eurocode (NEN-EN 1992-1-1:2005) revealed that the results are accurate in predicting failure loads and failure modes. The angle limitation between inclined struts and tie was set as $45^\circ - 60^\circ$. This is following Schlaich and Schafer's [21] recommendation to avoid the need for high plastic redistribution and strain incompatibility problems. When the concentrated force is transferred in the model by multiple inclined struts, the limitation is recommended to be applied to the angle of the resultant of the forces in the struts.

Other researchers like Dey and Karthick [22] proposed a displacement based compatibility STM that incorporates geometry and material constitutive relationships and accounted for reduction of concrete strength due to transverse tension in the truss. The model was proven to predict load-deformation and internal strain behavior as well as the failure mode of four-pile pile caps.

2.2 Current pile cap design approaches

Eurocode 2 (NEN-EN 1992-1-1:2005) stipulates that STM can be used for design in ultimate limit state (ULS) as well as verification in serviceability limit state (SLS). STM models can be developed by taking the stress trajectories and distributions into account from either linear-elastic theory or the load path method. The maximum stress that can be applied in a strut with or without transverse compressive stress can be assumed to be equal to the design compressive strength, f_{cd} of concrete. On the other hand, higher design strength can be assumed for regions with multi-axial compression while appropriate reduction factors must be applied for cracked zones or regions with transverse tensile stress. The transverse tensile force, T , depends on whether the region is partially or fully discontinuous. The design values of the compressive stresses in the nodes depends on the type of node, the value of concentrated forces and the respective area they are acting on. Three type of nodes are described in EN 1992-1-1:2004 based on the number of ties anchored at the node: CCC (no ties), CCT (one tie) and CTT (two ties) [5]. The inclination angle of struts is of interest since using an inappropriate value could have negative repercussions such as the need for large plastic redistribution and strain compatibility problems. Eurocode specifies that the compressive stress can be increased by 10% if all the angles between the strut-and-ties are $\geq 55^\circ$ [5].

The FIB Model Code [18] specifies compatibility of deformations should roughly be taken into account when developing STM by orienting the direction and position of the forces to the corresponding compression trajectories in the linear elastic stage (uncracked state). This is to minimize force redistribution post cracking and enable the use of the same STM model for both design in ULS and verification in SLS. It also outlines steps to take when developing the model including width of the D-region, values of the internal forces and geometry of the nodes. Moreover, the code provides reduction factors for regions with transverse compression.

$$k_c = 1.0\eta_{f_c} \quad (2.1)$$

$$\text{where } \eta_{f_c} = \left(\frac{30}{f_{ck}}\right)^{\frac{1}{3}} \leq 1.0$$

Where, k_c is the reduction factor,
 f_{ck} is the characteristic value of concrete compressive strength

The code defines design strength of tensile fields as the design yield strength of the reinforcement (traditional or prestressing steel). Similar to Eurocode, the maximum stress that can be applied at a node is dependent the type of node which determines the reduction factor. In addition, it also depends on the characteristic compressive strength of concrete, f_{ck} , and safety factor, γ_c [18].

On the other hand, the EC 2 in de Praktijk [8] provides detailed examples for the design of 2-pile and 4-pile pile caps following NEN-EN 1992-1-1:2005 guidelines. The lever height is calculated using formulas from the old Dutch code (NEN 6720:1995) while the CCC and CTT nodes are analyzed according to Eurocode. It is assumed that the compressive struts are fully surrounded by the concrete in the pile cap. Thus, the concrete confinement is sufficient to withstand the transverse tension perpendicular to these struts. This assumption prevents the need for shear reinforcement in the interior of the pile. Flexural reinforcement are also concentrated above the piles across the tension zone as shown in Figure 2.3. The width of the tension zone is calculated as $2 * e$, where e is the distance between the center of the pile to the edge of the pile cap. Crack width and anchorage are also computed according to NEN-EN 1992-1-1:2005.

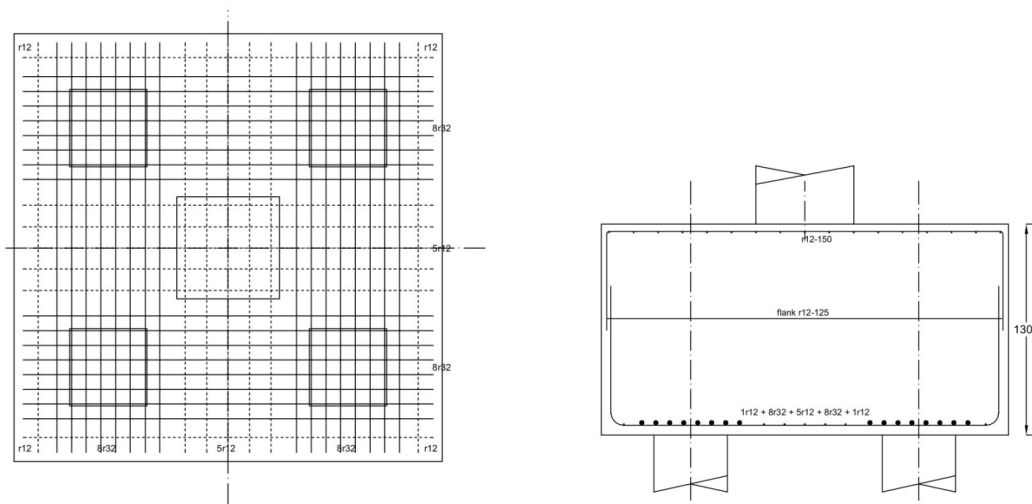


Figure 2.3: Schematic representation of calculated reinforcement in four-pile pile cap [8]

Although STM is the current choice of design method in Eurocode (NEN-EN 1992-1-1:2005) and other international codes, it has a few drawbacks. The first challenge is creating an appropriate strut-and-tie model particularly in three-dimensional structures. As mentioned previously, STM models are developed by considering the stress patterns in plane or rectangular elements. Direction of strut-and-tie are then determined by the direction of principal compressive and tensile stresses respectively. Moreover, their dimensions are assigned by considering the crack width limitations [21]. Two drawbacks of this approach are difficulty to generate a model for a complex stress distribution and visualizing the interior stress trajectories in three-dimensional members. Another challenge is the lack of proven guidelines for three-dimensional STM as most codes and guidelines focus on two-dimensional structures. Moreover, experts in ABT mention that there have been discussions among engineers recently about the accuracy of the STM design approach as it is based on the lower-bound theorem of plasticity and believed to be conservative. The STM calculations are expected to result in an over-reinforced structure which translates as more cost for the client and unsustainable design due to inefficient use of materials.

Table 2.1 summarizes the comparison between current design guidelines and approaches discussed in this section.

Table 2.1: Overview of comparison of current design guidelines and approaches

	Start of anchorage	Max stress in Strut ($\sigma_{RD,max}$)		Tensile Ties		Compressive stress in the node ($\sigma_{RD,max}$)
		Transverse compression	Transverse tension	Design strength	Width	
Eurocode (NEN-EN 1992-1-1:2005)	Beginning of node (inner face)	f_{cd}	$0.6v'f_{cd}$	f_{cd}	-**	$k_n v' f_{cd}$, where $k_1 = 1.0$ or 3.0 (CCC) $k_2 = 0.85$ (CCT)
EC 2 in de Praktijk		-	-		2e	$k_3 = 0.75$ (CTT)
Fib Model Code		$\eta_{fc} f_{cd}$	$0.75\eta_{fc} f_{cd}$		-	$k_c f_{cd}$, where $k_c = 1.0\eta_{fc}$ (CCC) $k_c = 0.75\eta_{fc}$ (CCC & CTT)

* Intersection between the tension force and diagonal extension of the node

** Though the value of tensile tie width is not specified, Eurocode mentions that the reinforcement must be distributed over the width of the transverse tension

Where, $v' = 1 - f_{ck}/250$
 $\eta_{fc} = (\frac{30}{f_{ck}})^{\frac{1}{3}} \leq 1.0$
 k_n & k_c are reduction factors,
 e is the distance between pile center to edge of the pile cap
 f_{ck} & f_{cd} are the characteristic and design concrete compressive strength respectively

2.3 Non-linear Finite Element Analysis

Non-linear finite element analysis is an important computational tool for modelling the non-linear behavior of reinforced concrete structures and determining their structural capacity, crack development and failure mode. It is the simulation of physical structures by converting them to mechanical and finite element model. The earliest publication of the application of FEM on concrete structures was in the second half of the 20th century by Ngo and Scordelis [23] who analyzed simple beams with predefined crack patterns and constant strain triangular elements. A linear elastic analysis was used to determine the stresses in the reinforcement and concrete. Nonlinear material properties for concrete and steel were introduced by Nilson who implemented nonlinear bond-slip relationship in the analysis and used an incremental load method on eccentric reinforced concrete tensile members. Quadrilateral elements were used in the analysis and the solution was stopped when an element reached the tensile strength to redefine a new cracked structure and reloaded incrementally to account for cracking [24]. However, continuous analysis without interrupting the solution was possible when Franklin developed nonlinear analysis that automatically accounted for cracking in finite elements and redistribution of stresses within the structure [25].

Application of NLFEA involves four key aspects:

Idealization of the physical problem

This includes schematization of the structure's geometry, boundary conditions, applied loads and their integration with surrounding structures.

Discretization of the idealized problem

This includes defining the type and size of finite elements to discretize the geometry of the structure which determine the displacement field. It also includes defining how the strains are calculated within the elements.

Constitutive model

Defining the stress-strain relationship, also known as the constitutive model, is a crucial aspect of finite element modeling. The constitutive model depends on the type of material. Most FEM software provide material models for linear and non-linear behaviour based on the user defined inputs.

Solution procedure

In NLFEA, the relation between the force and displacement vector is no longer linear and the varying stiffness of the structure at different loads is taken into account. An incremental-iterative solution procedure is necessary to solve the system of equations to obtain the equilibrium between external and internal forces. Therefore, loading the structure appropriately and choosing the most suitable iterative solution procedure, load step size and convergence criteria is imperative to obtain accurate results.

These four aspects of NLFEA are specific to each problem. Thus, each must be carefully selected to prevent inaccurate idealization, misleading results or high errors in the numerical results.

2.3.1 Material Models for Concrete

NLFEA models are based on discretization of elements with intrinsic model and factors which affect the analysis results. Thus, understanding the theories and assumptions behind these models is imperative to use the most appropriate design inputs, understand the implications of using each model, accurately interpret the results and identify errors in the model (if any).

The first finite element model of reinforced concrete which accounted for the effect of cracking was developed by Ngo and Scordelis who carried out a linear elastic analysis on beams using a discrete crack model [23]. Cracks were modeled by separating the nodal points of the finite element mesh creating a discontinuity in the mesh. J. G. Rots emphasizes that this reflects the cracks in concrete more realistically as it is geometrical discontinuity that separates the material. Interface elements are used at the predefined crack location. The model can be used on concrete structures with dominant cracks with known locations. A key drawback of this approach is that the gap of an element edge means discontinuity in nodal connectivity which does not fit the nature of finite elements [26]. Computational efforts are also significantly increased with the change of topology and redefinition of nodal points.

The need for a crack model that offers a general crack orientation and automatic generation of cracks without redefining the finite element topology has led to the development of smeared crack model. Rashid [27] introduced the concept of smeared cracking in his research of axisymmetric response of prestressed concrete reactor structures by taking cracking, temperature, creep and load history into account. Unlike the discrete cracks model which represent a single crack, the smeared crack model represents a cracked area with finely spaced cracks perpendicular to the principal stress direction. Though microcracking of concrete precedes fracture, this underlying assumption of smeared model conflicts with the reality of discontinuity in the member.

Moreover, the dependency on the finite element mesh size and tendency of inelastic strains to localize along one row of finite elements remain major drawbacks in this model. This can be avoided by introducing localization limiter such as the crack band model which associates the strain-softening law with a certain characteristic width, h_c , of the crack band and eliminates the dependency of concrete fracture energy on the element size [28]. Another drawback of the smeared approach is the risk of stress-locking when a smeared softening approach is used to simulate localization. Figure 2.4 shows the graphical representation of the two crack models. Two smeared crack models, the Total Strain Crack Model and the Kotsovos Model, are studied

and briefly discussed in this section.

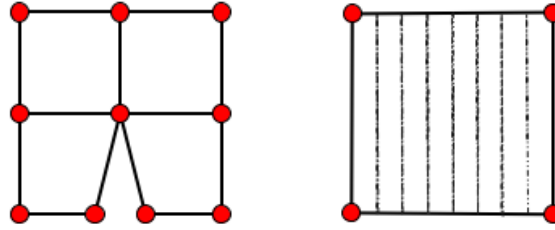


Figure 2.4: Two types of crack modelling [29]

a. Total Strain Crack Model

The Total Strain Crack Model is based on the smeared crack approach which considers cracking as a distributed effect and simulates cracked materials as a continuous medium. It's based on the Modified Compression Field Theory by Vecchio and Collins which considers stress equilibrium and strain compatibility at the crack interface. Crack is initiated when the principal stress exceeds the tensile strength [30].

Compressive behavior is assumed to be influenced by lateral cracking and confinement. Thus, the effect of increased stress due to lateral confinement can be accounted for in the compressive stress-strain relation. There are multiple predefined compression hardening or softening curves and the appropriate function for nonlinear FEM shall depend on the compressive fracture energy and post peak behavior of concrete. The parabolic softening curve shown in Figure 2.5a is a function of the compressive fracture energy. The Total Strain Crack model also provides several functions for the tensile behavior of concrete with or without taking into account the tensile fracture energy. Exponential softening functions such as Hordijk shown in Figure 2.5b are recommended as per Guidelines for Nonlinear Finite Element Analysis of Concrete Structures as it results in more localized cracks [31].

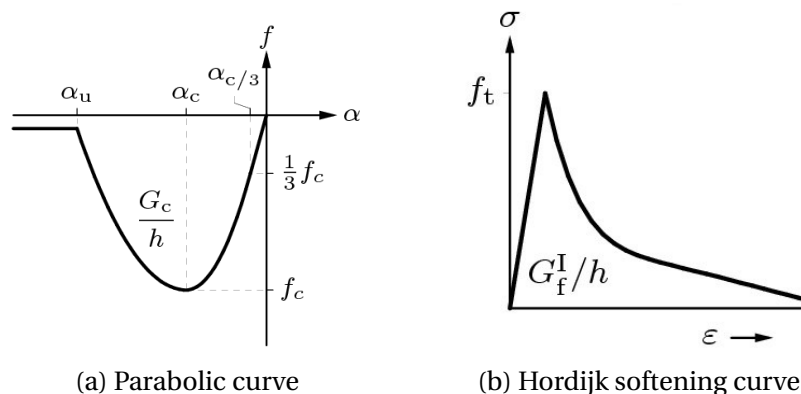


Figure 2.5: Concrete material properties [9]

Fixed total strain model

In this model, the crack is fixed upon initiation. Thus, the stress-strain relations are evaluated in a fixed coordinate system and crack orientation does not change during subsequent loading [9]. Consequently, shear is generated across the crack and the initial shear stiffness of concrete is reduced. Shear retention factor, β , is therefore applied to account for this reduction. Though the ease of formulating and implementing this model led to its popularity in the early seventies, studies have shown that the model has numerical problems due to the

singularity of the material stiffness matrix. Furthermore, the crack patterns predicted using this models has significant discrepancy with the ones observed in experiments [32]. This issue can be circumvented by introducing crack shear modulus which improves the accuracy of the model by eliminating the singularity of the stiffness matrix and the associated numerical instability. Recent models use a variable crack shear modulus to fully represent the change in shear stiffness as the principal stress vary from tension to compression [33].

Rotating total strain model

Contrary to the prior model, the crack in this model rotates continuously with the principal direction of the strain vector. The crack direction is kept perpendicular to the principal tensile strain direction which prevents shear strain from occurring in the crack plane and the need for crack shear modulus [9]. Vecchio and Collins [30] have shown in their research that crack orientation changes with loading history and the response of concrete elements depends on the current not on the original crack direction. A drawback in this approach is difficulty in correlating analytical results with experimental fracture mechanics results. Nevertheless, the model is currently being successfully used to study the global structural behavior of RC structures. Excessive stress rotation after cracking when relatively high shear retention factors are employed has been shown to lead to solutions that are too stiff [26].

Subsequent modelling in this thesis will be done using the rotating smeared crack concept as the implicit shear retention function results in a more flexible structural response. Moreover, as the location of cracks is not predefined, the pile caps cannot be modelled using discrete models.

b. Kotsovos Concrete Model

Kotsovos Concrete Model is a fully triaxial material model for concrete nonlinear behavior. The material model follows a smeared, non-orthogonal, fixed cracking approach with a maximum number of three cracks per integration point [34]. The model uses user-defined cylinder compressive strength, f_c , to derive other parameters such as the initial Shear (G_0), Bulk (K_0) and Young's modulus (E_0), as well as the tensile strength f_t . The constitutive relation is based on the assumption that the non-linear deformation response of concrete subjected to an increased state of stress below the ultimate stress level can be described in terms of the internal fracture process which reduces tensile stress concentrations near the tips of internal microcracks [35].

The total strain in an integration point which corresponds to a given stress below the ultimate stress level is given by the relation shown in Equation 2.2 assuming non-linear elastic isotropic behavior for uncracked concrete.

$$\varepsilon = \frac{\sigma_{ij} - \sigma_{oct} \delta_{ij}}{2G_S} + \frac{(\sigma_{oct} + \sigma_{id}) \delta_{ij}}{3K_S} \quad (2.2)$$

Where, σ_{ij} is the specific stress level,
 σ_{oct} is hydrostatic stress,
 σ_{id} is equivalent internal hydrostatic stress for the change in volume due to deviatoric loading,
 δ_{ij} is the Kronecker delta,
 G_S and K_S are the secant shear and bulk modulus respectively.

Subsequently, the stress is calculated using the incremental stress-strain relation $\sigma = D\varepsilon$ where D is the rigidity matrix. This rigidity matrix depends on the state of the integration points which can be uncracked or cracked and the number of cracks. For cracked concrete, the rigidity matrix is multiplied by normal retention factor, $\beta_\sigma = 0.0001$, and shear retention factor, $\beta_\tau = 0.1$ [9].

The fracture criterion is the limit beyond which the fracture process changes from internal micro cracking to visible macro-cracking. It defines the ultimate stress level which is dependent on the critical octahedral shear stress, $\tau_{oct,u}$. Crack is formed on a plane with a normal parallel to the direction of the largest principal stress when fracture criterion is exceeded by at least one positive principal stress. In other words, when the octahedral shear stress, τ_{oct} , corresponding to the current state of stress exceeds the maximum allowable stress, $\tau_{oct,u}$, cracking is initiated in a brittle manner neglecting any softening behaviour both in compression and tension [35]. Complete loss of capacity in all direction occurs when fracture criterion is exceeded by all principal stresses. The effect of confinement on deformation and capacity is a direct consequence of the stress-dependent non-linear stiffness moduli and fracture criterion. This effect of confinement and Poisson's ratio on the stress-strain relation are implicitly included in the model [34].

2.3.2 Effect of Confinement

Concrete under uniaxial compression expands laterally and experiences transverse tensile strains resulting in cracking and ultimately leads to failure in concrete. Lateral pressure applied on concrete members can provide confinement to counteract lateral expansions. Confinement effect can be achieved in two ways: 1) directly by applying external loading such as pressure or prestress, 2) indirectly by providing adequate reinforcement which would reach plastic stage as the concrete expands laterally and prevent cracking of concrete [36]. These can be stirrups in beams and columns or flank reinforcement in pile caps.

Confinement serves multiple purposes in reinforced concrete structures such as increasing the strength of the structure and the critical strain which subsequently alters the effective stress-strain relationship as shown in Figure 2.6. It can also increase bond strength and shear capacity which is highly useful particularly in seismic design. Moreover, it keeps the longitudinal reinforcement and concrete core in place during severe deformation increasing ductility and preventing collapse due to concrete crushing. Øystad-Larsena, et al [37] investigated the effect of lack of confinement on the probability of collapse for a design level earthquake through incremental dynamic analysis (IDA). The results showed a significant effect as the probability of collapse decreased from 12% to 1.2% by providing confinement.

The effect of confinement are incorporated in structural design and empirical formulas are provided in different building codes including the FIB model code [18]. Selby and Vecchio [38] developed the modified compression field theory which describes the stress-strain response of reinforced concrete under compression and tension stress states. The theory accounts for increase in the concrete strength and strain due to lateral confining stress and is adopted in DIANA as one of the confinement models. This strength enhancement is modelled by modifying the peak stress of the unconfined concrete.

The Hsieh et al. [39] formula is used to compute the failure surface and the maximum stress that causes failure, f_{c3f} . Solving Equation 2.3 provides a scaling factor which can then be used to compute the f_{c3f} and failure strength f_{cf} using Equation 2.4. The peak stress factor, k_σ is the ratio of failure strength and concrete strength.

$$2.0108 \frac{J_2}{f_c'^2} + 0.9714 \frac{\sqrt{J_2}}{f_c'} + 9.1412 \frac{f_{c1}}{f_c'} + 0.2312 \frac{I_1}{f_c'} - 1 = 0 \quad (2.3)$$

$$f_{cf} = -f_{c3} = s * \min(\sigma_{c1}, \sigma_{c2}, \sigma_{c3}) \quad (2.4)$$

$$f_{c1} = \max(\sigma_{c1}, \sigma_{c2}, \sigma_{c3}) \quad (2.5)$$

$$K_\sigma = \frac{f_{cf}}{f_{cc}} \geq 1 \quad (2.6)$$

Where, J_2 is the second stress invariant of deviatoric stress tensor,
 I_1 is the first invariant of stress tensor,
 f_{c1} is the maximum concrete stress,
 f'_c is the concrete compressive strength,
 $\sigma_{c1}, \sigma_{c2}, \sigma_{c3}$ are the principal stresses,
 S is the scaling factor

Selby and Vecchio [38] stipulate that experimental researches suggest that peak stress factor can be assumed to be equal to the peak strain factor in cracked concrete. However, different factors must be applied in confined concrete since the peak strain increases at higher rate than the peak stress with increasing confining pressure. The peak strain factor can be calculated as:

$$K_\epsilon = 0.2036K_\sigma^4 - 2.819K_\sigma^3 - 24.42K_\sigma + 13.718\sqrt{K_\sigma} + 1 \quad \text{for } K_\epsilon < 3 \quad (2.7a)$$

$$K_\epsilon = 5K_\sigma - 4 \quad \text{for } K_\epsilon > 3 \quad (2.7b)$$

The modified stress strain diagram for confined concrete can subsequently be computed using Equation 2.8 and 2.9.

$$f_p = K_\sigma f'_c \quad (2.8)$$

$$\epsilon_p = \epsilon_0 \left[K_\sigma \left(1 - \frac{f_{c3}}{f_{c3f}} \right) + K_\epsilon \left(\frac{f_{c3}}{f_{c3f}} \right) \right] \quad (2.9)$$

Where, f_p is peak stress (positive value),
 ϵ_p is the strain at peak stress (negative value),
 f_{c3} compressive principal stress in concrete,
 f_{c3f} required f_{c3} to cause failure in presence of f_{c1} and f_{c2}

The ratio of $\frac{f_{c3}}{f_{c3f}}$ measures the degree of non-linearity. For low value of this ratio, the peak strain value almost equals to $K_\sigma \epsilon_0$ and for higher values the strain at peak stress becomes closer to $K_\epsilon \epsilon_p$. The modified stress strain diagram for confined concrete is shown in the Figure 2.6.

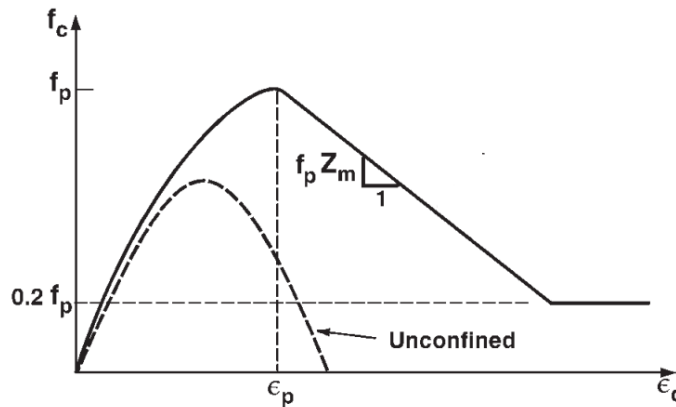


Figure 2.6: Modified stress strain diagram for confined concrete [30]

The descending branch of the stress-strain curve was calculated using Equation 2.10 by modifying the Kent-Park model.

$$f_{c3} = -f_p [1 + Z_m (\epsilon_{c3} - \epsilon_p)] \leq -0.2f_p \quad (2.10)$$

where,

$$Z_m = \frac{0.5}{\frac{3+0.29f'_c}{145f'_c-1000} \left(\frac{\varepsilon_0}{-0.002} \right) + \left(\frac{-I_1+f_{ci}}{170} \right)^{0.9} + \varepsilon_p} \quad (2.11)$$

- Where, f_{c3} is the compressive principal stress in concrete,
 ε_{c3} is the compressive principal strain,
 f_p is the peak stress (positive value),
 ε_p is the strain at peak stress (negative value),
 I_1 is the first invariant of stress tensor
 f_{ci} is the current stress in the principal direction under consideration,
 f'_c is the compressive strength of concrete cylinder (positive quantity),
 ε_0 is the strain in concrete cylinder at peak stress f'_c (negative quantity).

To study confinement in DIANA FEA, a 100x100x100mm solid cube was modeled as shown in Figure 2.7. Horizontal confinement was applied on two side faces and vertical confinement was applied on the top and bottom face. A 5MPa pressure was applied on the remaining two side faces to simulate confinement. The material properties used are shown in Table 2.2. The Poisson's ratio is set to zero to preclude it's effects and observe the effect of confinement alone. The cube was loaded vertically on the top face and modelled using displacement control with load step size of 0.01mm. The model only has one 20-node hexahedral element (CHX60).

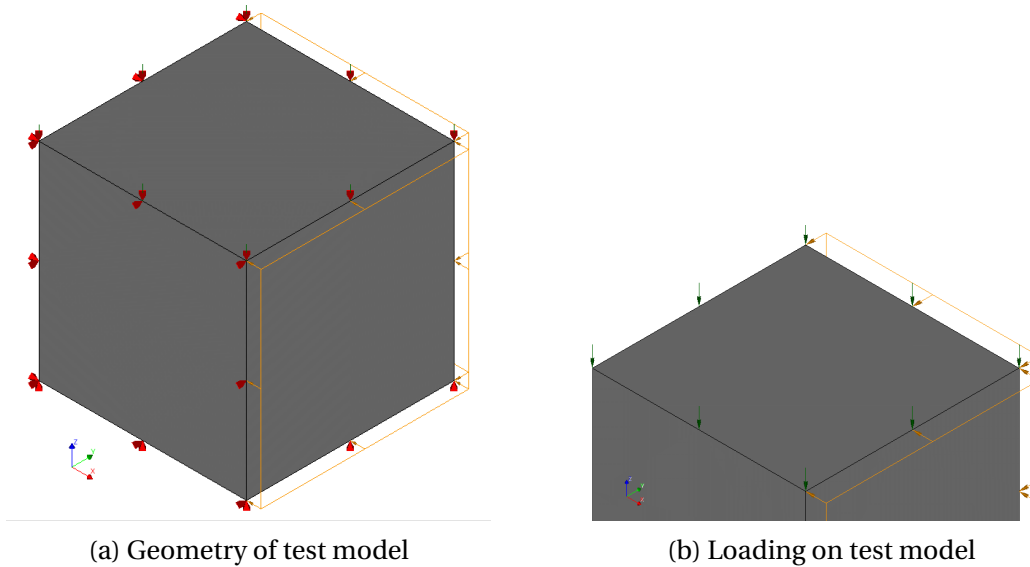


Figure 2.7: Test model for confinement study

Table 2.2: Material property of confinement test model

Parameter	Value
Young's modulus	30 GPa
Poisso's ratio	0
Tensile curve	Elastic
Compression curve	Parabolic
Compressive strength	30 MPa
Compressive fracture energy	35 MPa
Confinement model	Selby and Vecchio

The stress strain diagram was also computed manually to predict the values of the numerical analysis. While the DIANA FEA manual follows the Selby and Vecchio principle explained

earlier, it assumes the peak stress and peak strain factor to be the same, $K_\varepsilon = K_\sigma$. The program calculates principal stresses from the principal strains using $\sigma_c = E\varepsilon_{nst}$ assuming linear elastic behavior. The first stress invariant, I_1 , and second stress invariants, J_2 , are then calculated from the principal stresses using Equation 2.12 and 2.13 respectively. Solving the Hsieh et al. failure surface (Equation 2.3) as quadratic equation results in two values but the positive one is used as scaling factor to calculate f_{c3} . The peak stress and strain factors are then computed as the ratio of f_{c3}/f'_c . The modified stress strain curve are then computed by enhancing both the stress and strains of the unconfined concrete with these peak factors.

$$I_1 = \sigma_{c1} + \sigma_{c2} + \sigma_{c3} \quad (2.12)$$

$$J_2 = \frac{1}{6}((\sigma_{c1} - \sigma_{c2})^2 + (\sigma_{c2} - \sigma_{c3})^2 + (\sigma_{c3} - \sigma_{c1})^2) \quad (2.13)$$

The parabolic compression curve for concrete without confinement was also calculated manually to compare the increase in stress and strain with the confinement model. Fig 2.8 shows that the manual calculations perfectly predict the numerical model for confined concrete. Moreover, comparison between the confined and unconfined model show that the increase in peak stress is much higher than the increase in ultimate strain. It is noted that the increase in ultimate strain is not as high as expected. This can be attributed to the assumption of DIANA that the peak stress and peak strain factor are equal which is different than the assumption of Selby and Vecchio [38].

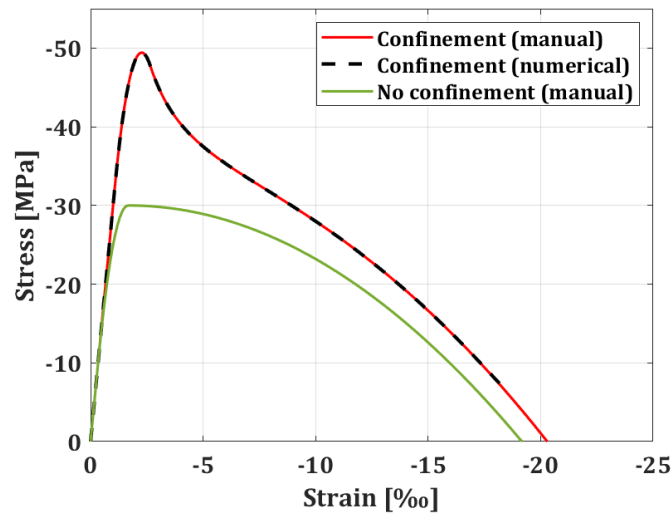


Figure 2.8: Compression stress-strain diagram

In pile caps, the large volume of concrete around the compression struts provides confinement which resists transverse tension. Un-reinforced struts typically fail due to either bearing failure of concrete at the nodes or splitting failure of the struts. However, due to the triaxial confinement of concrete at the nodes, the maximum bearing stress of concrete was found to be at least 1.1 times the concrete compressive strength, thereby eliminating the possibilities of failure of concrete at the nodes [40]. Moreover, larger loads can be resisted by increasing the width and depth of a pile cap. This is because the concrete area at the critical section increases which enhances confinement. In the technical paper titled Design of Deep Pile Caps by Strut-and-Tie Models, Adebar and Zhou [17] concluded that the maximum bearing stress is a function of confinement and aspect ratio (height-to-width) of the compression strut. The authors predicted maximum load carrying capacity of four-pile pile caps with different aspect ratio using the ACI Code [41] and CRSI Handbook [42]. The results show that while for narrow

pile-caps the maximum load is limited by bearing strength, for wider pile-caps confinement is sufficient so that the bearing strength reaches as high as $1.7f'_c$. It was also observed that increasing pile-cap depth increases the strength as shown in Figure 2.9.

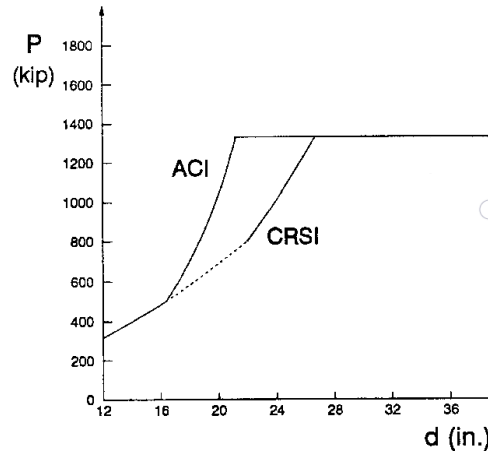


Figure 2.9: influence of pile cap depth on column load [40]

2.3.3 Approach to Model Bond in Reinforced Concrete

The bond behavior is the interaction between reinforcement steel and the surrounding concrete. It is the bond stress corresponding to a certain value of rebar slip. The bond-slip relationship of rebars affects the structural response and governs failure mode of RC elements particularly in members where shear plays a predominant role such as over-reinforced beams. The force transfer from steel to concrete can be attributed to the chemical adhesion between mortar paste and bar surface, friction and wedging action of small dislodged sand particles between the bar and the surrounding concrete and the mechanical interaction between concrete and rebar. While plain bars derive their bond primarily from the first two phenomena, the predominant mechanism in deformed bars is the mechanical interaction [18]. DIANA FEA simulates this interaction of concrete and reinforcement using embedded or bond-slip interface reinforcement.

Embedded reinforcement

This model assumes a perfect bond between the reinforcement and surrounding concrete. The reinforcements are embedded within structural elements called mother elements. The embedded reinforcement does not contribute to the weight of the element and does not have its own degree of freedom. Hence, its strains are computed from the displacement field of the mother element. Moreover, the integration scheme for the reinforcement is also derived from the embedding element [9].

Bond-slip reinforcement

Reinforcement and concrete have the same strain ($\epsilon_c = \epsilon_s$) in uncracked regions where bond stress has developed. In cracked cross-sections, the reinforcement bar transfers tensile forces and bond stresses are generated due to the relative displacement between concrete and steel ($s = u_s - u_c$). This bond allows the force transfer between cracks or along the transmission length of the reinforcement, l_{bpt} . Bond stresses arise in reinforced concrete members from the change in steel force along the length which makes the bond effect pronounced near cracks and at the end anchorage of rebars.

In order to model this behaviour, DIANA assumes a relative slip between the reinforcement and concrete whereby the slip zone is defined by an interface element with zero thickness.

Traction is described as a function of the total relative displacement. DIANA assumes the relation between the normal traction and normal relative displacement as linear elastic while the relation between the shear traction and the slip is assumed to be nonlinear.

According to fib Model Code, the bond stress-slip relationship depends of various factors such as rib geometry, concrete strength, position and orientation of the bar, boundary conditions and concrete cover. Moreover, it is also considerably influenced by reinforcement yielding, cracking along the reinforcement and type of loading i.e. cyclic, repeated or sustained. Yielding of reinforcement, cracking and transverse tension cause reduction in the bond stress while transverse compression increases the bond resistance [18].

Experimental researches indicate that the bond-slip behavior contributes to load carrying and rotational capacity. Sezen's [43] experimental results on double curvature columns showed that the bar slip deformation can sometimes be as large as flexural deformation and can generally contribute 25 – 40% of the total lateral displacement. Experiments done by other researchers such as Kowalsky et al. [44] and Saatcioglu et al. [45] have also corroborated this finding asserting that longitudinal bar slips from strain penetration and the associated rotation can account for as much as 35% of the total lateral deformation in flexural members.

While DIANA offers multiple predefined curves for the relation between shear traction and slip, the Shima and FIB Model Code bond-slip models were studied in this research. The Shima bond-slip model is defined by the constitutive relation as:

$$t_t = a \left(0.9 f_{ck}^{2/3} \left(1 - e^{-40 \left(\frac{\Delta u_t}{D} \right)^{0.6}} \right) \right) \quad (2.14)$$

Where, t_t is the shear traction,
 f_{ck} is the characteristics concrete compressive strength in MPa,
 D is the diameter of the reinforcement,
 a is the optional scaling factor,
 Δu_t is the relative displacement (slip).

FIB Model Code 2010 defines the bond-slip relation by the following piece-wise function:

$$\tau_b = \tau_{bmax} (s/s_1)^\alpha \quad \text{for } 0 \leq s \leq s_1 \quad (2.15a)$$

$$\tau_b = \tau_{bmax} \quad \text{for } s_1 \leq s \leq s_2 \quad (2.15b)$$

$$\tau_b = \tau_{bmax} - (\tau_{bmax} - \tau_{bf})(s - s_2)/(s_3 - s_2) \quad \text{for } s_2 \leq s \leq s_3 \quad (2.15c)$$

$$\tau_b = \tau_{bf} \quad \text{for } s_3 \leq s \quad (2.15d)$$

While τ_b is the bond stress for a given slip, τ_{bmax} and τ_{bf} are the maximum bond-stress and minimum friction traction stress for a given concrete. The FIB Model code also provides parameters to define the mean bond stress-slip relationship of ribbed bars which is detailed in [Table 2.3](#).

Table 2.3: Parameters defining the mean bond stress–slip relationship of ribbed bars [18]

	Pull-out (PO)		Splitting (SP)			
	$\varepsilon_S < \varepsilon_{s,y}$		$\varepsilon_S < \varepsilon_{s,y}$			
	Good bond cond.	All other bond cond.	Good bond cond.		All other bond cond.	
			Unconfined	Stirrup	Unconfined	Stirrups
τ_{bmax}	$2.5\sqrt{f_{cm}}$	$1.25\sqrt{f_{cm}}$	$2.5\sqrt{f_{cm}}$	$1.25\sqrt{f_{cm}}$	$2.5\sqrt{f_{cm}}$	$1.25\sqrt{f_{cm}}$
$\tau_{bu,split}$	-	-	$7.0(\frac{f_{cm}}{25})^{0.25}$	$8.0(\frac{f_{cm}}{25})^{0.25}$	$5.0(\frac{f_{cm}}{25})^{0.25}$	$5.5(\frac{f_{cm}}{25})^{0.25}$
s_1	1 mm	1.8 mm	$s(\tau_{bu,split})$	$s(\tau_{bu,split})$	$s(\tau_{bu,split})$	$s(\tau_{bu,split})$
s_2	2 mm	3.6 mm	s_1 mm	s_1 mm	s_1 mm	s_1 mm
s_3	c_{clear}^1	c_{clear}^1	$1.2s_1$	$0.5c_{clear}^1$	$1.2s_1$	$0.5c_{clear}^1$
a	0.4	0.4	0.4	0.4	0.4	0.4
τ_{bf}	$0.4\tau_{max}$	$0.4\tau_{max}$	0	$0.4\tau_{bu,split}$	0	$0.4\tau_{bu,split}$

1 clear distance between ribs

To compare these two bond-slip models, a pull-out test model was developed on DIANA FEA. A $1m^3$ cube was modelled where all faces were constrained except the positive x-direction. A reinforcement was placed horizontally in the center with a supported connected to its edge node. The length of the reinforcement was calculated according to Eurocode (NEN-EN 1992-1-1:2005) using Equation 2.16 and 2.17.

$$f_{bd} = 2.25\eta_1\eta_2f_{ctd} \quad (2.16)$$

$$l_{b,rqd} = (\varnothing/4) (\sigma_{sd}/f_{bd}) \quad (2.17)$$

Where, f_{ctd} is the design concrete tensile strength according to Eurocode 3.1.6(2)P [5],
 η_1 is coefficient related to quality of bond condition,
 η_2 is coefficient related to bar diameter,
 σ_{sd} the design stress of the bar at the position where anchorage is measured from.

The shear traction was plotted against the slip for both bond-slip models as shown in Figure 2.10. The values were also compared with the ultimate bond stress value according to Eurocode. The FIB model code results in higher bond stress values assuming both good and other bond conditions. The Shima bond-slip also results in higher stress values when the scaling factor is set to 1. Hence, an optimal value of the scaling factor to accurately predict the ultimate bond stress in Eurocode, was derived by equating f_{bd} and t_t as shown in Equation 2.18. It can be noted from Equation 2.14 that for higher values of slip, Δu_t , the influence of the reinforcement diameter becomes negligible and the equation can be simplified to, $t_t = a(0.9f_{ck}^{2/3})$. Moreover, η_1 and η_2 are assumed to be equal to 1.

$$\begin{aligned} a(0.9f_{ck}^{2/3}) &= 2.25\eta_1\eta_2f_{ctm} \\ \text{where, } f_{ctm} &= 0.3f_{ck}^{2/3} \\ a(0.9f_{ck}^{2/3}) &= 0.675f_{ck}^{2/3} \\ a &= 0.75 \end{aligned} \quad (2.18)$$

Where, f_{ck} is the characteristic concrete compressive strength,
 f_{ctm} is the mean concrete tensile strength.

Figure 2.10 shows that modelling the cube using this factor results in a shear traction value equal to the ultimate bond stress according to Eurocode. This value shall be used to model pile caps in this research.

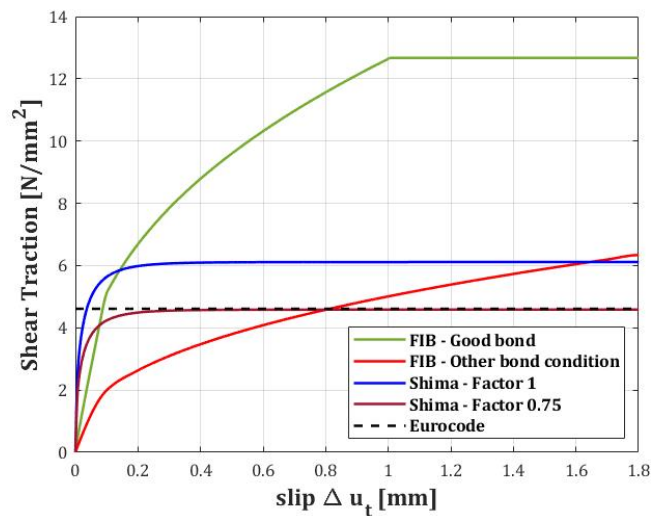


Figure 2.10: Shear traction-slip graphs

2.3.4 Safety Formats

Non-linear FEM analysis is a suitable approach to simulate the real structural behavior and evaluate the resistance of reinforced concrete. According to the FIB Model code, the design resistance assessment can be done using the probabilistic, global resistance or partial safety factor method.

The probabilistic method designs resistance for specific failure probability or reliability index. The global resistance method estimates the resistance based on simplified probabilistic approach assuming significant approximations. The partial safety factor method determines the resistance directly using the values of random variables without evaluation of global safety. The design conditions stipulate that $F_d \leq R_d$, where F_d is the design value of actions and R_d is the design resistance. The code also recommends using at least two methods to provide independent verifications of limit state. This section will only discuss the latter two since they have been recommended by the Guidelines for Nonlinear Finite Element Analysis of Concrete Structures [31].

Global resistance methods

The design resistance is calculated as

$$R_d = \frac{r(f_m \dots)}{\gamma_R \gamma_{Rd}} \quad (2.19)$$

- Where, r represents the non-linear analysis with mean input material
 f_m represents the mean material parameters
 γ_R is the partial factor of resistance specific to the type of safety factor
 γ_{Rd} is the model uncertainty factor equal to 1.06 for well validated numerical models and >1.06 for low-level validation models

Global resistance factor method

The method uses the mean material properties to calculate resistance and takes different uncertainties of steel and concrete into account.

$$f_{cm} = 0.85 * f_{ck} \quad (2.20)$$

$$f_{ym} = 1.1 * f_{yk} \quad (2.21)$$

f_{ym} is the mean yield stress of the steel
 f_{cm} is the mean concrete compressive strength

The partial factor, γ_R , is equal to 1.2. Thus, the global safety factor for steel and concrete is obtained a product of the partial factor and model uncertainty giving a value of 1.27 (fib, 2010).

Method of estimation of a coefficient of variation of resistance (ECOV)

This method is based on the assumption that the random distribution of resistance of RC members can be described by a lognormal distribution of two random parameters: R_m , mean resistance and V_R , coefficient of variation of resistance. It estimates the characteristic resistance as

$$R_k = r(f_{k...}) = R_m \exp(-1.65V_R) \quad (2.22)$$

where r represents the non-linear analysis with mean input material
 f_k represents the characteristic material parameters

The coefficient of variation, V_R , and the global resistance factor, γ_R , are calculated as:

$$\gamma_R = e^{\alpha_R \beta V_R} \quad (2.23)$$

$$V_R = \frac{1}{1.65} \ln\left(\frac{R_m}{R_k}\right) \quad (2.24)$$

where α_R is sensitivity factor for the reliability of resistance equal to 0.8
 β is a reliability index corresponding to the respective consequence class

2.3.5 Previous Pile Cap Models

The internships of Shozab Mustafa and Jayant Srivastava have explored the possibility of reinforcement optimization in two and four-pile pile caps respectively by analyzing the examples from EC 2 in de Praktijk in Diana and comparing the results between the manual results and FEM analysis.

Srivastava [7] in particular developed a three-dimensional half-model of four-pile pile caps shown in [Figure 2.12](#). Total strain rotating crack model is employed to avoid over estimation of failure load from stress locking. Hordijk tension softening curve and the parabolic model are used for the tensile and compressive behavior of concrete respectively. Vecchio and Collins reduction model is used for the reduction compressive strength due to lateral cracking with lower bound reduction factor of 0.4. Reinforcement are modelled both as embedded and truss bond-slip. Both load-control and displacement controlled analysis were developed.

Both attempted to improve the estimation of the internal lever arm 'z' which is one of the most important parameters that affects the pile cap design. The manual calculations determine the force in the tie diagonally which are then decomposed into their orthogonal components to calculate the rebar area required. The lever arm 'z' is therefore the distance between the node under the column and the diagonal force in the tie as shown in [Figure 2.11](#).

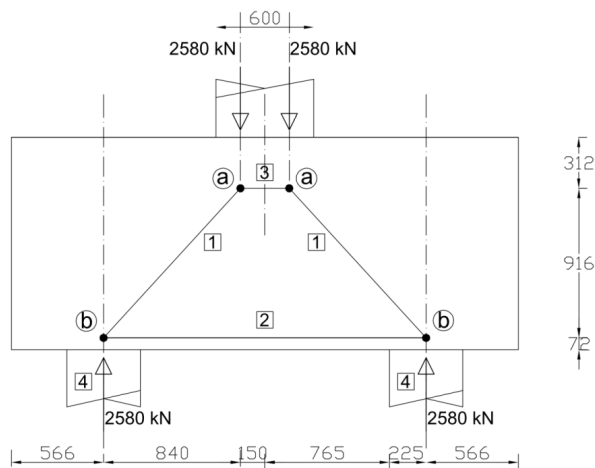


Figure 2.11: Internal Lever Arm in Manual Calculation [8]

To simulate this in the numerical model, the global stresses, S_{XX} and S_{YY} are obtained from the results and their diagonal components are used to determine the diagonal stress state. The stress distribution along the height of the pile cap was then plotted using probing curve and the height of the compression zone was determined. The vertical distance between the centroid of the compression zone and the flexural reinforcement was then measured to obtain the lever arm. Comparison between FEM analysis and manual calculation show that the latter underestimates the lever arm by nearly 15% in four-pile pile caps.

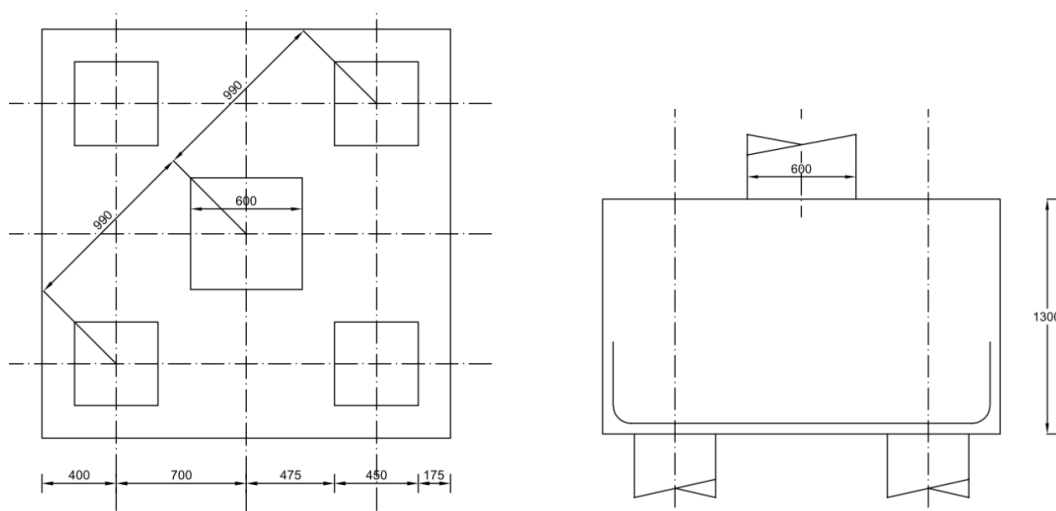


Figure 2.12: Schematic representation of calculated reinforcement in four-pile pile cap [8]

Crack width was determined using the mean relative strain and maximum crack spacing at SLS loading since it cannot be directly obtained as a numerical result when using a smeared cracking approach. Steel stress for crack width is calculated as $\sigma_s = \frac{Load_{SLS}}{Load_{ULS}} * \sigma_{ULS}$. Subsequently, the crack width was calculated following the procedure in section 7.3.4 of NEN-EN 1992-1-1:2005. The crack width was calculated as 0.039mm which was much less than the maximum allowable value (0.415mm) and the manual calculated value (0.337mm).

While the unity checks have shown that concrete is being used to its capacity, the bottom reinforcements are not fully utilized in the four-pile pile caps. The maximum stress in the rebar in ULS in the numerical model show that the main rebar only carry 67% of the manually calculated value. While this can partly be attributed to the difference in the lever arm values, it is

also due to the assumption in the manual design which assumes the tie to be in pure tension. The numerical model show that this is not the case and that the stress in the reinforcement is not constant along the length exhibiting both tension and bending. Moreover, the contribution of the concrete is not taken into account in the manual calculation.

Sensitivity analysis was also performed on the four-pile pile caps to investigate the effect of various parameters such as stiffness of the pile interface, concrete tensile strength, fracture energy and bottom reinforcement. While the pile cap response is found to be highly sensitive to the tensile strength and fracture energy in tension of concrete, changing the flank diameters and the pile stiffness did not have a significant effect on the load carrying capacity of the pile cap. The study concluded that flank reinforcement contributes to the pile cap strength up to a certain limit after which increasing the diameter does not have a substantial effect on the failure mechanism since failure is caused by concrete failure.

2.4 Practical insight from experts

Part of the methodology of this thesis was to gain practical insight from experts by conducting interviews. This was also to understand the practical aspect of pile cap design and collect data from past ABT projects of four-pile pile caps. Six experts from ABT who are or have been involved in the structural analysis of pile caps in practical projects were interviewed. Their response is summarised in this section.

2.4.1 Summary of interview responses

The interviewed experts had experience both with the old Dutch code (NEN 6720:1995) [46] and Eurocode (NEN-EN 1992-1-1:2005) [5]. The old Dutch code was based on the beam theory and specified checks such as stockiness of the structure, bending reinforcement and compression above the pile. On the other hand, Eurocode requires extensive checks including the height of the lever arm, compression above the pile, nodes, struts, ties and introduction of the load going into the pile cap which requires longer computational time. The concrete contribution to the tensile strength in the ties is not taken into account in NEN-EN 1992-1-1:2005. Thus, the old Dutch code resulted in more economic designs than Eurocode. Current design methodology of pile caps in ABT follows the NEN-EN 1992-1-1:2005. While some prefer hand calculations, most experts use excel sheets such as the QEC or ABT Wassenaar sheets. Examples from EC 2 in de Praktijk and Cement en Beton books are also used as references.

The width of the tension zone in pile caps has been an issue of discussion among experts. While the EC 2 in de Praktijk concentrates the reinforcement above the piles within the node width, the QEC sheets uses a larger value (minimum of $2.5 \cdot$ pile dimension or $2 \cdot$ distance between pile center to edge of the pile cap). Even though most experts agree that the latter is more appropriate due to symmetry and sufficient space for anchorage, some believe that the actual width is not significant since in reality the tensile strength will not be strictly limited to this width. Though there might be a slight difference in the value of the strain at the tie and the middle of the cap, the value in the centre is not zero or significantly lower. Moreover, the reinforced concrete is ductile enough to activate a large width of the pile cap. Concentrating reinforcement in the cap also creates execution problems on site. Thus, distributing the reinforcement throughout the width of the cap or concentrating it near the pile without applying reinforcement to the centre are better solutions according to these experts. Some of the highlighted parameters that affect the structural response of a pile cap include:

- Concrete strength and quality
- Width of the tension tie

- Lever arm particularly in SLS
- Diameter of anchorage bend (Doordiameter)
- Introduction of force into and from the pile cap i.e. anchorage length of piles and columns

Although bends and hooks do not contribute to compression anchorages, concrete failure inside bends should be prevented by providing anchorage length less than 5ϕ past the end of the bend or a cross bar with diameter $>\phi$ inside the bend [5].

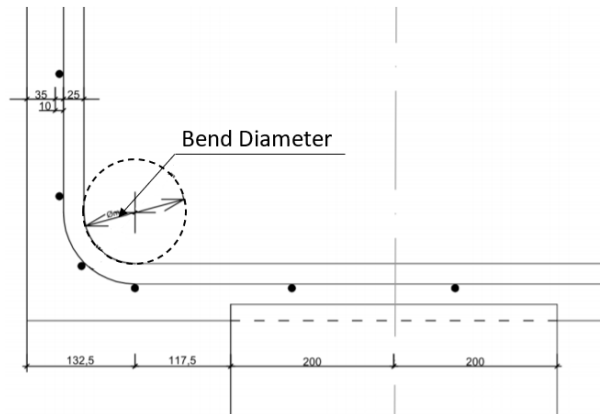


Figure 2.13: Diameter of anchorage bend [8]

Another issue of discussion among experts on pile cap design is the influence of anchorage length and the beginning of anchorage length. NEN-EN 1992-1-1:2005 [5] prescribes the anchorage of the reinforcement in compression-tension nodes starts at the beginning of the node and the anchorage length should extend over the entire node length (EC, 1992). However, some experts highlighted that stocky pile caps act neither as a beam nor a clear STM in practice. As the bending moment lessens from the centre towards the support (piles), so does the tension in the reinforcement which have also been demonstrated in prior Diana models of pile caps. The Eurocode (NEN-EN 1992-1-1:2005) provision is based on the assumption that the same force exists throughout the length. The experts have suggested a more conservative and realistic approach would be to check the residual tension in the bars at the pile and provide anchor for that value. Others have mentioned that they prefer a simplified approach without the reduction of anchor length i.e. starting outside the pile. This will result in a conservative and safe design even in case of human error on site and allows a standardized design in case large number of pile caps needs to be designed.

Some of the challenges mentioned by experts in designing pile caps include calculating anchorage length, flank and shear reinforcement and positioning of compressive node underneath the column. Lack of standardization for optimal design remains an issue due to different interpretations of Eurocode. Moreover, the current design approach does not account for practical issues such as human errors during construction. On the other hand, challenges during construction include fitting the longitudinal reinforcement on the pile cap as it conflicts with the rebar sticking out from the piles. Most experts suggested that the current design approach particularly the detailing of reinforcement should be reconsidered as it's not always necessary.

When checking for maximum allowable crack width, the STM calculates the tie as a purely axial tension bars. k_2 is the coefficient which takes the distribution of strain into account is taken as 1 assuming pure tension instead of 0.5 for bending. This necessitates a lot of reinforcement for crack control and all interviewed experts agreed that this approach is conservative. How-

ever, they had different views on how this should be improved. Some pointed out that using 0.5 would be more appropriate as the realistic behaviour of pile cap during SLS would be a combination of tension and bending action. Others indicated that this would be inconsistent since using the STM approach while assuming the ties as pure bending would be mixing two design theories.

Although optimizing pile design using non-linear FEM could potentially be a supplementary solution to the current design method, its standardized application on large scale and reliability remains in question due to the large number of inputs that influence the results. Moreover, determining the lever arm in SLS would also be challenging. The computational time and cost are also much higher as compared to manual calculations. Acceptance of non-linear FEM calculations for design purposes is currently low as the level of expertise among engineers is still limited.

Investigating the influence of some parameters such as width of the tension bar and anchorage length in FEM would be helpful in future designs as it will help experts understand how critical these parameters are. Other topics of interest highlighted by the interviewees are summarized below.

- Introducing the force from the column to the pile cap cannot always be achieved using only concrete so reinforcement is required. This usually entails the column reinforcement that extends into the pile cap. The force in the reinforcement reduces towards the end of the bar as it transfers the stress to the surrounding concrete. However, it is not clear how much height of the reinforcement or width of the concrete should be taken into account as this is not specified in the Eurocode (NEN-EN 1992-1-1:2005).
- Reinforcement placement during construction is not always the same as the design due to various conditions on site such as the conflict of vertical pile rebars and the longitudinal pile cap rebars. Thus, investigating the influence of rebar shifting outwards or the centre-to-centre distance being less than the calculated value would be of interest.
- Another helpful application of FEM on pile cap design could be to check the safety of existing caps and in case there is a need to construct an additional structure to check how much more load they can carry without collapsing.

2.4.2 Past ABT projects

Appendix A.1 outlines data from past ABT projects of pile-cap designs. All pile were designed using the strut-and-tie model according to Eurocode [5] and EC 2 in de Praktijk [8]. Four of these pile caps were selected based on the following criteria:

1. *Geometry*: a variety of pile cap geometry has been selected ranging from 2.05m to 3.75m
2. *Reinforcement percentage*: the rebar percentage also varies widely ranging from 0.28% - 0.41%
3. *Flank reinforcement*: pile caps with and without flank reinforcement have been selected

Details of the selected pile caps is presented in [Table 2.4](#)

Table 2.4: Detailed data of selected past project

Pile-cap dimension			Column	Pile	Concrete	Reinforcement				Loads	
Name	Dimension (mm)	Depth H (mm)	Dimension (mm)	Diameter (mm)	Concrete Strength	Yield Strength	Flank Rebar	Rebar Grid in x-direction	Rebar Grid in y-direction	Force in Tie F_{dia} (kN)	Design Load F_{ED} (kN)
Nieuwbouw Feringa Building											
NFB-1	2600x2600	1400	450x450	∅ 460	C30/37	435	∅12@100	2 x ∅ 25@125(bottom)		1840	8000
NFB-2	2600x2600	1000						2 x ∅ 12@150(top)			
Ahoy ICC Rotterdam											
NK-1	2000x2000	800	300x300	∅ 400	C35/45	435	∅10@100	2 x ∅ 16@100/150(bottom) 2 x ∅ 12@100(top)		741	3725

2.5 Experiments on pile cap

2.5.1 Experimental studies

Several experiments have been conducted on four pile caps to study the structural behaviour and influence of various factors such as reinforcement ratio and layout on the structural response. However, most of these experiments are done on scaled down specimens as the sheer weight and dimension of full sized pile-caps make testing in the lab difficult. This section describes these experimental researches and their respective findings.

Hobbs and Stein [47] published a paper on the mathematical expression of stress distribution in pile caps and confirmed the results experimentally. The tests were conducted on seventy one-third-scale model pile caps and investigated the relative contribution of bond grip and end anchorage to the pile cap strength. Failure modes of the pile caps ranged from crushing (where the vertical deformation was extremely large) to shear and anchorage failure (for specimens with low quality concrete).

Blévot and Frémy [48] performed comprehensive series of tests on 51 half-scale and 8 full-scale four-pile pile caps. The objective of these tests was to check the efficiency of different STM models and compare the performance of pile caps with different longitudinal reinforcement patterns shown in Figure 2.14. The results demonstrated that, although bundled reinforcement above the piles (Figure 2.14-a) increased load carrying capacity by 20% as compared to a grid pattern (Figure 2.14-e) for the same reinforcement ratio, it led to poor crack control. The researchers recommended the use of complementary grid reinforcement along with this layout for increased strength and better crack control.

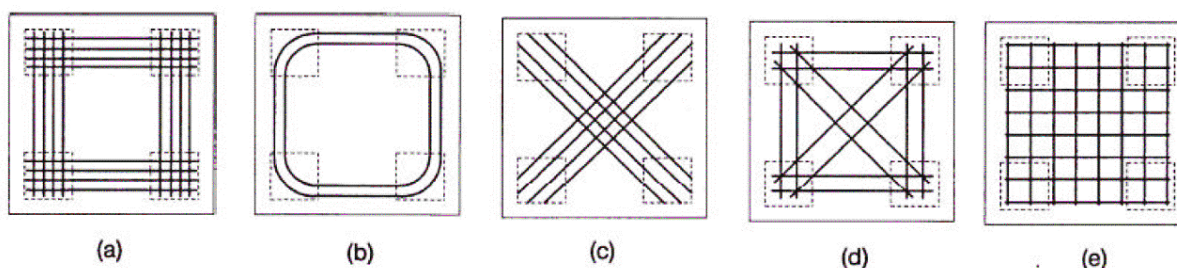


Figure 2.14: Longitudinal reinforcement layouts used by Blévot and Frémy [48]

Clarke [3] tested fifteen half-scale four-pile pile caps with various reinforcement layout (Figure 2.14-a, 2.14-c and 2.14-e) which were designed to fail in flexure. However, only four caps failed in flexure while the rest showed shear failure after the longitudinal reinforcement yielded. The study demonstrated the unsafety of the sectional approach for calculating shear capacity and that the STM was a better method for designing four-pile pile caps. The comparison between the three types of pile caps showed similar results as Blévot and Frémy with the bundled square reinforcement patten showing a 25% increase in failure load.

Sabnis and Gogate [49] publish an experimental study on pile caps in 1984 testing nine scaled down specimens (1/5 ratio) to investigate effect of steel ratio on shear strength. The study demonstrated that while the minimum reinforcement ratio ($2.5\text{‰} - 3.3\text{‰}$) provided by ACI 318-19 [2] code was essential for the development full capacity of the cap, further increase in reinforcement ratio did not improve the capacity. However, this conclusion by several other experiments ([48]; [50]).

An experimental study by Adebar et al. [40] showed that strut-and-tie model describes the behavior of deep pile caps more accurately than ACI 318-19 [2] code provision following the

beam theory. The tests were performed on five four-pile pile caps with different geometries and one six-pile pile cap. It was observed that compression struts did not fail by crushing of concrete in deep pile caps but rather exhibited a strut split failure. A longitudinal split of the struts was a result of transverse tension as the compressive stress spread. The study also concluded that while the shear strength of slender pile caps is dependent on the concrete thickness, bearing area of the concentrated loads is a more important factor to improve shear strength of deep piles.

Suzuki and Otsuki [51] conducted a series of experiments to investigate several aspects of pile cap behavior. The experimental study on the flexural strength included six types of tests on seventy four scaled down samples of four-pile pile caps. The experiments studied the effect of pile arrangement, pile spacing, anchorage and reinforcement layout on bending strength. All samples exhibited failure in bending. The study found that initial crack load is not affected by the ratio and arrangement of reinforcement bars and the strut-and-tie model underestimates the ultimate strength.

Sam and Iyer [52] studied the behavior of four-pile pile caps using three-dimensional non-linear finite element analysis and compared the findings with experimental results on scaled down specimens. The experiments were conducted on three pile caps with the same geometry, material properties and reinforcement percentage but with varying reinforcement layout. The results from these experiments showed that the maximum load carrying capacity of pile caps with slab type reinforcement is higher than those with bunched square and bunched diagonal type reinforcement. The experiments also showed that beam action is predominant at low load levels while strut-and-tie action is prevalent at higher loads.

Suzuki et al. [50] tested 28 four-pile pile caps to investigate the effect of layout of longitudinal bars and edge distance (shortest distance between the periphery of the cap to the pile center). Most of the piles exhibited shear failure after the longitudinal reinforcement yielded. Moreover for the same reinforcement ratio, the ultimate strength with bundled flexural reinforcement arrangement gives an average of 10% higher value as compared to grid-type layout. The research also demonstrated that the edge distance affected the failure load and recommended that $1.5 \times$ pile diameter is the optimal value to increase deformation and load capacity after yielding of reinforcement.

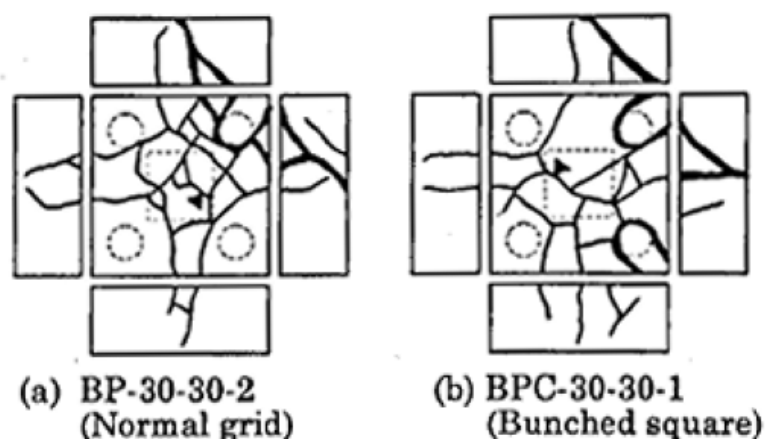


Figure 2.15: Crack pattern of pile caps tested by Suzuki et al. [50])

Two years later, the authors tested thirty four pile caps reinforced with grid layout to evaluate the influence of the edge distance on the structural response particularly the ultimate load and flexural strength as shown in Figure 2.16 [53]. Pile cap depth, column width and edge distance were used as variable parameters. The results showed that the load of the onset of crack and

the flexural capacity decrease when shortening the edge distance.

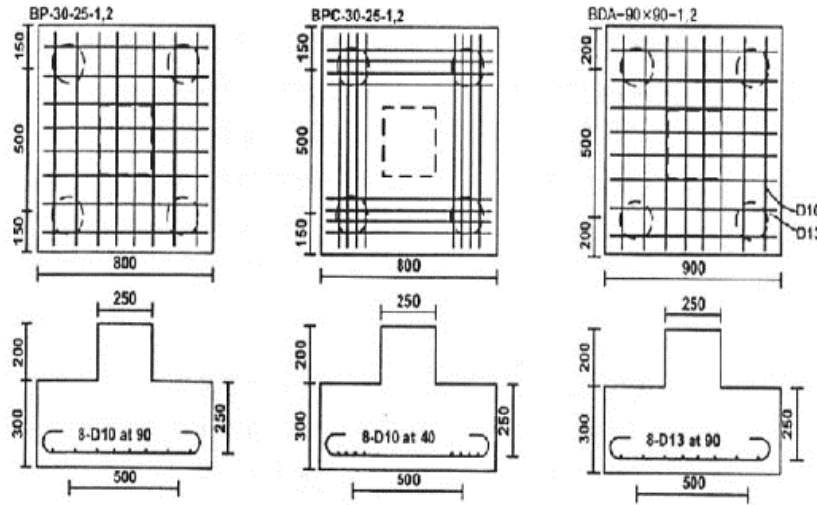


Figure 2.16: Types of four-pile pile caps tested by Suzuki et. al. [53]

A year later, the authors published another paper explaining the influencing of concrete strength and type of anchorage on the strength of four-pile pile caps based on their previous tests [54]. Most samples exhibited corner shear failure and concrete strength was shown to have a small impact. The strain measurement along the reinforcements demonstrated that the rebar is less effective when moving from the pile towards the center as shown in Figure 2.17.

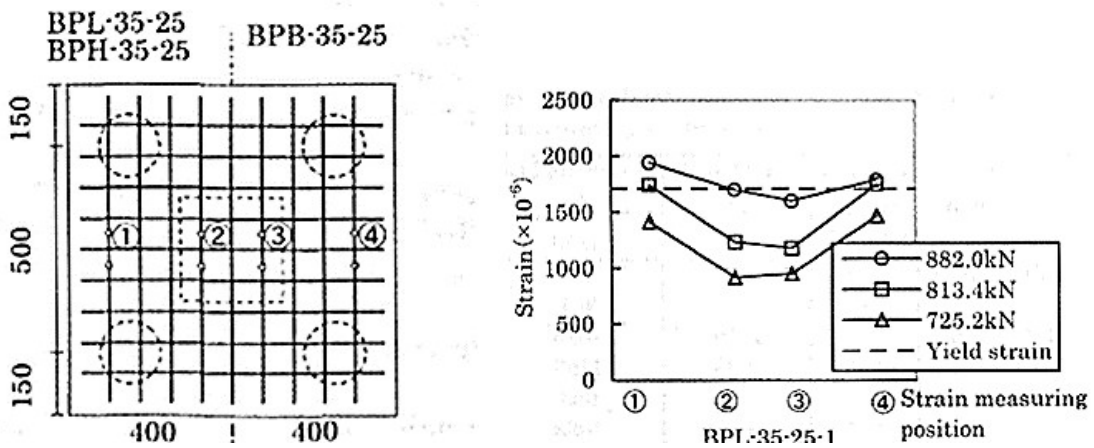


Figure 2.17: Strain distribution of reinforcing bars [54]

Gu et al. [55] tested four pile caps scale down with a ratio of 1/5 to investigate the effect of layout of longitudinal reinforcement. The specimens had the same reinforcement percentage, dimension, material and test procedure. The study found that despite the type of reinforcement arrangement and distribution, deep pile caps failed in shear and corner-pile punching. Figure 2.18 shows the four rebar arrangements in the experiment. The findings of the research regarding the effect of reinforcement arrangement were similar to Wang’s experiment [56].

One of the finding in this research was diagonal rebar layout increases the pile cap strength significantly. CT4-3 and CT4-4 showed a 14% and 11% increase respectively on the ultimate load while CT4-2 showed a less significant increase with 7% as compared to CT4-1. However,

the cracking load for the diagonal reinforcement (CT4-3 and CT4-4) were lower than CT4-1 while CT4-2 recorded an increase by 11%. Thus, the study concluded that CT4-2 was the optimal reinforcement layout considering increase of strength and improvement in ductility.

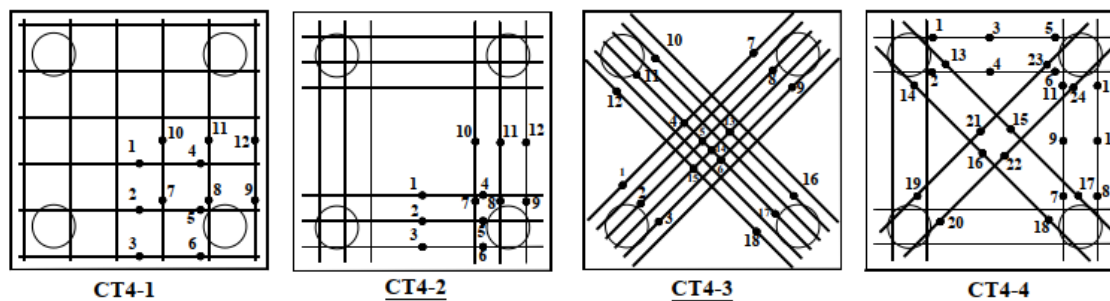


Figure 2.18: Reinforcement layout Gu, et al. in experiment [55]

Ahmad et al. [4] designed four-pile pile caps using STM and tested six scaled down piles experimentally to compare the theoretical and experimental shear capacities. The results demonstrated that the shear strength results from STM were fairly close to the values obtained in the lab showing an average variation of 10%. Cao and Bloodworth [57] studied the shear capacity of RC pile caps by conducting experiments on seven full scale samples with applied wall load. The research looked into the effect of varying shear enhancement factor on shear capacity by changing the longitudinal and traverse pile spacing. The sample with the minimum longitudinal and transverse pile spacing was observed to have the highest failure load.

Wang et al. [56] studied failure mechanisms of five scaled down (600x600mm) thick pile caps with four-piles. The research also investigated the impact of different bottom reinforcement layouts and compressive strength of concrete. The results showed that the load that initiated crack was significantly higher for higher concrete strength while the increase in ultimate load was less noticeable. A comparison between three types of reinforcement layouts: uniformly distributed, bundled at the supports and diagonal bottom bars was also revealed that placing reinforcement diagonally enhances the bearing capacity of the cap slightly but results in lower cracking load.

Lucia et al. [58] studied 21 full-scale pile caps with various shear span-depth ratios and reinforcement layouts to investigate the effect of eccentric loading on the strength of pile caps. The pile caps were loaded centrally with axial load, bi-axial bending and uni axial bending. The results show that pile caps loaded eccentrically have lower load carrying capacity and higher reaction in the piles as compared to those loaded without eccentricity. The study also compared pile cap design methods of the strut-and-tie model and the sectional approach in Eurocode-2 [59] and ACI 318-14 [2]. The research concluded that the strength prediction of strut-and-tie model is much lower than the observed value in the experiments and do not adequately reflect the influence of slenderness and the failure modes. Table 2.5 summarizes the experimental researches discussed in this section.

Table 2.5: Global overview of available experimental data

Name	No. of Pile Caps Tested	Scale		Tested Parameter	Key Findings
		Full	Scaled		
Hobbs & Stein [47]	71		✓	Bond grip and end anchorage	Anchorage can be improved using curved bars; failure can be crushing, shear or anchorage failure
Blévoit & Frémy [48]	59	✓ (8)	✓ (51)	Rebar layout	Bundled layout results in higher failure load but poor crack control
Clarke J. [3]	15		✓	Design approach	STM is better than sectional approach to design pile caps
Sabnis & Gogate [49]	9		✓	Rebar ratio	Rebar ratio above 0.002 doesn't significantly increase strength
Adebar et al. [40]	5	✓		Pile cap geometry	Shear strength depends on concrete thickness or bearing area for slender and deep piles respectively
Suzuki & Otsuki [51]	74		✓	Rebar layout, anchorage and pile spacing	Reinforcement layout and ratio affects failure load but not cracking load
Sam & Iyer [52]	3		✓	Rebar layout	Grid rebar layout increased strength; beam action is predominant at low loads while strut-and-tie action is prevalent at higher loads
Suzuki et al. [50]	28		✓	Rebar layout and edge distance	Bundled rebar layout increased ultimate strength and edge distance affects failure load
Suzuki et al. [53]	30		✓	Edge distance	Cracking load and flexural capacity decrease as edge distance decreases
Gu et al. [55]	4		✓	Rebar layout	Rebar layout doesn't affect failure mode but increases failure load
Ahmad et al. [4]	6		✓	Design approach	Shear capacity values from STM were fairly close to the experimental values with 10% variation
Cao & Bloodworth [57]	7	✓		Pile spacing	Failure load increases as longitudinal and transverse pile spacing decreases
Wang et al. [56]	5		✓	Rebar layout and concrete strength	Higher concrete strength increases cracking load significantly; diagonal placement of rebar increases strength but lowers cracking load
Lucia et al. [58]	21	✓		Rebar layout and design approach	Eccentricity of loading reduces load carrying capacity; STM underestimates strength

2.5.2 Selected experiments for FEM design

Among the experimental researches discussed in [subsection 2.5.1](#), three research papers Suzuki et al. [50], Suzuki et al. [53] and Lucia et al. [58] have been found to have relatively complete data. This refers to how comprehensive the input data and results are logged and presented which includes material properties of concrete and reinforcement steel, test setup, the reinforcement arrangement, load-displacement graph and strain in the reinforcement. Moreover, the experiments in this papers are relevant and within the scope of this research. All pile caps have four-piles with rectangular or square geometry. The reinforcement arrangement is also vertically and horizontally linear (no diagonal arrangements).

Thus, the data from these experiments was analysed based on several selection criteria as shown in [Appendix B.1](#). Although all three papers have reflected the load deflection graph and crack pattern in some of the pile caps, crack width has not been included in the reports. The selected five pile caps are highlighted in [Appendix B.1](#). A variety of pile cap geometry, reinforcement percentage and failure mode has been incorporated by selecting these four pile caps. A more detailed data on the selected pile caps is presented in [Table 2.6](#) and [2.7](#). Both scaled down and full scale models are selected.

Table 2.6: Property of selected experimental pile caps (1/2)

Pile-cap dimension			Column	Pile	Concrete		Reinforcement			Test Results	
Name	Dimension (mm)	Depth H (mm)	Dimension (mm)	Diameter (mm)	Compressive Strength f'_c (MPa)	Tensile Strength f_{ct} (MPa)	Yield Strength f_y (MPa)	Ultimate Strength f_u (MPa)	Rebar Grid	Yield Load P_y (kN)	Failure Load P_{ult} (kN)
Lucia et al. [58]											
4P-N-A3	1150X1150	250	∅ 350	∅ 250	30.0	3.1	573.3	650.9	4x5∅8	689.7	981.5
							519.3	634.7	2x4∅16		
							553.8	641.8	2x2∅12		
							554.8	644.8	2x5∅10		
4P-N-B2	1150X1150	350			25.3	2.8	553.8	641.8	2x3∅12	569.9	872.6
							554.8	644.8	2x5∅10		

Table 2.7: Property of selected experimental pile caps (2/2)

Pile-cap dimension		Column	Pile	Concrete	Reinforcement			Test Results		
Name	Dimension (mm)	Dimension (mm)	Diameter (mm)	Compressive Strength f'_c (MPa)	Yield Strength f_y (MPa)	Ultimate Strength f_u (MPa)	Rebar Layout*	Crack Load P_{cr} (kN)	Yield Load P_y (kN)	Failure Load P_{ult} (kN)
Suzuki et.al. [50]										
BP-30-30-2	800X800X300	300X300	∅ 150	28.5	405	592	2x8 ∅ 10@90	431	907	907
Suzuki et.al. [53]										
BDA-40-25-70-1	700X700X400	250X250	∅ 150	25.9	358	496	2x8 ∅ 10@70	519	862	1019
BDA-40-25-90-1	900X900X400			25.7			2x8 ∅ 10@100	715	1068	1176

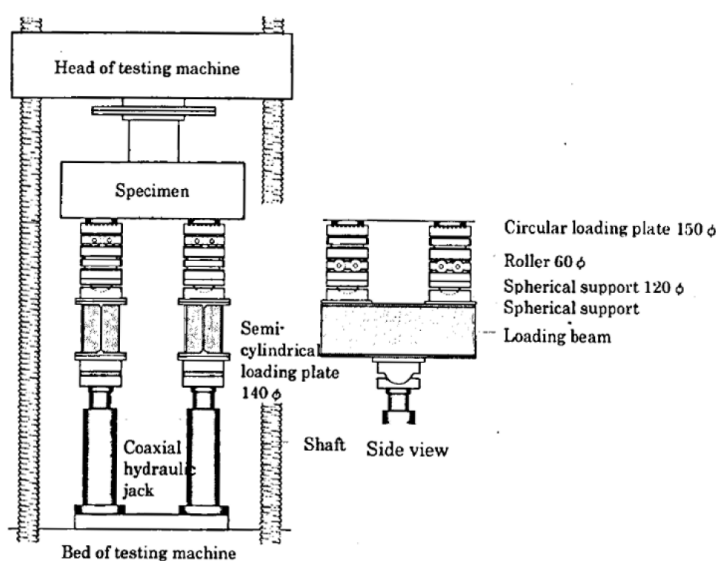
2.5.3 Experimental program

Suzuki et al.

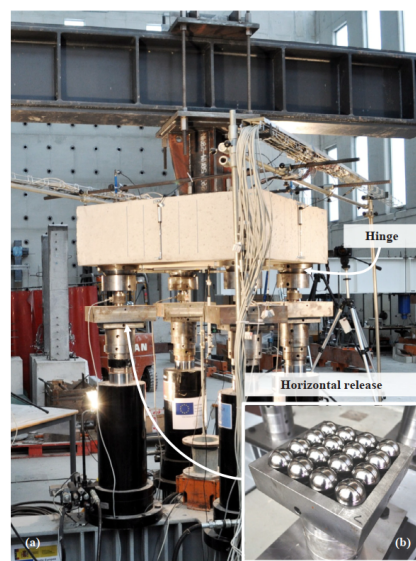
The set up for all Suzuki et al. [53] [50] experiments were identical. An Amsler machine was used to load the pile caps using hydraulic jacks supporting two loading beams as shown in Figure 2.19a. Circular loading plates were used to simulate the piles. A spherical support and two-stage rollers positioned under each pile were used to set the rotation and horizontal translation free respectively. This was to ensure the results would not be affected by unwanted resistance. Central deflection at the bottom pile surface was obtained by deducting the deflection of the supports from the measured deflection at the center point. The cracking load was approximately set as the loading grade under which the first microcrack was detected.

Lucia et al.

The experiments of Lucia et al. [55] were conducted using a hydraulic pressure machine where four independent controlled hydraulic jacks were synchronized to apply a linear distribution of loads to the piles. Perfectly vertical reactions were ensured by means of support devices that acted as hinges and release horizontal reactions as shown in 2.19b. Loading was applied monotonically up to failure at a constant deformation rate of 0.05 mm/s. The vertical displacement of the pile cap was recorded using six displacement transducers (LVDT): one in the bottom centre of the pile cap, one centered on top of the pile cap and four over the piles. The average strains of the main and secondary reinforcement were also measured by LVDT placed along the rebars.



(a) Suzuki et al. [53] [50]



(b) Lucia et al. [58]

Figure 2.19: Test arrangements of selected experiments

2.5.4 Overview of Failure Modes

Five types of failure modes are recorded in the experiments namely flexural, punching shear, corner shear, combined flexure and punching and combined flexure and corner shear failure.

A. Flexural Failure

This failure mode is caused when the reinforcement yields before the concrete crushes. It is a ductile failure where the peak load is sustained while deformation increases before complete loss of capacity.

B. Shear Failure Typical shear failure causes sudden decrease in loading capacity at the peak load with small increase in deflection.

B1. Punching Shear Failure

This failure mode is characterized by reduction of load carrying capacity of the structure below the flexural capacity due to shear. It is a brittle failure which causes a sudden rupture in the structure. Typically, it exhibits clear and wide cracks around each corner piles connecting with inclined cracks on side face of the pile cap.

B2. Corner Shear Failure

This failure is a combination of several one way shear cracks which isolate the four corners of the cap. It is characterized by diagonal cracks on the sides of the pile cap which start from the inner edge of the piles. This results in fracture in which the corner of the footing is chipped off.

C. Combination Failure

C1. Combined Flexure and Punching Shear Failure

This combination is caused when yielding of longitudinal (main) reinforcement is followed by punching shear failure. This is because the flexural resistance of the specimen is greater than its punching resistance.

C2. Combined Flexure and Corner Shear Failure

In this failure mode, yielding of reinforcement is followed by corner shear failure. This failure mode is common when the edge distance (distance between the pile center and the edge of the pile cap) is short.

3. Comparison of FEM Models with Experimental Results

The primary objective of this research is to investigate the application of FEM to the design of pile caps. However, it is imperative to first validate if FEM can actually capture the structural response of pile caps. It is also important to determine what kind of numerical choices must be implemented to get realistic results. Hence, five experimental pile caps are modelled in DIANA to evaluate the accuracy of FEM results compared to experiments.

3.1 Description of Generic Finite Element Model

An initial three dimensional non-linear finite element model of the pile cap BDA-40-25-90-1 from Suzuki et al. [53] was developed using DIANA FEA 10.3. The geometry and reinforcement layout of this pile cap is shown in Figure 3.1. The model was developed to investigate six aspects of numerical analysis namely size of the model, confinement, material model, mesh size, load step and rebar-concrete interaction. The detailing, loading and support condition of the model is discussed in this section.

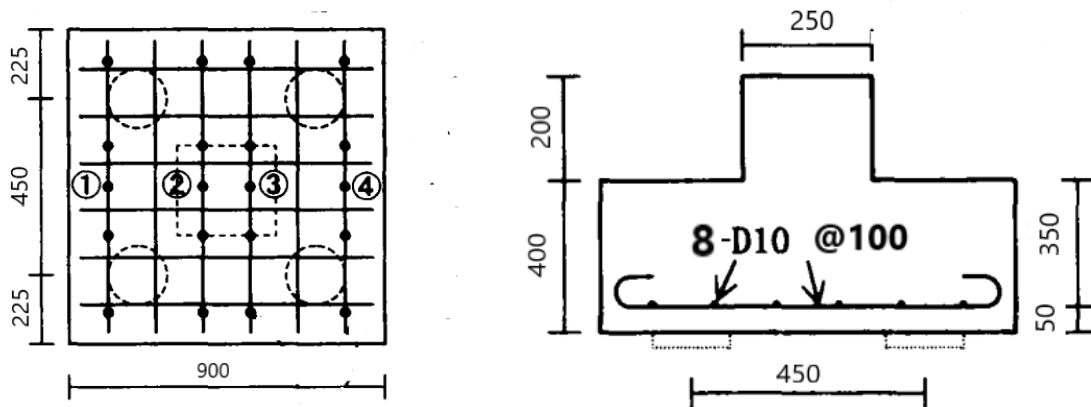


Figure 3.1: Top and side view of the reinforcement layout [53]

3.1.1 Material properties

The column is modelled as a linear elastic isotropic concrete element since its sole purpose is to introduce the load into the pile cap. On the other hand the pile cap is modelled non-linearly using the concrete and masonry material class. The assigned properties of the column and pile cap are shown in Table 3.1. The mean values of the concrete compressive and tensile strength are used to make comparison between the numerical analysis and experiment. The plastic hardening in the reinforcement is modelled using plastic strain-yield stress

model with isotropic strain hardening. Table 3.3 includes the detail material properties of the reinforcement.

Table 3.1: Material properties of column and pile cap

	Column	Pile-cap
Poisson's Ratio	0.15	
Mass Density	2500 kg/m ³	
Material Class	Linear Elastic Isotropic	Concrete and Masonry
Young's Modulus (Concrete)	15 GPa	29.45 GPa
Compressive strength (f_{cm})	n/a	25.7 MPa
Tensile strength (f_{ctm})	n/a	2.04 MPa

3.1.2 Support and boundary condition

Pile Support

The piles are geometrically modelled using steel plates. As discussed in subsection 2.5.3, the experiment restrains only vertical displacement of the pile cap. Thus, the steel plates were only restrained centrally in the vertical direction. Moreover, the thickness of the plate is 200mm which is sufficient enough to prevent high concentration of forces and local deformation in the plate. The experimental set up of Suzuki et al. includes loading beams and multiple layers of steel support as shown in Figure 2.19a. It was observed that using the E_s of conventional steel (200GPa) to model the support was too flexible to simulate the experiment. It was also observed that altering this E_s value only affects the stiffness of the linear elastic range in the load-displacement graph which validates the assumption that the experimental setup of the support is much stiffer than the conventional steel plate. Thus, a factor of 4 (800GPa) was used to attain similar stiffness as the experiment.

Symmetry support

For the quarter model, the appropriate boundary condition was provided on the symmetry faces. The pile cap and column faces parallel to the y-axis are restrained in the x-direction (T1) while the faces parallel to the x-axis are restrained in the y-direction (T2) as shown in Figure 3.4b.

3.1.3 Loading

The pile cap is modelled using displacement-control load. To simplify the post processing, the top face of the column is tied to a node at the edge of the column in the vertical direction (T3) as shown in Figure 3.2. This allows retrieving the reaction (applied) force from one node as concentrated loads. A support is also added at this master node to provide a translation restraint in the vertical direction (T3). A prescribed deformation of 1mm is applied on the master node.

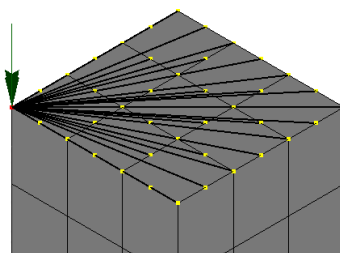


Figure 3.2: Tying on the top face of the column

Each analysis is continued until numerical failure, which corresponds to reinforcement strain exceeding the ultimate steel strain, ε_{su} , concrete strain exceeding the ultimate strain, ε_{cu} (except for local crushing) or the convergence norm of non-linear calculation exceeding 10%.

3.1.4 Meshing

The mesh generating algorithm in DIANA for 3D structures can sometime result in a mesh with sharp edges causing convergence issues. It also has a considerable effect on the accuracy and reliability of the model. Thus, the mesh is generated using a 2D sheet element which are then extruded to give a solid 3D structure.

Following the Guideline for Non-Linear FEM [31], elements with quadratic interpolation of the displacement field are used as they are better to model structures with complex failure modes such as shear failure. Brick 20-node hexahedral (CHX60) element is used as shown in Figure 3.3. This is a twenty-node parametric solid brick element which uses quadratic interpolation and Gauss integration. The element has 3 degrees of freedom per node (u_x, u_y and u_z). The default integration scheme is 3x3x3 in DIANA.

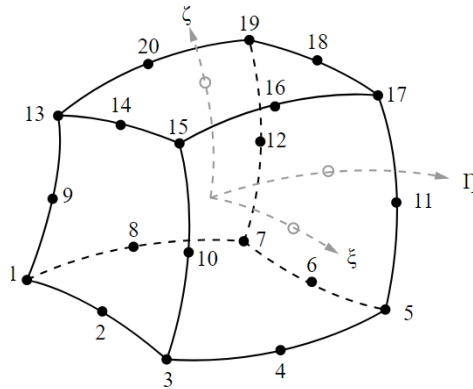


Figure 3.3: CQ48I – 3D Plane quadrilateral interface elements (8+8 nodes) [9]

3.1.5 Iterative procedures

Iterative procedure using regular Newton-Raphson approach is used to balance the internal and external forces with maximum of 50 or 100 iterations. This method evaluates the stiffness relation in every iteration and provides quadratic convergence. This means it requires relatively few iterations but the iterations are time consuming [9].

However, the Newton-Raphson approach resulted in error due to divergence when the pile cap has sudden large drop in stiffness due to fully developed cracks. When divergence occurs, the analysis was automatically aborted. Though it is uncertain why the Newton-Raphson method was unable to obtain convergence, it can be due to complexity of the model. When bond-slip reinforcement is implemented, the reinforcements are also meshed and obtain degrees of freedom which would result in many more equilibrium equations that must be solved. Hence, Secant (Quasi-Newton) method was used for the bond-slip model as it gave stable results. Unlike the regular Newton-Raphson, the Quasi-Newton method does not set up a completely new stiffness matrix for every iteration. The stiffness of the structure is determined from the known positions at the equilibrium path [9]. The secant iterative solution has shown to surpass the effect of local deformations in the equilibrium path [60].

The line search option was switched on in every analysis. The tolerances for the three convergence norms shown in Table 3.2 are specified as per the guideline. It was also specified that all

three norms must be satisfied before moving to the next load step. [Table 3.3](#) summarizes the various finite element modeling choices.

Table 3.2: Convergence criteria

Norm	Tolerance
Force	0.01
Energy	0.001
Displacement	0.9

Table 3.3: Summary of finite element modeling choices

Model Geometry	
Geometry	3-dimensional
Support Condition	
Pile	Steel plate
E_s	800GPa
Thickness	200mm
Loading Condition	
Load Application	Displacement control
Imposed Deformation	1mm
Load Step Size	0.02mm and 0.04mm
Material Models	
Concrete Material Model	
Material Model	Total Strain Crack and Kotsovos Model
Poisson Ratio, ν	0.15
Crack Orientation	Rotating
Tension Curve	Hordijk
Tensile Strength	2.04 MPa
Tensile Fracture Energy, G_f	0.131 N/mm
Crack Band Width Specification	Rots
Poisson Ratio Reduction Model	Damage Based
Compression Curve	Parabolic
Compressive Strength	25.7 MPa
Compressive Fracture Energy, G_c	32.74 N/mm
Reduction Model	Vecchio and Collins (1993)
Lower Bound for Reduction Curve	No reduction and 0.6
Confinement Model	No Increase and Selby and Veccio
Density	2500kg/m ³
Reinforcement Material Model	
Youngs Modulus	200 GPa
Plasticity Model	Von Mises Plasticity
Plastic Hardening	Plastic strain-yield stress
Hardening Hypothesis	Strain Hardening
Hardening Type	Isotropic Hardening
Type	Embedded and Bond-Slip Interface
Yield Strength, f_{ym}	358 MPa
Ultimate strength, f_{tm}	496 MPa
Yield Strain, ε_y	0.00175
Ultimate Strain, ε_u	0.3
Mesh	
Continuum Element Type	Solid brick element
Continuum Element Name	CHX60
Reinforcement Element Type	Truss
Element Size (h)	30mm and 45mm
Interpolation Scheme	Quadratic
Analysis Procedure	
Iterative Solution Procedure	Newton Raphson and Secant
Iteration per Load Step	50 and 100

3.2 Initial investigations

3.2.1 Size of the model

Computational time and cost can be reduced by making use of symmetry in numerical analysis. Thus, two models - full sized and quarter model were developed to investigate this possibility. The geometry of these two models are shown in Figure 3.4. All aspects of the two models is identical including the mesh size.

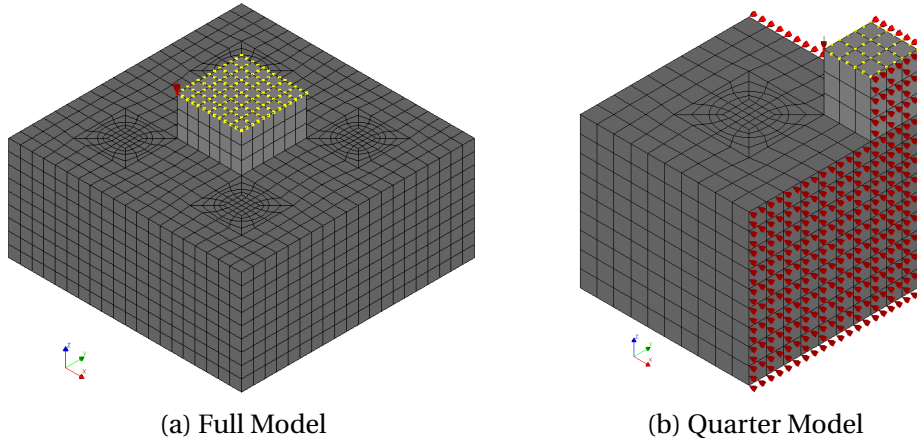


Figure 3.4: Geometry and mesh size of pile cap BDA-40-25-90-1

Comparison between the experimental and numerical load deformation graphs shows that both the quarter and full model carry higher loads for the same deformation before change in stiffness occurs as indicated in Figure 3.5a. To understand the reason behind this, the full pile cap was then modelled using three different tensile strength values as shown in Figure 3.5b. It can be observed that concrete with 1.5MPa concrete tensile strength shows a change in stiffness for nearly the same load as the experiment. This means the tensile strength of the concrete in the experiment is lower than the initially used value in the numerical model (2.04MP) which is derived from the mean compressive strength following the Guidelines for Nonlinear Finite Element Analysis [31].

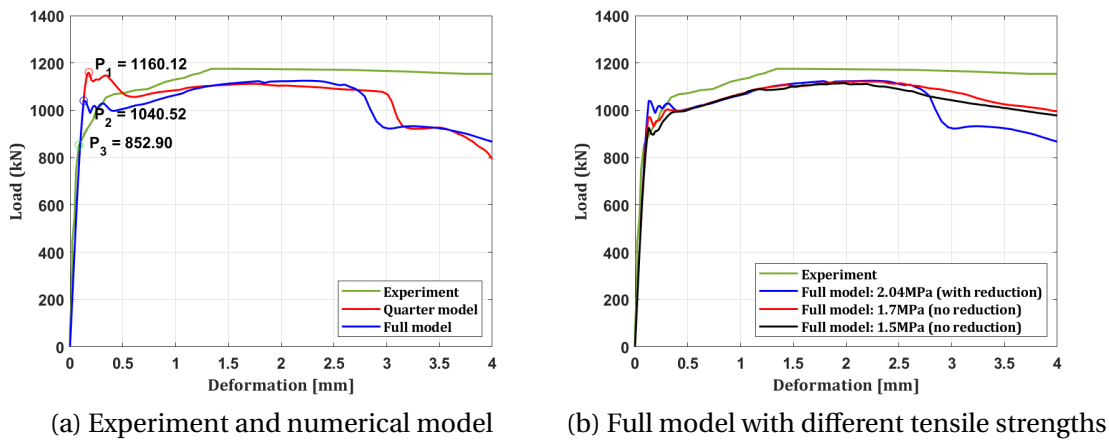


Figure 3.5: Load deformation graphs

The decline in the load deformation graph at the indicated load steps on Figure 3.5a occurs due to a significant decrease in the compression zone and fully developed cracks along the length of the bottom of the pile cap. However, the load at which this occurs is higher in the quarter

model than the full model. Figure 3.6 shows crack patterns for both models at load step P_2 in Figure 3.5a. It can be observed that the full model does not exhibit a purely symmetrical crack pattern and a wide crack is localized in one row of elements along the full length horizontally. Thus, this localization leads to reduction in stiffness in these elements as the stress-strain relationship is further along in the hordijk curve with high tensile strain but low corresponding stress. On the other hand, the crack width in the quarter model is comparatively much lower. The crack pattern of the quarter model is similar to the bottom right quarter of the full model which has no concentrated cracks. As the quarter model assumes perfect symmetry, it is able to carry higher load for the same deformation before reduction in stiffness occurs as can be seen in Figure 3.5a.

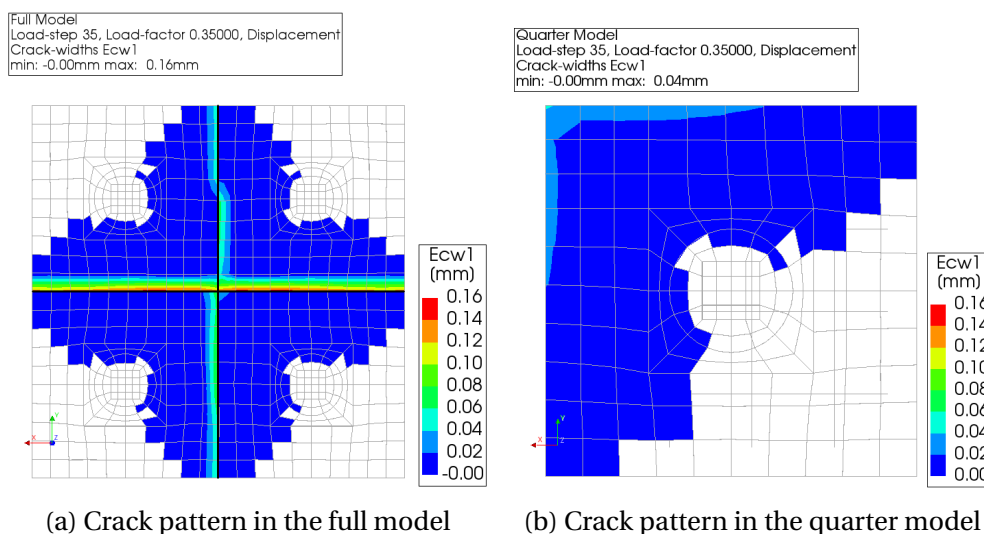


Figure 3.6: Crack patterns at the bottom of the pile cap

Despite this initial differences in the load deformation graph of the quarter and full model, the post yield pattern of the graphs is very similar as shown in Figure 3.5a. Thus, keeping the initial difference in mind, the quarter model can still be used to model the remaining pile caps. The computation time for the full model is more than 12 hours while the quarter model only takes 2 hours which is another incentive for using the latter. The comparison between the crack patterns of the experiment at destruction and the quarter model at the final load step (at 4mm) in Figure 3.7 shows that the two have similarities. In fact, it can be observed that the quarter model resembles Q4 of the experimental pile cap. While the experiment crack pattern is not perfectly symmetrical, wide cracks run across the bottom of the pile cap vertically and horizontally connecting the centers of the opposite sides. Similar cracks are observed on the numerical quarter model in Figure 3.7a. The vertical cracks on the four faces of the pile cap also occur in the quarter model although these are not shown in 3.7a.

Comparison of the load deformation graph of the numerical model and the experiment also reveals that the former exhibits a decline in the load value as the deformation nears 3mm as shown on Figure 3.5a. This is because reduction of compressive strength due to lateral cracking is turned on and modelled using Vecchio and Collins 1993 with a lower bound value of 0.6. Turning this parameter off in the model results in a load deformation graph that has a smoother reduction and resembles the experiment graph as shown on Figure 3.8. Turning this parameter on and off only affects the post peak behaviour and Vecchio and Collins 1993 model in DIANA FEA is observed to over estimate the effect of lateral carking in this pile cap.

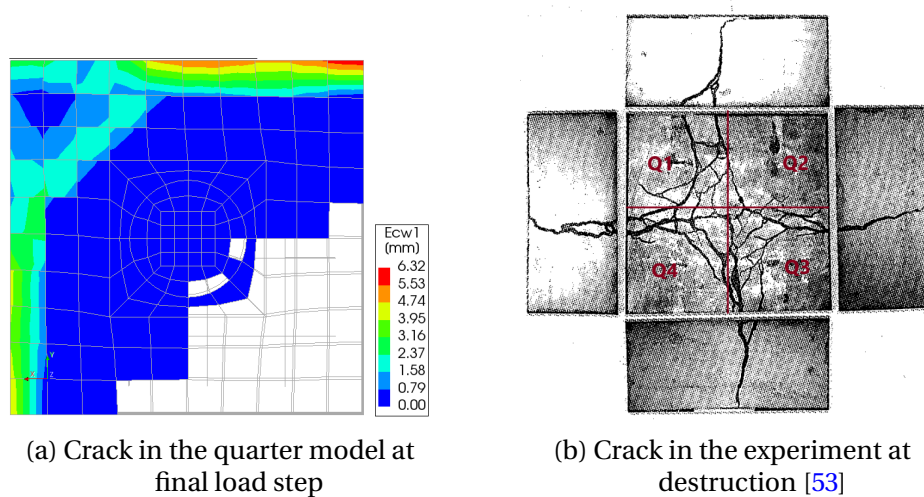


Figure 3.7: Crack pattern of numerical model and experiment

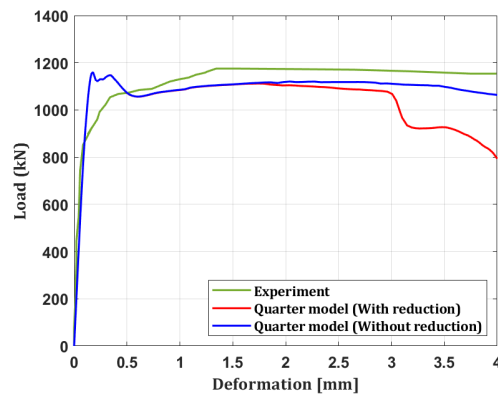


Figure 3.8: Effect of compressive strength reduction due to lateral cracking

3.2.2 Material model

The quarter model was developed using two concrete material models: the Total Strain Crack Model and the Kotsovos Model. For the total strain crack model, a rotating crack is used to avoid over estimation of failure load due to stress locking which can be the case in fixed crack models. Parabolic compression curve and Hordijk tension softening curve are used to model the compressive and tensile behaviour of concrete respectively as shown in Figure 3.9. Rots' element based method is set to calculate the crack bandwidth. Though the graph in Figure 3.9 is plotted assuming constant crack band width of 45mm, the curve within the model might be different as crack bandwidth is individually calculated for each element using the Rots method. Damage based reduction model is employed to account for reduction in Poisson's ratio after crack initiation.

The stress-strain relationship employed in the Kotsovos model is not clearly outlined in the DIANA FEA manual and the only user defined parameter is the concrete compressive strength which is 25.7MPa.

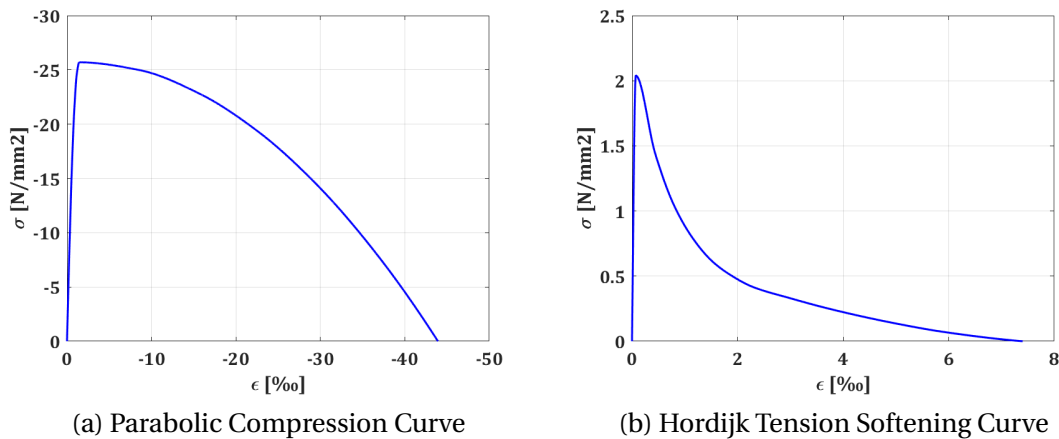


Figure 3.9: Total Strain Crack Model graphs for 45mm crack band-width

Figure 3.10 shows the load deformation curve for the experiment and numerical models using the two concrete material models. Though the graph only shows the data until 4mm deformation to easily draw comparisons with the experiment, it must be noted that the numerical models do not stop at this value. The cracking and yield load for the Kotsovos model is much lower than the total strain crack model (TSCM). The former initially underestimates the loads and gradually results in higher load values for the same deformation than the experiment and the total strain crack model.

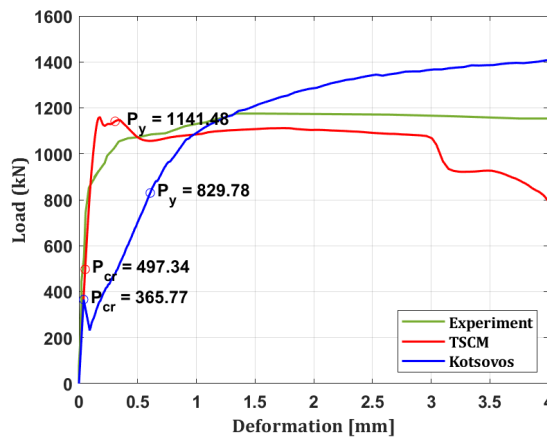


Figure 3.10: Load-deformation graph using different material model

A closer look into the initial cracks of the two models shows that the Kotsovos model exhibits a highly brittle behaviour. Figure 3.11 shows the cracks in both models at the load step where the first cracks occur. In the Kotsovos model, several elements crack at once as soon as tensile strength is exceeded. On the other hand, the total strain crack model shows a few cracked elements at the bottom of the pile cap which gradually increase in size and number. This can be explained by the post-cracking behaviour of the Kotsovos model. Kotsovos [61] stipulates that tensile fracture is characterized by a sudden loss of capacity in a force-controlled experiment since stress redistribution within the concrete structure is not possible once micro-cracks are formed. However, Hordijk et al. [61] mentions that stress transfer is still possible once tensile strength is reached which is defined by the softening section of the tensile stress-strain diagram in Figure 3.12b.

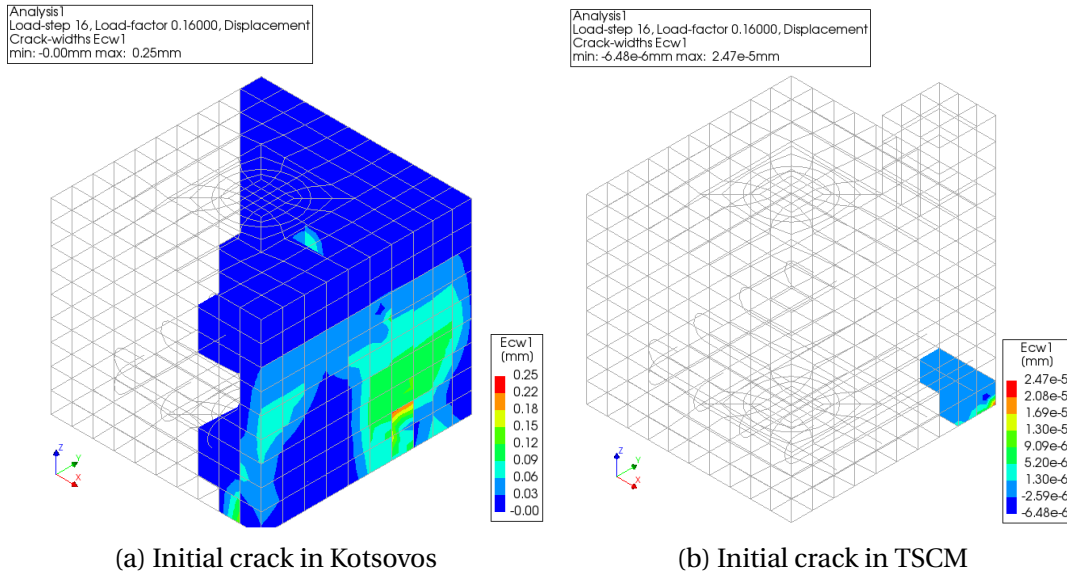


Figure 3.11: Comparison of initial crack patterns between the two models

Thus, in order to gain deeper insight into how the Kotsovos model works in DIANA FEA, two concrete columns, M1 and M2, were developed with dimensions 100x100x1000mm as shown in Figure 3.12a. The two models are identical in all aspects except the presence of reinforcement bar at the centre of M2. This was to compare the behaviour of plain concrete with reinforced concrete. The columns are restrained vertically at the bottom face and loaded in tension at the top. Both models were deformation controlled with load step of 0.01mm. The compressive strength of the concrete was set as 25.7MPa with a mass density of 2500 kg/m³.

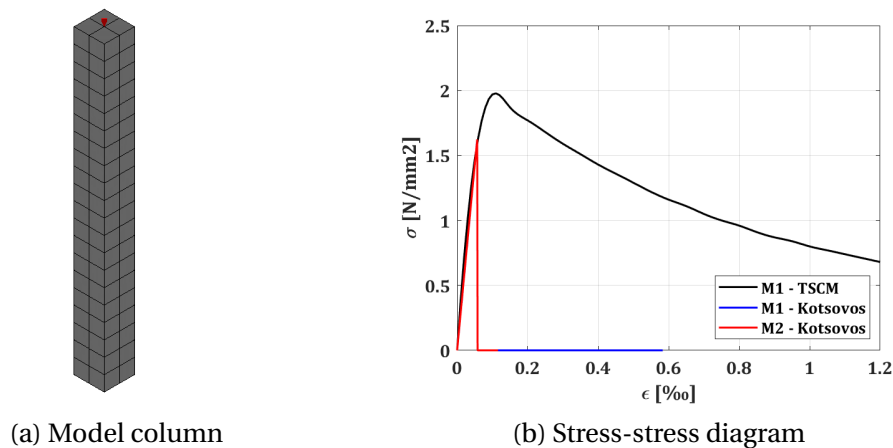


Figure 3.12: Kotosovos material model study

Comparison of the stress-strain diagram between the total strain crack model (using the Hordijk softening curve) and the Kotsovos models reveals that the tensile stress in concrete is underestimated by the latter as shown in Figure 3.12b. Moreover, the Kotsovos graph exhibits a highly brittle behaviour with no tensile softening after the peak stress. This explains the lower cracking load of Kotsovos model in the load deformation graph in Figure 3.10. Both Model 1 and 2 exhibit identical behaviour as the stress-strain diagram overlap. An interesting observation in the plain concrete column, M1, is that the model does not have any crack widths as outputs. This is because crack band width, which is a necessary parameter to compute crack width, is

not stored in DIANA 10.3. Thus, a closer look on the strain distribution on the load steps before and after the peak stress reveals that all elements have equal strain throughout the length of the column as expected from a smeared crack model. On the other hand, the reinforced column, M2, exhibits cracks distributed over the entire length.

The compressive stresses in the strut is investigated to understand the high load carrying capacity of the Kotsovos model. Figure 3.13 shows the principal stress, S3, in the Kotsovos and the total strain crack models at 3mm where the load in the former model is significantly higher. The Kotsovos model exhibits higher stresses in the strut and has a higher compression zone. This implies that the structure utilizes confinement due to the tri-axial stress state. However, the confinement model which is implicitly included in Kotsovos remains unknown.

While the Kotsovos model was initially considered to describe confinement in three-dimensional concrete better, there are still aspects of the model that remain unclear such as how it derives the tensile strength. Moreover, the model exhibits a highly brittle behaviour which significantly affects the structural response of the pile cap including the crack patterns and the load carrying capacity. Thus, the total strain crack model will be used for further modeling purposes.

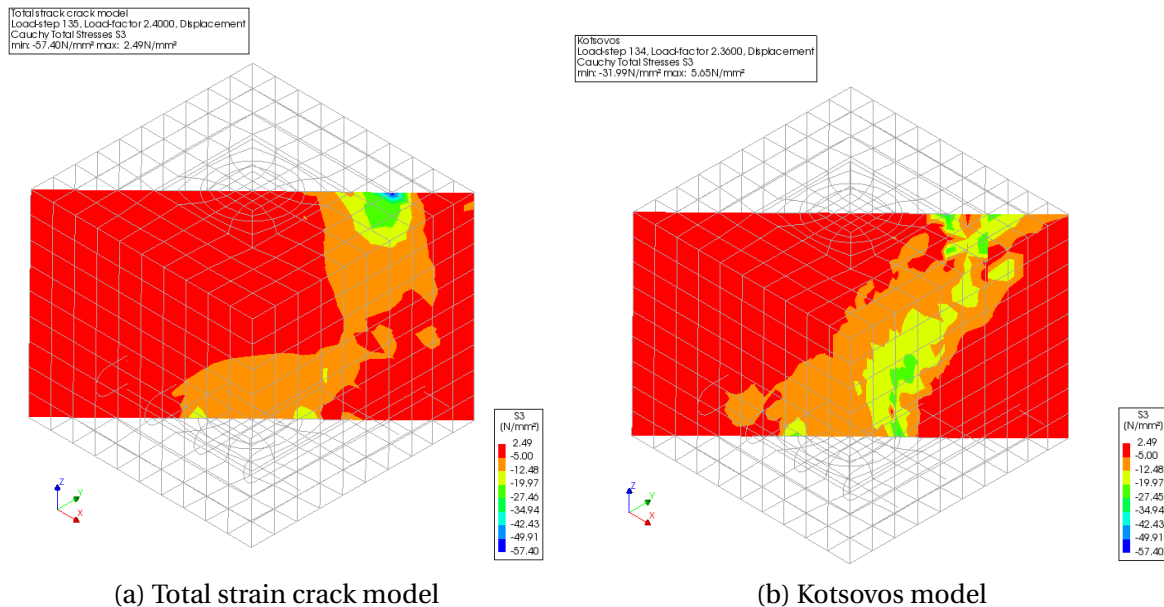


Figure 3.13: Compression stresses at displacement 3mm

3.2.3 Confinement

Two quarter models were developed to study the effect of confinement on the numerical model: one without an increase in stress due to confinement and another using confinement model of Selby and Vecchio. Figure 3.14 shows the load deformation diagrams of these two models. While the model employing confinement has higher load carrying capacity, the increase is not significant.

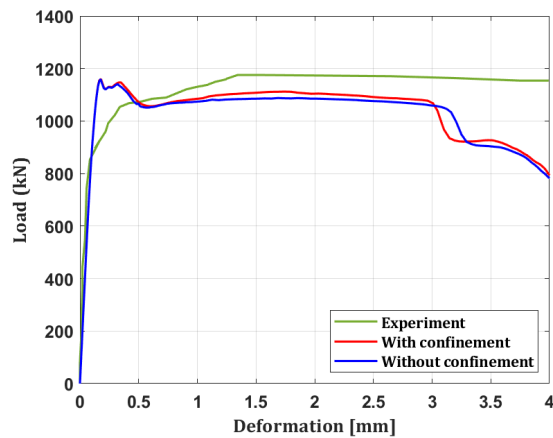


Figure 3.14: Load-deformation graph for confinement vs unconfined

A closer look into the compressive stresses and strains in the struts however shows that confinement results in higher values in both. Figure 3.15 shows the principal stress, S3, at the load step where the unconfined model reaches the compression strength of concrete. While the load and deformation of both models at this load step is the same, the stresses and strains in the confined model shows a significant increase. Hence, confinement model will be employed to model the remaining pile caps.

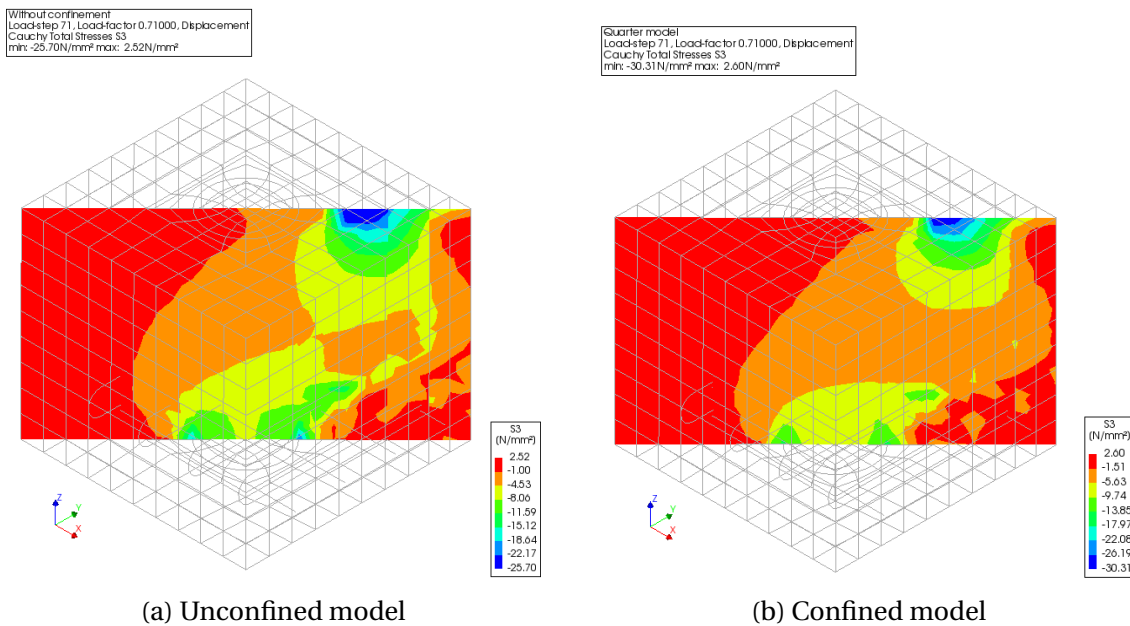


Figure 3.15: Stresses in the compression strut

3.2.4 Mesh Size

The effect of the mesh size on the results of the numerical models was investigated by running two models using 30mm and 45mm mesh. The results show that the mesh size does not affect the pre-peak behaviour and load carrying capacity as shown in Figure 3.16. It does however affect the deformation at which a significant reduction of compressive strength due to cracking occurs. Smaller mesh size means higher ultimate strain in the parabolic compressive curve. Hence, when stress is localized under the column in a few elements, the larger mesh model reaches ultimate strain at a lower load step than the model with smaller mesh size. Hence, the

reduction due to lateral cracking occurs at a lower deformation. For future models, this effect will be considered when choosing the mesh size and analyzing the load deformation graph.

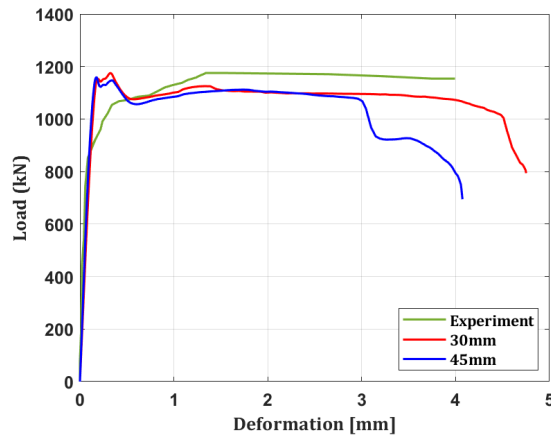


Figure 3.16: Load-deformation graph of models with different mesh sizes

3.2.5 Load Step Size

Two similar models were run with 0.02 and 0.04mm load steps to investigate the effect of the load step size on the numerical results. It is observed that the load step size does not affect the load deformation diagram significantly as shown in Figure 3.17. The computational time for the step size 0.02mm and 0.04mm was three and half hours and nearly two hours respectively. Convergence was achieved in both models for all load steps prior to the stress reduction due to lateral cracking. Hence, the computational time and convergence will be taken into account when selecting load step sizes in future models.

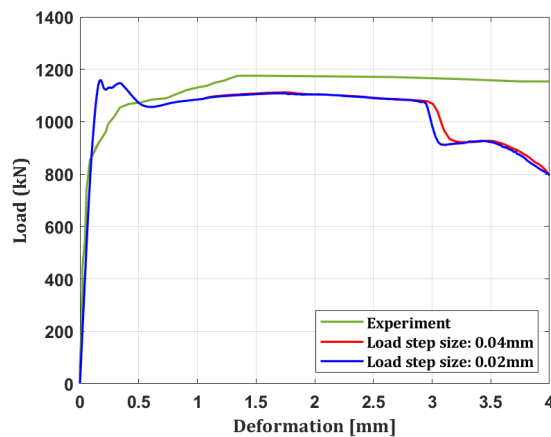


Figure 3.17: Load-deformation graph of models with different load step sizes

3.2.6 Reinforcement type

While the Newton-Raphson iterative procedure was employed for most models, errors due to divergence occur when using bond-slip reinforcement. Hence, the Secant (Quasi-Newton) method was used as it gave stable results with better convergence as discussed in subsection 3.1.5. However, it is noted that the secant iterative approach does not give an entirely smooth graph exhibiting sudden jumps in the load at certain deformations. This can be due to the fact that the Secant method does not set up new stiffness for every iteration but uses

previous solution vectors and out of balance force vectors during the increment to achieve a better approximation [9]. To investigate the effect of the reinforcement type on the structural behaviour of the pile cap, two models were developed using embedded and Shima bond-slip reinforcement which is discussed in subsection 2.3.3.

Figure 3.18 shows the load deformation graphs for these models. Both models have no reduction due to lateral cracking. The graphs show that the Shima bond-slip model results in slightly higher load carrying capacity than the embedded reinforcement and experiment. The decrease in load due to fully developed cracks also occurs at a lower load value in the Shima model. This is because a strain in the cracked elements activates un-cracked elements as the Shima model allows relative displacement between the reinforcement and concrete which increases the progression of cracks in the pile cap.

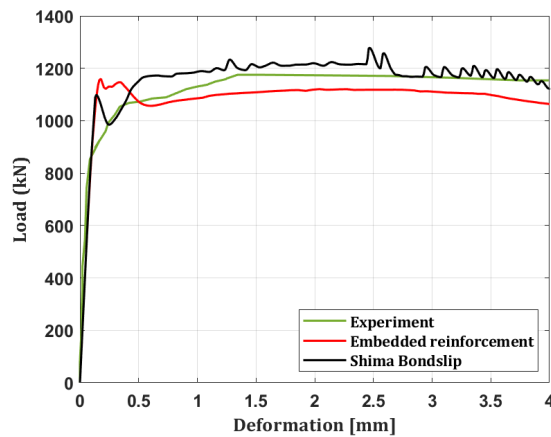


Figure 3.18: Load-deformation graph of models with different reinforcement types

Figure 3.19 shows the comparison between the stresses and strains in the steel between the two numerical models. The figures show s_{xx} and ϵ_{xx} values of node 1 in Figure 3.1 at the integration points. The Shima bond-slip has lower stresses for the same deformation most notably until yield. The strains in steel are also lower in this model as expected since it allows relative slip as opposed to the embedded model which assumes perfect bond between the concrete and the steel. To include this aspect of the reinforcement and concrete interaction, the remaining pile caps will be designed using both embedded and Shima bond-slip.

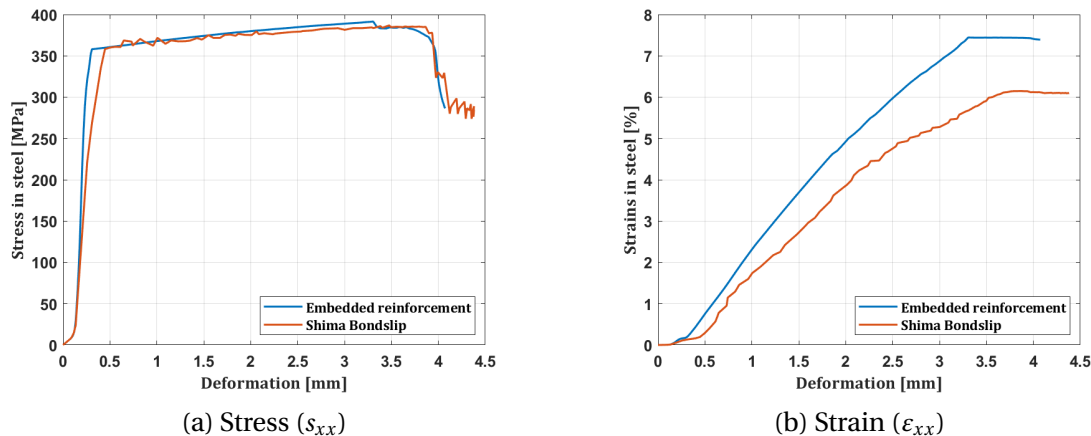


Figure 3.19: Stresses and strains in embedded and bond-slip reinforcement types

3.3 FEM models of experimental pile caps

The four experimental pile caps selected in [subsection 2.5.2](#) are modelled using the modelling choices discussed in [section 3.2](#) and the comparisons with the experimental results are discussed in this section. These four pile caps cover the four of the five failure modes discussed in [subsection 2.5.4](#) namely flexural, concrete shear failure, combined flexure and punching shear and combined flexure and corner shear failure.

3.3.1 Suzuki et al.

The shape, reinforcement arrangement, experimental set up, loading and support conditions of all Suzuki et al. [50] pile caps are the same as BDA-40-90-1 described in [section 3.2](#). The geometry, reinforcement detail and other inputs of these pile caps are specified in [Table 2.7](#).

a. BDA-40-70-1

Pile cap BDA-40-70-1 is similar to BDA-40-90-1 in all aspects except geometry, edge distance and center to center distance between the longitudinal reinforcement which are specified in [Table 2.7](#). Comparison of the load deformation graph of the experiment and numerical model shows that the linear elastic phase is fairly similar. From the initial investigation on BDA-40-90-1 in [section 3.2](#), it is known that the higher load prediction before the change in stiffness is because the quarter model assumes a perfectly symmetrical behaviour throughout the concrete which is not the case in the experiments.

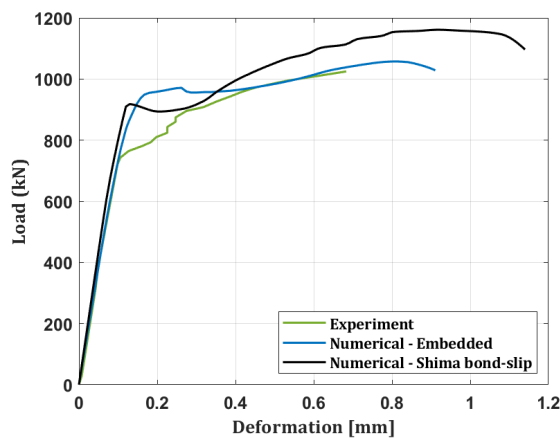


Figure 3.20: Load-deformation graph for pile cap BDA-40-70-1

The failure mode of this pile cap in the experiment is described as corner shear failure. The failure load is reached before much plastic hardening is observed although the reinforcement at the edges have yielded. Diagonal cracks occur on two adjacent faces near the pile penetrates into the pile cap causing the corner to chip off. [Figure 3.21](#) shows the crack patterns in the experiment and the embedded model as both numerical models show similar crack patterns. It can be observed that the both exhibit large cracks near the corner of the pile. The propagation of these piles to the adjacent faces diagonally is also observed in the numerical model. However, while the experiment fails due to punching when one of the corners is chipped off, the numerical model would assume this occurs simultaneously in all four sections.

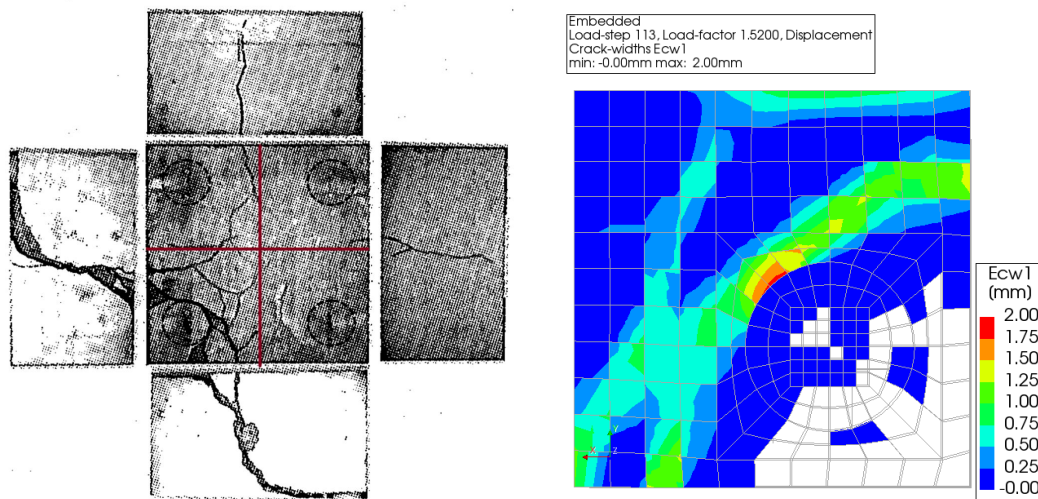


Figure 3.21: Crack pattern of experiment and numerical model for BDA-40-70-1

b. BP-30-30-2

As for the pile cap BP-30-30-2 [53], the concrete and steel material properties are different while the remaining properties remain the same as pile cap BDA-40-90-1. These changed parameters are shown in Table 3.4.

Table 3.4: Concrete and reinforcement material properties

Material Properties	Values
Concrete	
Compressive strength, f_{cm}	28.5 MPa
Tensile strength, f_{ctm}	2.05 MPa
Steel	
Yield Strength, f_{ym}	405 MPa
Ultimate strength, f_{tm}	502 MPa
Yield Strain, ε_y	0.00197
Ultimate Strain, ε_u	0.272

Both embedded and Shima bond-slip models are able to capture the linear elastic phase accurately. However, the non-linear response diverges from the experiment. This occurs when the cracks at the bottom of the symmetry faces are fully developed. The embedded model exhibits a change in stiffness while the Shima bond-slip model decreases in load before change in stiffness. This is because the compression zone in the bond-slip model shows a significant decrease at this load step. This leads to a significant increase in the size and number of cracks at the bottom of the symmetry faces causing a dip in the load deformation graph.

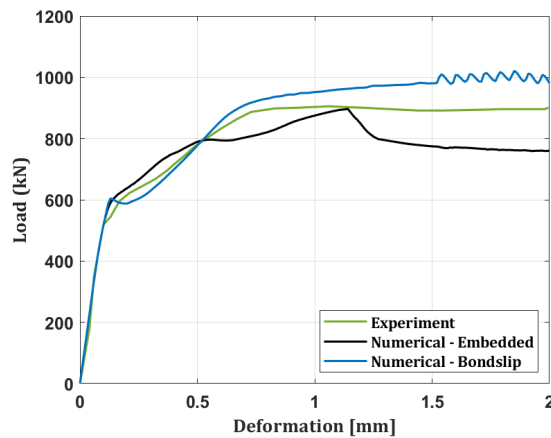


Figure 3.22: Load-deformation graph of pile cap BP-30-30-2

Figure 3.23 shows that the compression zone in the bond-slip model is smaller than the embedded at this load step. Compared to the experiment, the crack and yield load in the Shima bond-slip are respectively 19% and 6% lower. However, it is difficult to determine the load carrying capacity of this model as there are jumps in the load values post 1.5mm deformation. As for the embedded model, the load deflection graphs show another change in stiffness at 0.5mm deformation. This corresponds to the development of cracks throughout the height of the symmetry face under the column. The crack and yield loads of this model are 26% and 15% lower than the experiment but the ultimate load is predicted accurately showing only a 1% difference. Nonetheless, the model does not capture the plastic behaviour of the pile cap. While the load is sustained with increasing deformation in the experiment, the embedded model shows a decrease in the load.

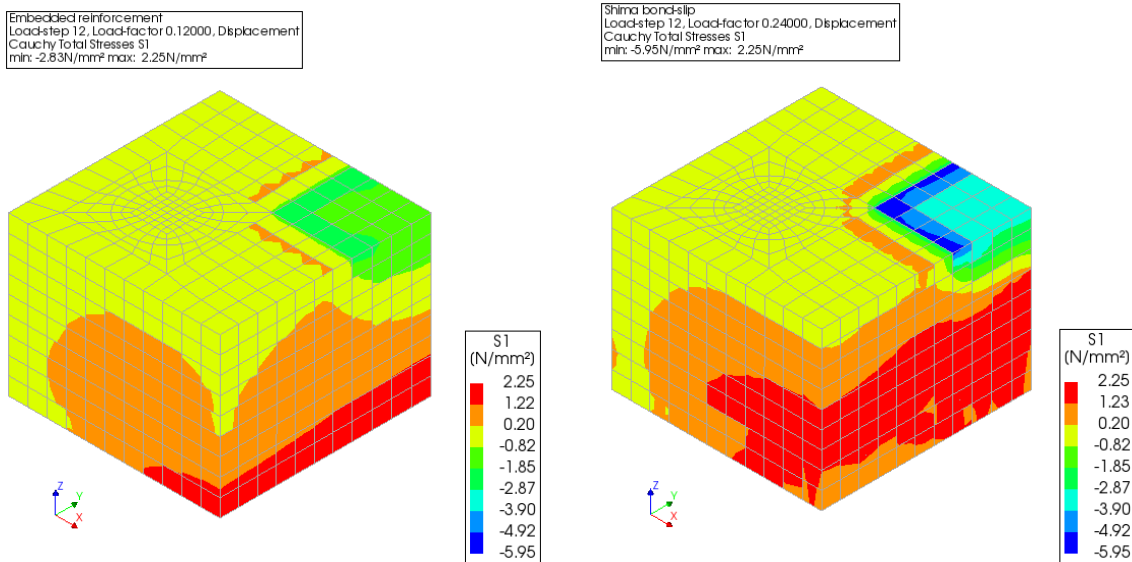


Figure 3.23: Principal tensile stresses in numerical models

Comparison of the crack patterns shows that the embedded model captures the corner shear failure more accurately than the bond-slip model as shown in Figure 3.24. Moreover, it can be observed that the experimental pile caps exhibits diagonal cracks on the side faces that extend from the cracks at the corner of the piles. This is also displayed in the embedded model. Although the bond-slip model shows cracks at the corner of the piles, they are relatively smaller

than the cracks at the symmetry. Subsequently, the failure mode of the embedded model is similar to the experiment, yielding of reinforcement followed by corner shear failure whereas the bond-slip model exhibits combined flexure and punching shear failure.

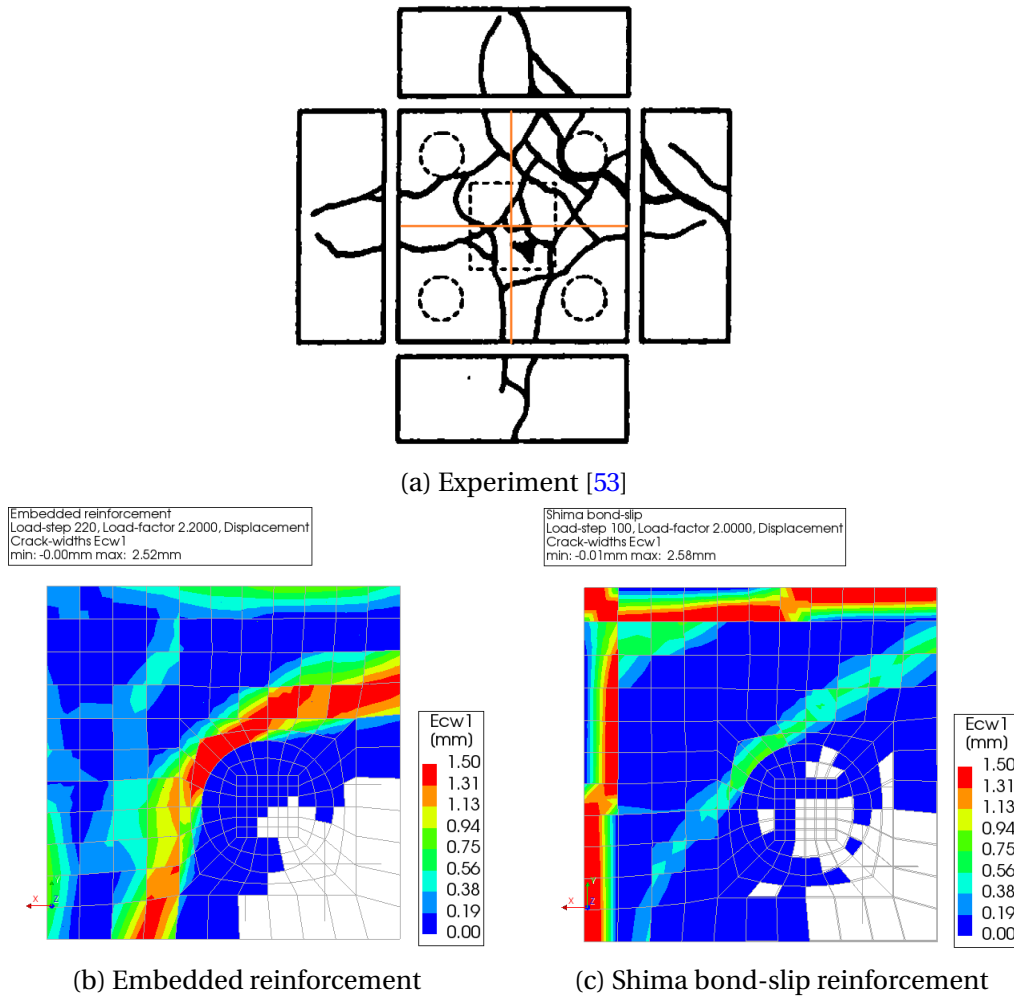


Figure 3.24: Crack patterns on BP-30-30 in the experiment and numerical models

3.3.2 Lucia et al.

The pile caps in this experiment have a standard width and length of 1.15m as shown in [Figure 3.25](#) while the depth ranges from 0.25m to 0.45 . The concrete cover, shear span, pile spacing, pile and column diameter as well as the center to center distance of the reinforcement are also similar for all pile caps.

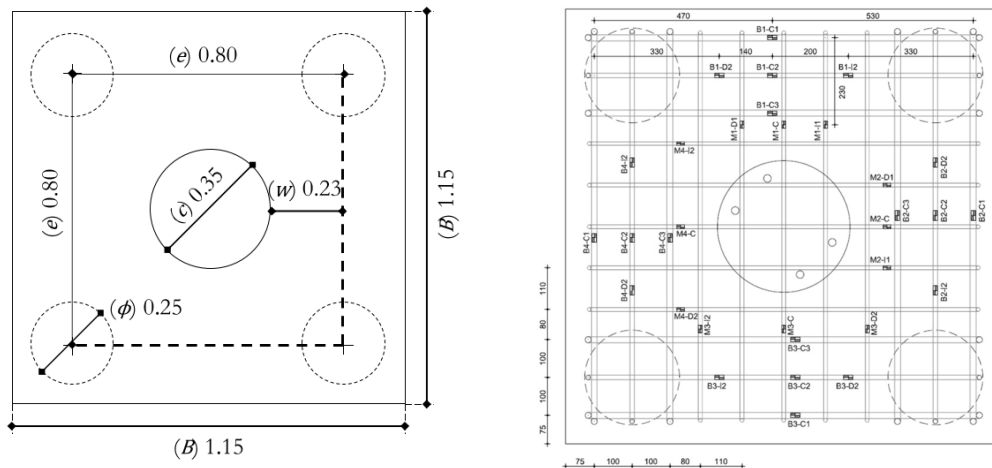


Figure 3.25: Geometry and reinforcement layout of Lucia et al. [58]

While pile cap 4P-N-B2 has only longitudinal reinforcements, 4P-N-A3 has additional shear reinforcement (stirrups) as shown in Figure 3.26. Similar to Suzuki et al. experiments, the piles are modelled using steel plates. Four independent controlled hydraulic jacks were synchronized to apply a linear distribution of loads to the piles at a constant deformation rate of 0.05mm/s. Similarly, the load is introduced as a point deformation on the central node of the pile in the numerical model. Moreover, the column is also modelled as steel plate since the columns in the experiments are circular steel girders as shown in Figure 2.19b. The top face of the column is restrained in the vertical direction to provide vertical support. The symmetry boundary conditions are similar to BDA-40-25-90-1 in Figure 3.4.

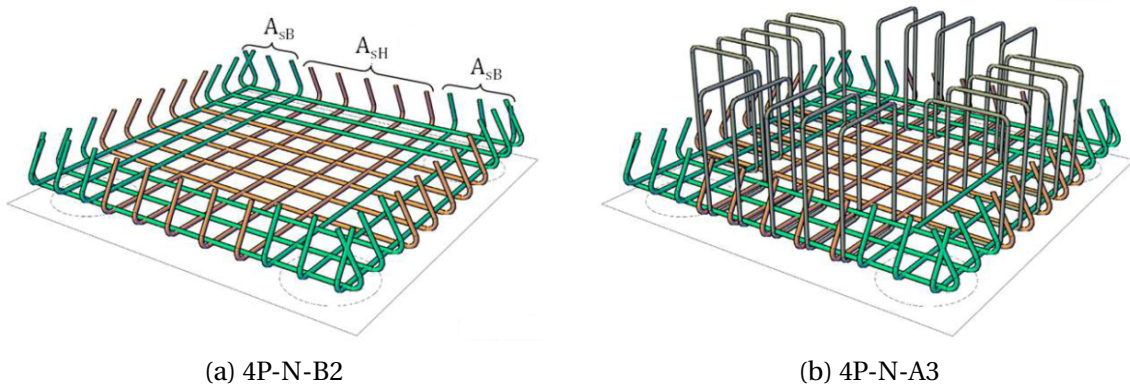


Figure 3.26: Reinforcement detail of the selected pile caps [58]

As the load is applied by synchronizing the hydraulic jacks at each pile, this leads to small differences between the reactions of each pile. Subsequently, the load deflection curve of the pile cap in this series is plotted as pile reaction of the pile with the maximum load against its vertical displacement. Hence, the total load carrying capacity of the pile caps is slightly more than four times the reaction.

Table 3.5: Concrete material properties

Property	4P-N-A3	4P-N-B2
Material Class	Concrete and Masonry	
Material Model	Total Strain Crack Model	
Poisson Ratio, ν	0.15	
Density	2500 kg/m ³	
Crack Orientation	Rotating	
Tension Curve	Hordijk	
Tensile Strength, f_{ct}	3.1 MPa	2.8 MPa
Tensile Fracture Energy, G_f	0.135 N/mm	0.131 N/mm
Crack Band Width Specification	Rots	
Poisson Ratio Reduction Model	Damage Based	
Compression Curve	Parabolic	
Compressive Strength, f_c	30.0 MPa	25.3 MPa
Compressive Fracture Energy, G_c	33.7 N/mm	32.6 N/mm
Reduction Model	No Reduction	
Confinement Model	Selby and Veccio	

a. 4P-N-A3

A key difference between pile cap 4P-N-A3 and the rest of the analyzed pile caps is the presence of shear reinforcements (stirrups) as shown in Figure 3.26b. Figure 3.27 shows the load deformation response of the numerical models and the experiment. The linear elastic phase of both embedded and bond-slip models coincides with the experiment. Although, change in stiffness due to crack occurs at slightly higher load in the numerical models, the tension stiffening portion aligns with the experiment.

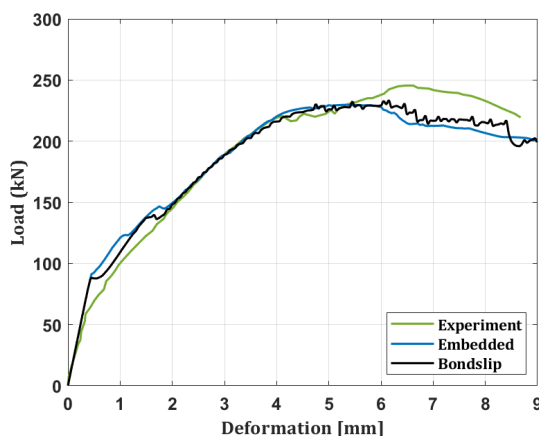


Figure 3.27: Load-deformation graph of pile cap 4P-N-A3

Table 3.6 shows the yielding loads of the main longitudinal reinforcement, denoted as A_{sB} in Figure 3.26a, and shear reinforcements as well as the failure load. It is observed that the embedded and bond-slip models over estimate the yield load of the longitudinal reinforcement by 25% and 23% respectively. On the other hand, both models show a 5% difference in the peak and stirrup yield load when compared to the experiment.

Table 3.6: Comparison of yielding and ultimate load of 4P-N-A3

	$V_{y,B}$ (kN)	$V_{y,V}$ (kN)	V_u (kN)
Experiment	689.70	947.88	981.50
Embedded Model	864.61	898.94	919.08
Bond-slip Model	845.37	897.00	933.514

$V_{y,B}$: Yield load of the main longitudinal reinforcement,
 $V_{y,V}$: Yield load of the stirrup, V_u : Peak load

During the experiment, it was observed that bending cracks initially appear on the lateral faces and propagate through the base towards the pile cap center. In pile cap 4P-N-A3, the first of these cracks denoted as 1 in Figure 3.28a appear near pile R4 and move towards R3. Similar phenomenon is observed in the other faces as loading continues. As the yielding of the main reinforcement begins, some of the vertical cracks near the piles became diagonal. An increase in resistance and ductility is observed post yielding of main reinforcement. As the failure load was reached, the inclined cracks on the faces progress towards the centre completing an arch shape denoted as 2 in Figure 3.28a. The authors conclude that these cracks indicate the geometry of a potential punching failure surface as shown in Figure 3.28b.

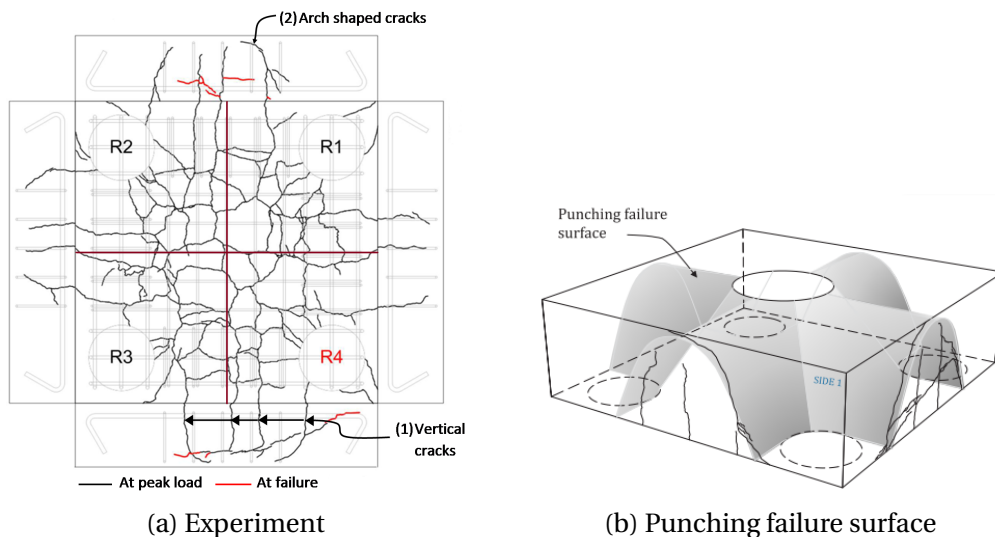


Figure 3.28: Crack patterns and failure surface on 4P-N-A3 in the experiment [58]

In the experiment, although the hydraulic jacks at each pile are synchronised to apply equal deformation, there are slight differences in reaction at the four piles. This would cause one of the piles to have a slightly higher reaction load than the rest. The reaction forces of each pile is measured in the experiment and in this pile cap, pile R4 is recorded to have the highest reaction. Hence, flexural cracks first occur near pile R4. In the numerical model however, the load is applied uniformly in all piles which allows perfect symmetry in the pile cap. Hence, the flexural cracks occur at the center of the faces.

The progression of the cracks in the numerical models after yielding of reinforcement is similar to the experiment. The cracks on the lateral faces become diagonal in both numerical models. Moreover, both models capture the progression of pile caps post peak load. Figure 3.29 shows the cracks on the lateral faces and soffit in the bond-slip model. It can be observed that the arc shaped cracks that were defined as punching failure surface occur on both sides. Hence, it can be concluded that the failure mode of the numerical models is similar to the experiment - flexure and punching shear failure.

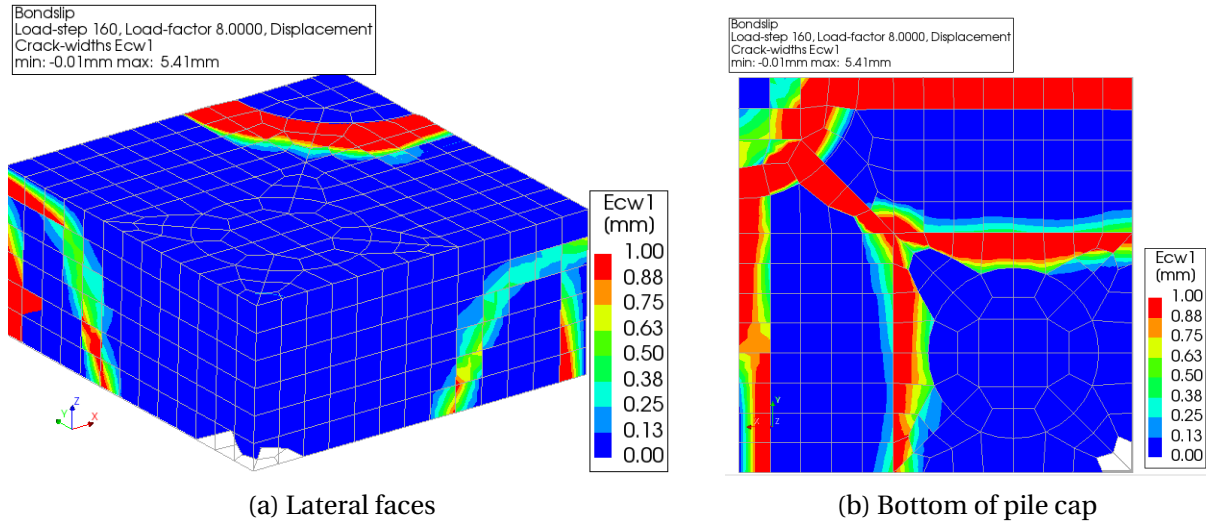


Figure 3.29: Crack patterns on 4P-N-A3 in the bond-slip model

Strain gauges were placed on the main reinforcement as shown in Figure 3.25. The measured strain in strain gauge B1-C2 and B1-C3 is compared with the numerical models in Figure 3.30. The graphs show that initial increase in strain in the numerical models occurs at a higher load value compared to the experiment. Figure 3.27 shows that the change in the stiffness of the graph occurs at a slightly higher load in the numerical model compared to the experiment. This denotes a higher cracking load in the former. As the reinforcement is activated when crack is initiated in concrete, the strain in the rebar increases at a higher load in the numerical model. However, apart from this initial discrepancy, the subsequent values closely resemble the experiment.

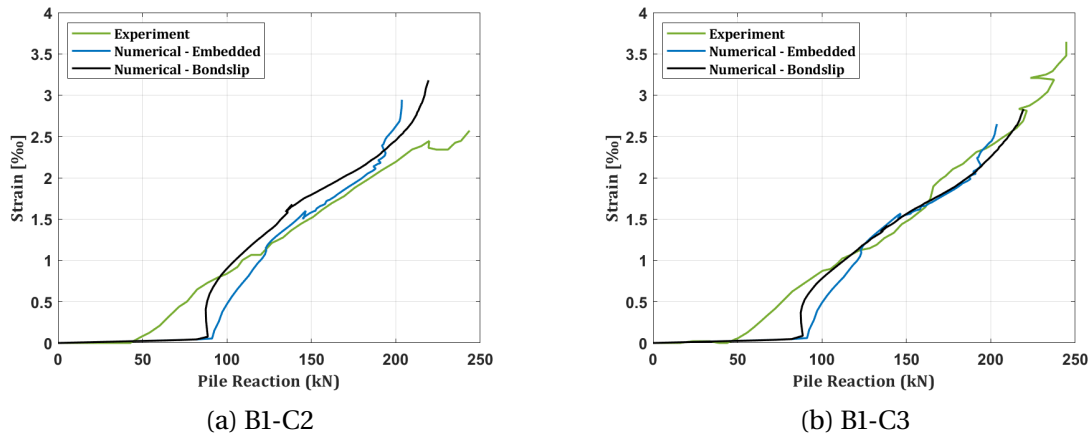


Figure 3.30: Strain in 4P-N-A3 in the numerical model and experiment

b. 4P-N-B2

The reinforcement layout of pile cap 4P-N-B2 is shown in Figure 3.26a. Comparison of the load deflection diagram of the experiment and numerical model in Figure 3.31 shows that the latter over estimates the load carrying capacity. The peak load in the embedded and bond slip models are 14% and 23% higher than that of the experiment respectively. While the initial stiffness of the numerical model matches the experiment, the load at which change in stiffness occurs is higher due to the quarter model. The tension stiffening in the embedded model is

similar to the experiment following an equal slope. The post peak behaviour of this model however varies significantly with the experiment showing a faster decline in the load.

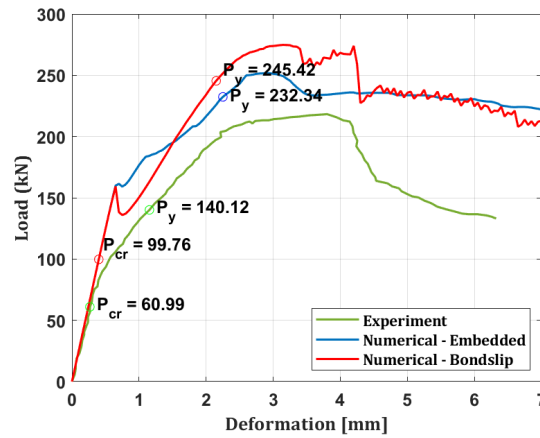


Figure 3.31: Load-deformation graph of pile cap 4P-N-B2

Figure 3.32 shows the strain in strain gauge B1-C2 and B1-C3 in the main reinforcement. It can be observed that the strain in the numerical model is much higher than the values recorded in the experiment. While the strain in the experiment do not show major variation, the strain in the numerical model shows an increase at the load 140 - 160kN. This values correspond the loads at which change in stiffness occurs in the load deflection diagram in Figure 3.31. It can be noted from this graphs that in the experiment, the reinforcements have not been activated in that region until failure load since cracks have not developed near the strain gauges. This explains the significant difference between the two graphs.

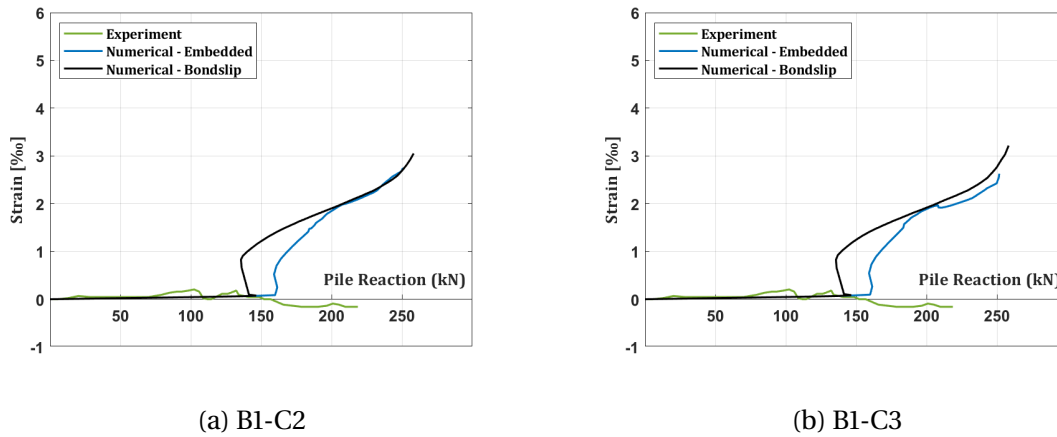


Figure 3.32: Strain in 4P-N-B2 in the numerical model and experiment

Similar to pile cap 4P-N-A3, the failure mode of this pile cap is yielding of reinforcement followed by punching. This is deduced from the vertical bending cracks that extend to arc shaped on the four faces of the pile cap as shown in Figure 3.33. However, since pile cap 4P-N-B2 does not have shear reinforcement, the ductility of the pile cap is much lower. These arc shaped cracks on the pile cap faces also occur in the numerical model. Moreover, the vertical and horizontal cracks along the symmetry faces and the circular crack at the center of the pile cap soffit shown in Figure 3.34 resemble the experiment. However, a concentrated crack at the corner of the pile extending to the adjacent faces of the pile cap is observed. Hence, it can be

deducted that the failure mode of the numerical model is corner shear failure.

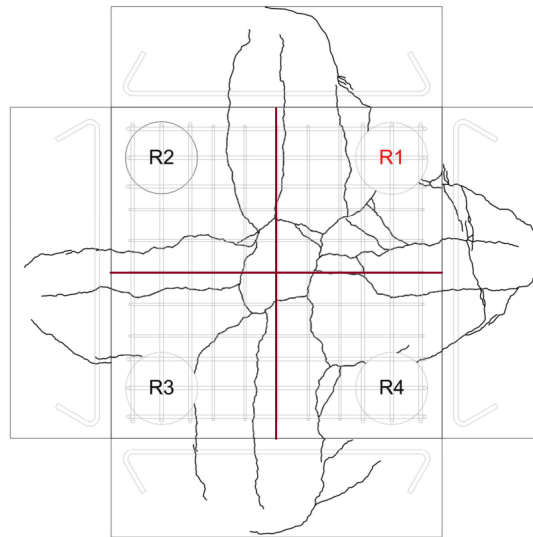


Figure 3.33: Crack patterns on 4P-N-B2 in the experiment [58]

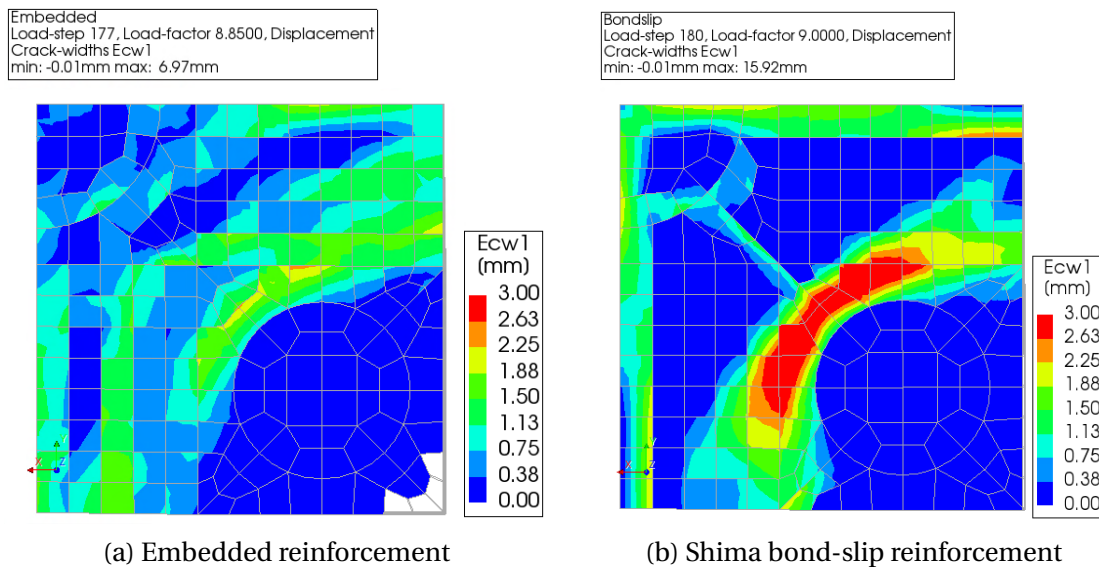


Figure 3.34: Crack patterns on 4P-N-B2 in the numerical models

The difference in the load deflection graph of the numerical model and experiment can be attributed to the load at which reduction in stiffness occurs. Figure 3.31 shows that while the initial crack occurs around 100kN in the numerical model, change in stiffness occurs much later at 160kN. In the experiment however, the initial crack is observed around 60kN and the stiffness changes at 75kN. In the former, change in stiffness in the graph occurs when the cracking has developed along the full symmetry length of the pile cap soffit. This is not the case in the experiment as stiffness reduction occurs before fully developed cracks are obtained.

The discrepancy between the numerical model and experiment can also be explained by the type of failure mode of pile cap 4P-N-B2. Figure 3.35 shows the ductility of different failure modes of pile caps: flexure (f), yielding of main and shear reinforcement followed by punching (Pyw), yielding of main reinforcement followed by punching (Py) and punching (P). Pile caps with ductile failure (f and Pyw) such as BDA-40-90-1 and 4P-N-A3 are predicted by numerical

model well while those with brittle failure such as 4P-N-B2 show a significant difference from the experiment.

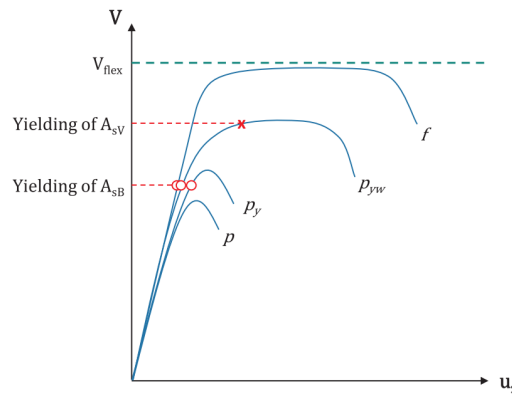


Figure 3.35: Failure modes in pile caps [58]

Hence, the full pile cap of specimen P4-N-B2 was modelled in DIANA to evaluate if it captures the experimental response better. Figure 3.36a shows that though the load carrying capacity is lower than the quarter model, it is still 7% higher than the experiment. A closer look into the crack pattern also shows that the cracks are similar to the quarter model which makes the failure mode corner shear failure. Thus, this shows that better prediction is not necessarily achieved by modelling the full pile cap.

Since the crack width is affected by the fracture energy, the quarter model was also modified by lowering the values of both the tensile and compressive fracture energy to 80% and 50%. It can be observed on Figure 3.36b that lowering the fracture energy lowers the load carrying capacity of the pile cap. The load at which the change in stiffness occurs is also lower and closer to the value in the experiment. Using half the original fracture energy, $0.5G_f$, also results in a failure mode similar to the experiment: yielding of main reinforcement followed by punching. Although this particular model captures the structural response of the experiment better, the reduction in fracture energy is arbitrary and it can't be deducted that reducing the fracture energy by half for pile caps with brittle failure modes will always have similar effect. This however shows that original material model do not capture the full structural response of pile caps with brittle failure.

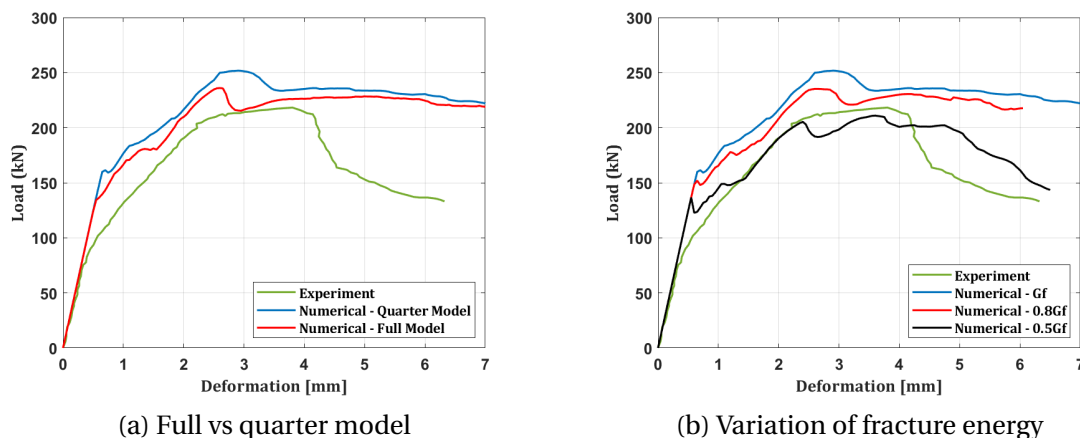


Figure 3.36: Load-deformation graph of variation models of pile cap 4P-N-B2

3.3.3 Comparison with strut-and-tie calculations and experiments

Although pile caps in the Suzuki et al. [50] experiment were initially designed using the bending theory, Jung et al. [62] computed the load carrying capacity of the pile caps using the strut-and-tie model following the ACI 318-14 [63]. The failure loads of pile caps in Lucia et al. [58] were also predicted following the strut-and-tie model in the same code. These values are presented in Table 3.7.

Table 3.7: Comparison of failure load between numerical, STM and experimental results

Pile cap	$V_{u,exp}$ (kN)	$V_{u,STM}$ (kN)	% difference ¹	$V_{u,num}$ (kN)	% difference ²	Failure mode ³
Lucia et al. [58]						
4P-N-B2	861.0	973.3	12.2%	1,007.19	15.7%	F + P
4P-N-A3	973.2	1,018.3	4.5%	933.52	-4.2%	F + P
Suzuki et al. [62] [50]						
BDA-40-25-90-1	1,176	821.98	-35.4%	1,111.93	-5.6%	F
BDA-40-25-70-1	1019	821.77	-21.4%	1,057.45	3.7%	C
BP-30-30-2	907	604.67	-40%	896.84	-1.1%	F + C

¹ Percentage difference between STM and experiment,

² Percentage difference between numerical model and experiment

³ C = Corner Shear Failure; F = Flexural; P = Punching Shear Failure.

Table 3.7 shows the percentage differences of ultimate load capacity in the experiment and strut-and-tie model calculation as well as the numerical model. In the Suzuki et al. [50] experiment, the values from the STM calculations are significantly lower than the experiment and the numerical model results are closer. Thus, it can be deduced that the numerical model is able to predict the load carrying capacity of these pile caps better than STM calculations.

On the other hand, the Lucia et al. [58] experiment shows a slightly different pattern. While the results for pile cap 4P-N-A3 also indicate that the numerical results are closer to the experiment than the STM calculations, results from pile cap 4P-N-B2 show that the STM calculations are slightly closer to the experiment. This can be explained by the difference in failure modes. Pile cap 4P-N-A3 has a ductile failure while 4P-N-B2 has a brittle failure mode. Hence, the structural response of the latter is captured with numerical models less accurately. Table 3.8 shows the ratio of the experimental failure load to the numerical and STM results. It can be observed that the mean ratio of the numerical results is closer to 1. Moreover, the coefficient of variation (COV) shows that the STM results have a greater the level of dispersion than the numerical models.

Table 3.8: Ratio of experimental failure load and numerical and STM results

Pile cap	$V_{u,exp}/V_{u,STM}$	$V_{u,exp}/V_{u,num}$
4P-N-B2	0.88	0.85
4P-N-A3	0.96	1.04
BDA-40-25-90-1	1.43	1.06
BDA-40-25-70-1	1.24	0.96
BP-30-30-2	1.50	1.01
Mean	1.20	0.99
COV	22.9%	8.3%

Lucia et al. [58] also calculated the yielding loads of each pile cap with STM. Table 3.9 shows the the yielding load values obtained in the experiment, STM calculation and the numerical

models. It can be observed that similar to the failure load, the experimental results of 4P-N-A3 are captured well by the numerical model while 4P-N-B2 shows a significant difference. Nevertheless, it is noted that the numerical models are comparatively closer to the experimental values than the STM calculations.

Table 3.9: Comparison of yielding load between numerical, STM and experimental results

Pile cap	$V_{y,exp}$ (kN)	$V_{y,STM}$ (kN)	% difference*	$V_{y,num}$ (kN)	% difference**
Lucia et al. [58]					
4P-N-B2	569.9	930.2	48%	861.6	15.7%
4P-N-A3	973.2	1,018.3	4.5%	933.52	-4.2%

* Percentage difference between STM and experiment,

** Percentage difference between numerical model and experiment.

4. Comparison of FEM Models with STM Results

The second sub-research question of this thesis focuses on how numerical models compare to analytical calculations. Thus, four-pile pile caps that were designed using the STM approach were modelled in DIANA to answer this question. The modelling choices discussed in [section 3.2](#) are used to design pile caps from past ABT projects namely NFB-1, NFB-2 and NK-1. These are summarized in [Table 4.2](#). The geometry and material properties of these pile caps such as concrete strength, number and yielding strength of reinforcement are presented in [Table 2.4](#).

The analytical design of all pile caps follows the calculation in the EC 2 in de Praktijk [8] which is discussed in [section 2.2](#). The CCC-node under the column and CCT nodes above the piles are checked to ensure the stresses in the concrete do not exceed the allowable limit. Similar to the example in EC 2 in de Praktijk [8], the concrete confinement is assumed to be sufficient to withstand the transverse tension perpendicular to the compression struts. This assumption prevents the need for shear reinforcement in the interior of the pile caps. Hence, only flank reinforcement are provided for confinement.

The guideline for Nonlinear Finite Element Analysis of Concrete Structures [31] specifies that the characteristic values of the material properties should be used for SLS analysis while characteristic, design or mean values can be used for ULS. However, since the design and mean values have been used in the STM calculation for ULS and SLS analysis respectively, these values are also used in the numerical models to obtain comparable values. [Table 4.1](#) shows the concrete input values for the different safety formats specified in the guideline.

Table 4.1: Concrete inputs for safety formats

	f_c [MPa]	f_{ct} [MPa]	E_c [MPa]	G_F [$\frac{Nmm}{mm^2}$]	G_c [$\frac{Nmm}{mm^2}$]
Mean	$f_{cm} = f_{ck} + \Delta f$	$*f_{ctm} = 0.3(f_{ck})^{2/3}$	$*E_{c0}(\frac{f_{cm}}{10})^{1/3}$	$73f_{cm}^{0.18}$	250 G_F
Characteristic	$f_{ck} = f_{cm} - \Delta f$	$f_{ctk,min} = 0.7f_{ctm}$	$E_{c0}(\frac{f_{ck}}{10})^{1/3}$	$73f_{ck}^{0.18}$	
Mean GRF	$f_{cm,GRF} = 0.85f_{ck}$	$*f_{ctm,GRF} = 0.3(f_{cm,GRF})^{2/3}$	$E_{c0}(\frac{f_{cm,GRF}}{10})^{1/3}$	$73f_{cm,GRF}^{0.18}$	
Design	$f_{cd} = f_{ck}/\gamma_c$	$f_{ctd} = f_{ctk,min}/\gamma_c$	$E_{c0}(\frac{f_{cd}}{10})^{1/3}$	$73f_{cd}^{0.18}$	

*only for concrete class \leq C50

$E_{c0} = 21500$ MPa for all

Table 4.2: Summary of FEM choices for STM designed pile caps

Model Geometry	
Geometry	3-dimensional
Model	Quarter model
Support Condition	
Pile	Steel plate
E_s	800GPa
Thickness	200mm
Loading Condition	
Load Application	Displacement control
Imposed Deformation	1mm
Load Step Size	0.04mm
Material Models	
Concrete Material Model	
Material Model	Total Strain Crack
Poisson Ratio, ν	0.15
Crack Orientation	Rotating
Tension Curve	Hordijk
Tensile Strength	1.35 MPa
Tensile Fracture Energy, G_f	0.125 N/mm
Crack Band Width Specification	Rots
Poisson Ratio Reduction Model	Damage Based
Compression Curve	Parabolic
Compressive Strength, f_{cd}	20 MPa
Compressive Fracture Energy, G_c	31.29 N/mm
Reduction Model	Vecchio and Collins (1993)
Lower Bound for Reduction Curve	No reduction
Confinement Model	Selby and Veccio
Density	2500kg/m ³
Reinforcement Material Model	
Youngs Modulus	200 GPa
Plasticity Model	Von Mises Plasticity
Plastic Hardening	Plastic strain-yield stress
Hardening Hypothesis	Strain Hardening
Hardening Type	Isotropic Hardening
Type	Embedded
Yield Strength, f_{yd}	435 MPa
Ultimate strength, f_{td}	468 MPa
Mesh	
Continuum Element Type	Solid brick element
Continuum Element Name	CHX60
Reinforcement Element Type	Truss
Element Size (h)	150mm
Interpolation Scheme	Quadratic
Analysis Procedure	
Iterative Solution Procedure	Newton Raphson
Iteration per Load Step	50

Each analysis was continued until numerical failure occurred. The numerical failure was defined as:

- Concrete strain exceeding the ultimate strain, $\varepsilon_{cu} = 3.5\text{‰}$
- Reinforcement strain exceeding the ultimate strain $\varepsilon_{su} = 4.5\%$
- The convergence norm of the nonlinear calculation exceeding 10%

Seven parameters are compared from the results of the STM and numerical model which are compressive stress in the concrete particularly in the CCC-node, stress in the rebar at ULS and SLS, crack width, failure load, lever arm and force in the horizontal tie.

4.1 Feringa Building

The first project selected is the Nieuwbouw Feringa Building which was designed in 2018 and includes various types of pile caps. Two pile caps which fit the scope of this thesis were selected and modelled from this project .

a. NFB-1

Pile cap NFB-1 has dimension 2600x2600x1400mm as shown in [Figure 4.1](#). The pile diameter is $\varnothing 460\text{mm}$ while the column has a dimension of 450x450mm. The ULS and SLS load are specified as 8000 kN and 6000 kN respectively.

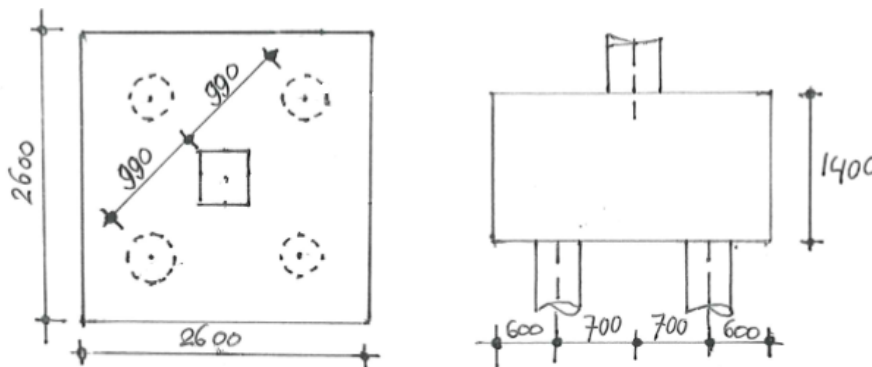


Figure 4.1: Geometry of pile cap NFB-1 [64]

The available length of the longitudinal reinforcement was found to satisfy the anchorage length rendering bending unnecessary. However, the design still provided bended re-bar as shown in the reinforcement layout in [Figure 4.2](#) to avoid re-bar slip.

b. NFB-2

Pile cap NFB-2 is mostly similar to NFB-1 except two parameters: the height which is 1000mm and distance between the edge of the pile cap and the center of the pile which is 805mm as shown in [Figure 4.3](#). Pile diameter, column dimension, reinforcement layout, ULS and SLS load remain the same.

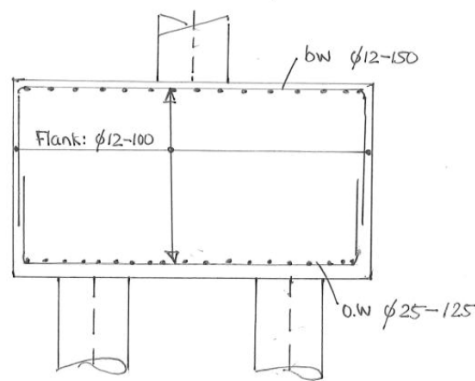


Figure 4.2: Reinforcement layout in pile cap NFB-1 [64]

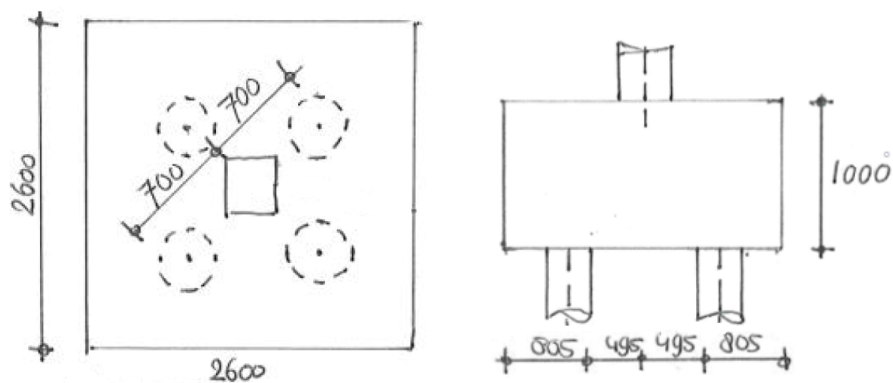


Figure 4.3: Geometry of pile cap NFB-2 [64]

4.2 Kloosterboer Vastgoed

The Kloosterboer Vastgoed project was completed in 2020 and primarily consisted of foundation design. Among the pile caps designed however, only one was four-pile pile cap and fit the scope of this thesis.

c. NK-1

Pile cap NK-1 has dimension 2000x2000x800mm as shown in Figure 4.4. The pile diameter is \varnothing 400mm while the column has a dimension of 300x300mm. Distance from the edge of the pile cap to the center of the pile is 400mm. The ULS and SLS load are 3725 kN and 2550 kN respectively.

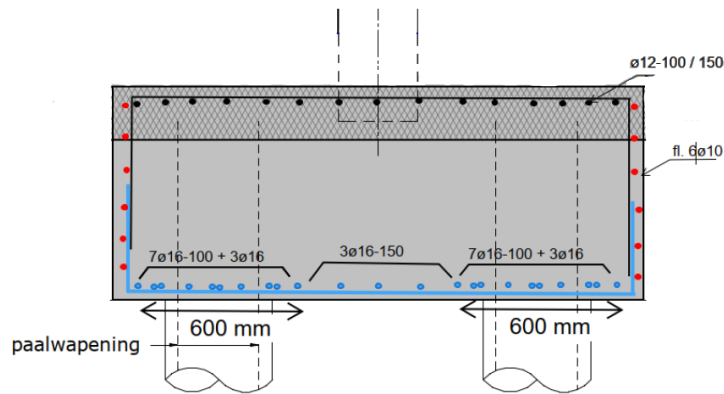


Figure 4.4: Reinforcement layout in pile cap NK-1 [65]

4.3 Comparison between Numerical Model and STM Calculation

4.3.1 Compressive Stress in Concrete

The stress in the CCC-node in the manual calculation is determined based on the concrete quality and force per pile as per NEN-EN 1992-1-1:2005 section 6.5 [5]. Moreover, the maximum allowable stress in concrete under triaxial stress state is calculated using Equation 4.1. On the other hand, in the numerical model, the maximum stress in confined concrete is calculated according to the DIANA manual [9] discussed in subsection 2.3.2. The confining pressure is set as 10MPa which was the minimum principal stress in the compression zone in all three pile caps. This would result in a conservative estimation as shown in Table 4.3. Figure 4.5 shows the position of CCC-nodes in the STM and numerical model.

$$\sigma_{RD,max} = \min(k_4 v' f_{cd}, \alpha_{cc} f_{ck,c} / \gamma_c) \quad (4.1)$$

Where, $\sigma_{RD,max}$ is the maximum allowable stress in concrete under triaxial stress state,
 k_4 is a coefficient with a value of 3.0,
 v' is defined as $1 - f_{ck}/250$,
 f_{cd} is the design strength of concrete,
 f_{ck} is the characteristic strength of concrete.

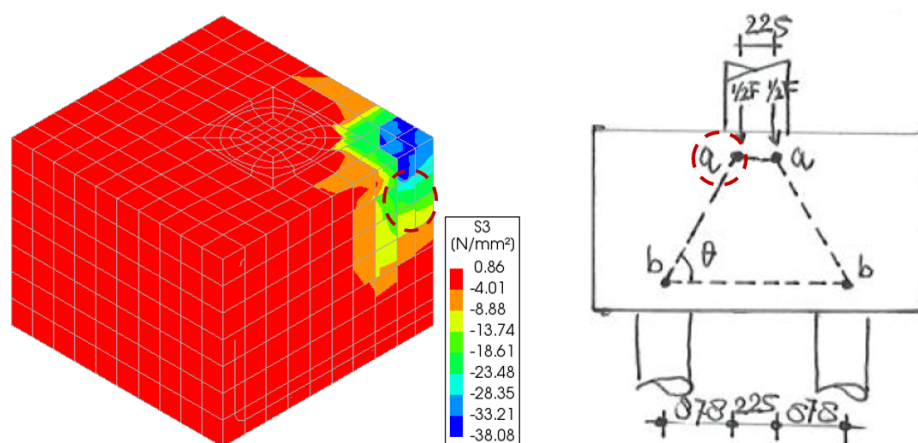


Figure 4.5: CCC-node in STM and numerical model

Table 4.3 shows comparison of compressive principal stresses, S_3 , in concrete at ULS between the numerical model and the STM calculations. It can be observed that the numerical model result in lower stresses than the STM for all pile caps. For NFB-1 and NFB-2, the stress in the model is about 60% of the STM result and around 45% of the maximum allowable value. For NK-1, it is only 23% and 19% of the STM and allowable limit respectively. It can be concluded that this is not because the numerical model reaches the maximum stress limit prematurely since the stress limit for the STM and numerical model are comparable.

Thus, this large difference in stress is because of overestimation in the STM and the stress distribution in the numerical model is more favorable. Moreover, concrete in the numerical model takes up tensile stress after initial cracking following the Hordijk curve in Figure 2.5b. The STM approach however, assumes the concrete contribution post crack to be zero. The flank reinforcement also provides confinement in the pile cap which is not taken into account in the STM calculations.

Table 4.3: Comparison between numerical and STM results for stress in concrete

Pile cap	Numerical (MPa)	Numerical Limit (MPa)	STM (MPa)	STM Limit (MPa)
NFB-1	23.5	54.1	39.5	52.8
NFB-2	25.5	54.1	39.5	52.8
NK-1	11.5	54.1	50.1	60.2

4.3.2 Internal Lever Arm

The internal lever arm in the manual calculation is determined using $z = 0.2l + 0.4h \leq 0.6l$ according to the old Dutch code (NEN 6720:1995) [46]. For the numerical model, the lever arm is calculated by determining the height of the compression zone under the column using proving curve. The vertical distance of the centroid of this region from the center of the main rebar is then calculated. Figure 4.6 shows an example of a global stress component along the height of pile cap NFB-1.

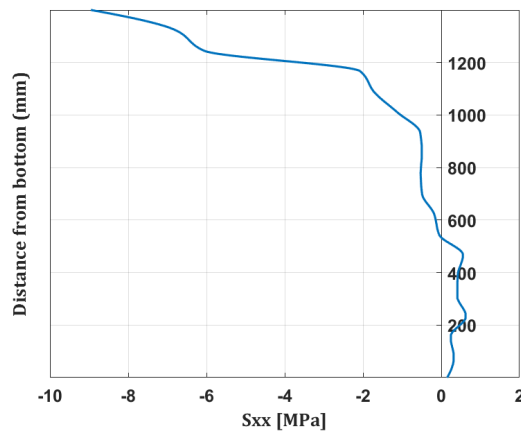


Figure 4.6: Lever arm calculation in numerical model

The stress that must be used in the lever arm calculation should be in the diagonal direction following the strut and tie configuration. So, global stress components in the x and y direction are obtained from the numerical model and their component in the diagonal direction is used to determine the stress state diagonally. The centroid is determined by dividing the compression zone into multiple regular shapes (triangle and rectangles) and calculating their respective areas and centroid. The overall centroid for the total area under the curve is then computed by multiplying each area to the respective centroid and dividing the sum to the total area.

It can be observed from [Table 4.4](#) that the lever arm in the numerical model is consistently higher than the manual calculation for all pile caps. Hence, it can be inferred that STM approach is more conservative. The length of the lever arm affects the forces in the tensile ties as it determines the angle between the compressive strut and tension tie. Thus, the higher the lever arm the lower the forces in the tie and subsequently lower stresses. The maximum lever arm value is $0.6 * l$ where l is the diagonal distance between the center of the piles at the opposite end of the pile cap. The lever arm in all the numerical models fulfil this criteria.

Table 4.4: Comparison between numerical and STM results of internal lever arm

Pile cap	Numerical (mm)	STM (mm)	Max. Value (mm)
NFB-1	1168	956	1188
NFB-2	791	680	840
NK-1	672	659	1018

4.3.3 Stress in Reinforcement at ULS

The comparison of stress in the rebar at SLS and ULS as shown in [Table 4.5](#) reveals that the numerical model for all three pile caps result in lower values than the STM calculations. In fact, it can be noted that the stress in NFB-1 recorded in the numerical model at ULS is only 70% of the STM calculation and only 43% of the maximum allowable stress. Hence, it can be inferred that the longitudinal reinforcements in these pile caps are not fully utilized.

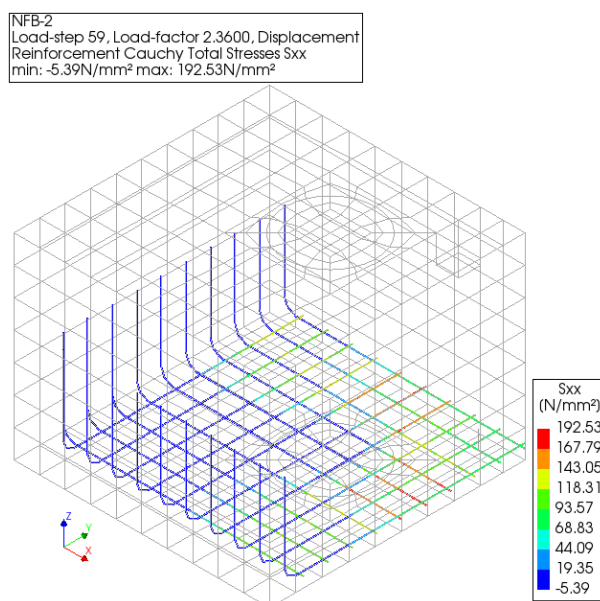


Figure 4.7: Example of stress in main reinforcement

The expected stress in the longitudinal reinforcement at ULS in the STM approach is calculated using the force carried by the tension tie. Pure tension is assumed throughout the length of the rebars for this calculation. However, the numerical model shows a variation in stress along the length. Figure 4.7 shows an example of stress in the longitudinal reinforcement. It can be observed that the stress along the length of the rebars increases from the corner towards the center. This stress distribution contributes to the lower stress in the re-bar in the numerical model. Moreover, the longer lever arm of the numerical models also contributes to this phenomenon as it leads to a larger angle between the compressive strut and tension tie which leads to lower force in the latter.

Table 4.5: Comparison between numerical and STM results of stress in rebars at ULS

Pile cap	Stress at ULS [MPa]		Load [kN]		Stress Limit [MPa]
	Numerical	STM	Numerical	STM	
NFB-1	186	265	913	1840	435
NFB-2	193	250	945	1225	435
NK-1	363	369	731	741	435

4.3.4 Crack Width and Steel Stress at SLS

The crack pattern and deflection of each pile cap at the respective peak load is closely observed to determine the failure mode. While the initial cracks occur at the bottom center of the pile cap, as the load increases a diagonal crack occurs along the symmetry face connecting the edge of the column with the opposite face of the pile cap. The width of this crack progressively increases and shows a crack pattern as shown in Figure 4.8a at failure load. The pile cap section right under the column is punched in as shown in Figure 4.8b. While all three pile caps show similar crack patterns, the main reinforcement in NK-1 have yielded at the peak load. Hence, the failure mode of pile cap NFB-1 and NFB-2 is determined to be punching shear (P) while NK-1 is flexure-induced punching (Py) in the numerical models. On the other hand, the unity checks for the STM calculations Table 4.7 shows that the critical parameter is the crack width on the pile-cap soffit.

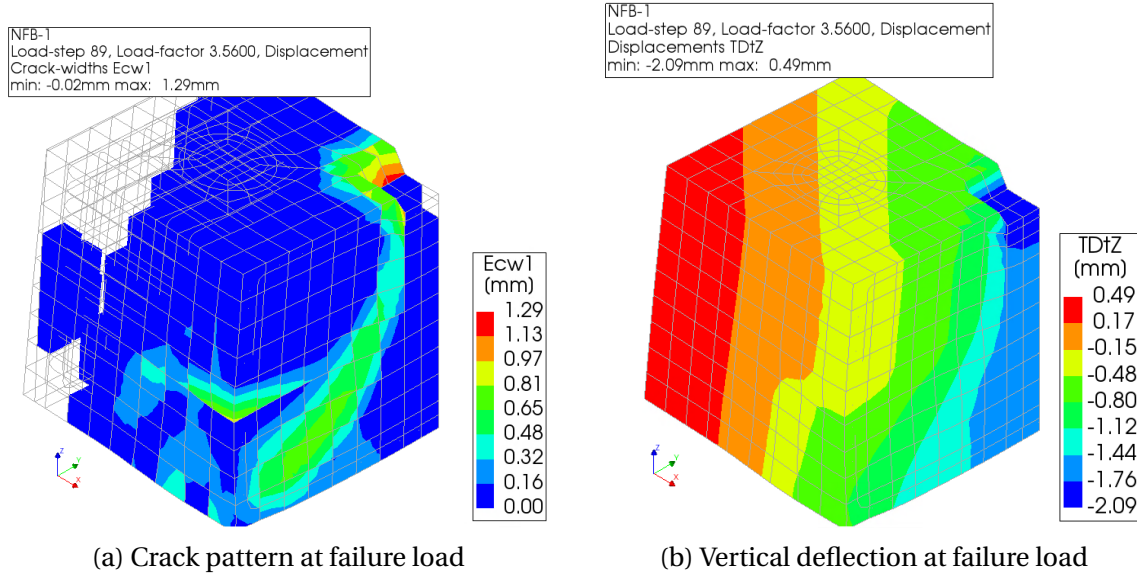


Figure 4.8: Failure mode of pile cap NFB-1 (scaled view)

Stress at SLS is calculated by scaling down the ULS stress with the ratio of the ULS and SLS load as $\sigma_{SLS} = \frac{Load_{SLS}}{Load_{ULS}} * \sigma_{ULS}$ both in the STM calculation and numerical model. Subsequently, crack width is calculated following Eurocode [59] provisions in section 7.3 using Equation 4.2 - 4.4.

$$w_k = s_{r,max}(\epsilon_{sm} - \epsilon_{cm}) \quad (4.2)$$

$$s_{r,max} = k_3 C + \frac{k_1 k_2 k_3 \phi_{staaf}}{\rho_{p,eff}} \quad (4.3)$$

$$\epsilon_{sm} - \epsilon_{cm} = \frac{\sigma_s - k_t \frac{f_{ct,eff}}{\rho_{p,eff}} (1 + \alpha_e \rho_{p,eff})}{E_s} \geq 0.6 \frac{\sigma_s}{E_s} \quad (4.4)$$

Where, w_k is the crack width,
 $s_{r,max}$ is the maximum crack spacing,
 ϵ_{sm} is the mean strain in the reinforcement,
 ϵ_{cm} is the mean strain in the concrete between cracks,
 k_n coefficients taking account of different properties such as rebar bond,
 $A_{c,eff}$ is the effective concrete area determined as $bh_{c,eff}$,
 $\rho_{p,eff}$ is the rebar ratio determined as $A_s/A_{c,eff}$,
 σ_s is the stress in the steel,
 α_e is the ratio of modulus of elasticity, E_s/E_{cm} ,
 $f_{ct,eff}$ is equal to the mean tensile strength of concrete, f_{ctm} .

Since the stress at SLS is lower in the numerical model in all pile caps, it results in a lower crack width value as shown in Table 4.6. Though the crack width is lower than the maximum allowable value in both the manual and numerical model, it can be observed that the value in the latter is significantly lower. Thus, it can be inferred that crack width is not critical in the numerical model.

Table 4.6: Comparison between numerical and STM results at SLS

Pile cap	Stress at SLS [MPa]		Crack Width [mm]		Max. Crack Width [mm]
	Numerical	STM	Numerical	STM	
NFB-1	85	199	0.13	0.41	0.43
NFB-2	83	192	0.12	0.42	0.43
NK-1	211	252	0.26	0.42	0.43

Table 4.7 shows unity checks summarizing the numerical and STM calculation of the three pile caps. It is noted that each pile cap have some capacity left in the STM design as all the unity checks are less than one. However, it can be observed that the unity checks for crack width, stress in concrete and steel in numerical models are much lower. The unity check of the lever arm is higher in the numerical model which means the longer lever arm of the numerical models leads to a larger angle between the compressive strut and tension tie which leads to lower force in the tie. This shows that the results are favorable compared to STM calculations which leaves room for optimization in the design of pile caps

Table 4.7: Unity check comparing numerical and STM

	NFB-1		NFB-2		NK-1	
	Numerical	STM	Numerical	STM	Numerical	STM
Stress in concrete	0.44	0.75	0.48	0.75	0.19	0.83
Stress in rebar	0.43	0.61	0.44	0.57	0.84	0.85
Crack width	0.29	0.98	0.29	0.77	0.99	0.99
Lever arm	0.98	0.80	0.94	0.81	0.66	0.65

5. Parametric study

The analysis in [chapter 4](#) demonstrates that FEM model results are favourable compared to STM calculations which leaves room for optimization in the design of pile caps. Hence, parametric study was conducted to identify the possibility of optimization by investigating the sensitivity of the structural response to changes in design parameters. The parameters explored in this research are pile cap geometry, reinforcement percentage (both bottom and flank reinforcement) and concrete quality. Pile cap NFB-1 was selected to conduct this study.

5.1 Pile cap geometry

The depth of the pile cap, which was originally 1.4m (pile cap A1), was reduced to 1.3m and 1.2m while maintaining the reinforcement percentage constant. While the failure mode of all pile caps remains punching shear, it can be observed from [Table 5.1](#) that the failure load shows a decline as the depth decreases. This is because one of the governing parameters for punching resistance is the height of concrete. Hence, the higher the depth, the higher the load carrying capacity.

For all specimens, the first crack is observed at the center of the pile cap soffit which propagates toward the the opposite faces along the symmetry faces. As the load increases, new cracks start to appear at the interface between the column and the pile cap. Small cracks then start to occur throughout the symmetry faces and a wide curved crack connects the edge of the column with the pile cap face along the adjacent symmetry face as shown in [Figure 5.1](#). Though the crack propagation is similar for the three specimens, crack width increases as the depth is decreased. A closer look into the cracking load reveals that the tensile strength is reached earlier and crack is initiated at a lower load in the pile cap with lower depth as expected due to lower section modulus. Hence, by the time the ULS load is reached, cracking would have significantly developed. The crack load is measured as 3709 kN, 3215 kN and 2719 kN for pile cap A1,B1 and C1 respectively.

[Table 5.1](#) also shows that reducing depth increases stress both in the reinforcement and concrete. Since cracking occurs earlier as the depth of the pile cap decreases, the bottom reinforcement is activated earlier. Hence, by the time the ULS load is reached, the stress in the re-bar will be higher.

Table 5.1: Comparison between results for pile cap of various depth

Name	Depth (m)	S_{xx} at SLS (MPa)	S_{xx} at ULS (MPa)	S_3^* at ULS (MPa)	Crack Width (mm)	Lever Arm (mm)	Failure Load (kN)
A1	1.4	85	186	23.38	0.13	1168	9237
B1	1.3	175	233	24.36	0.16	1010	9140
C1	1.2	237	316	30.01	0.23	960	8474

* Stress in CCC-node under column

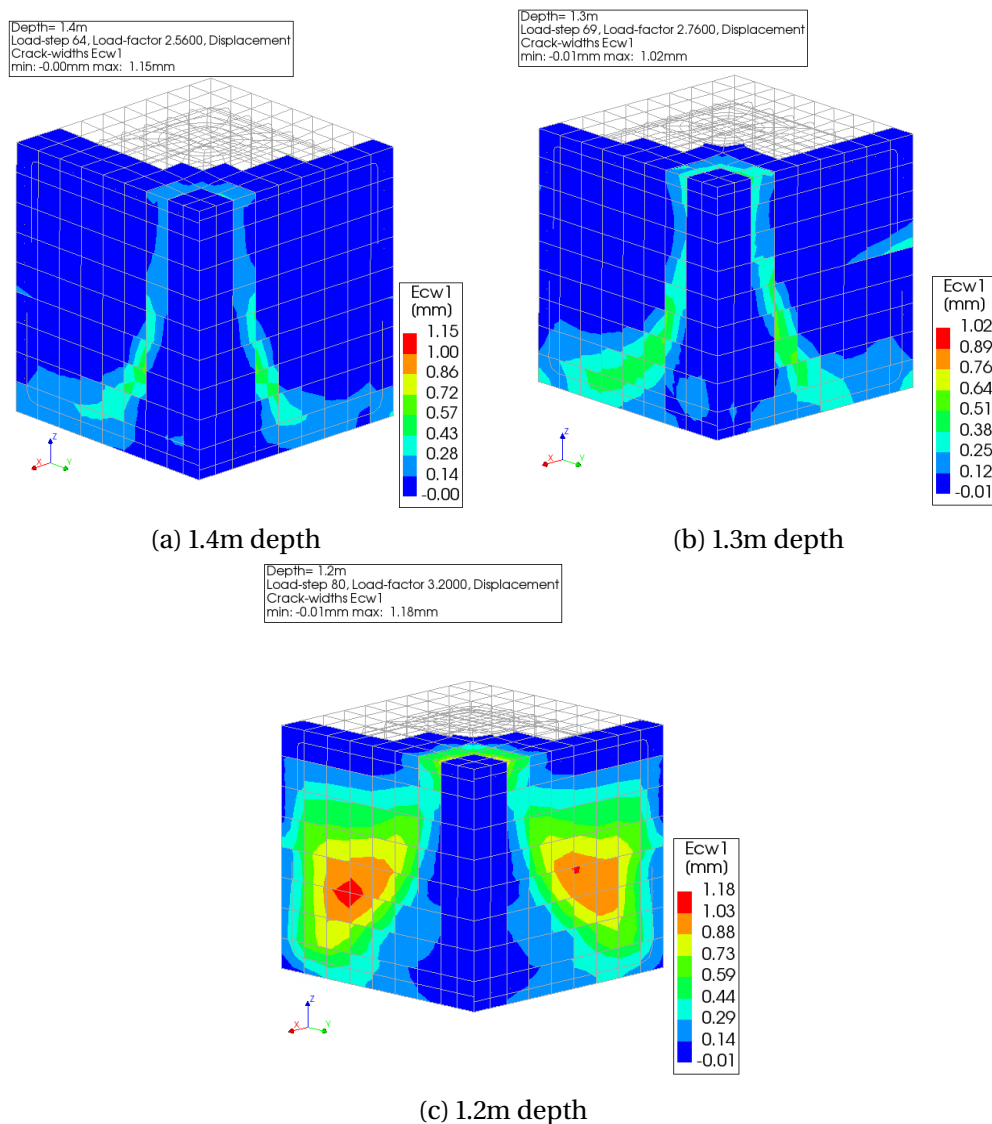


Figure 5.1: Crack pattern at ULS for pile caps with different depth

A closer look into the crack pattern of the three specimens at ULS in Figure 5.1 shows that the cracks along the symmetric faces progressively develops covering more surface on the symmetry face as the height decreases. This is simply because of the delayed cracking in the pile caps with higher depth. The crack pattern of pile cap A1 at a latter load step reveals a similar pattern as pile cap B1.

While the decrease in height is only 7.1% and 14.3% for pile cap B1 and C1 respectively, the stress in the reinforcement has increased by 25% and 70% compared with the control specimen. The compressive stress in the CCC-node has increased by 4.3% and 28.4% respectively and the crack width has shown a 25% and 82.7% increase. However, the crack width of all specimens is under the maximum crack width limit which is 0.429mm. Though the peak load has shown a 1.1% and 8.3% decrease for specimen B1 and C1, both have a load carrying capacity that exceeds the original design load of 8000 kN. Thus, it can be observed that C1 is still a safe design despite its lower depth.

To evaluate the monetary advantage of geometry optimization in pile caps, the cost of each specimen was calculated as shown in Appendix D. The cost of pile cap A1, B1 and C1 is calculated as €2848 , €2690 and €2514 . Thus, for every 0.1 meter reduction in depth, there is a 6%

reduction in cost per pile cap. This can have a substantial effect on the overall cost of a project since buildings have a lot of pile caps.

In addition to cost reduction, optimizing the pile cap depth has a significant impact on the environment as lower depth in the pile cap means lower volume of concrete. Production of concrete and its ingredients require energy that result in generation of CO₂. According to the National Ready Mixed Concrete Association, concrete uses about 7% - 15% cement by weight depending on the performance requirement and the average quantity of cement is around 250 kg/m³. As a result, one cubic meter of concrete has a CO₂ footprint of 100 - 300 kg or approximately 5% - 13% of the weight of concrete produced depending on the mix design [66]. Thus, a 0.1m reduction in depth in this pile cap translates to a 0.676 m³ reduction in volume which lowers the CO₂ footprint by 67.6 - 202.8 kg. This means specimen C1 has 135.2 - 405.6 kg lower CO₂ footprint as compared to A1.

5.2 Bottom reinforcement percentage

The bottom reinforcement percentage in the original pile cap was 2.62%. Three different variations were modelled with 2.36%, 2.09% and 1.83% while maintaining all other parameters constant. It can be observed from Table 5.2 that decreasing the rebar percentage results in higher stress in the reinforcement. This is because the total force in the reinforcement remains relatively similar since the lever arm doesn't change significantly. The load in the tension tie is calculated as 913kN, 931kN, 892kN and 911kN in A1, B2, C2 and D2 respectively. Since the total area of the reinforcement has decreased, the stress in the rebars subsequently increases. The crack width increases as the rebar percentage decreases following the higher stress in SLS.

Table 5.2: Comparison between results for pile cap of various reinforcement percentage

Name	Rebar %	S_{xx} at SLS (MPa)	S_{xx} at ULS (MPa)	S_3^* at ULS (MPa)	Crack Width (mm)	Lever Arm (mm)	Failure Load (kN)
A1	2.62	85	186	23.38	0.13	1168	9237
B2	2.36	96	211	22.59	0.15	1260	9200
C2	2.09	104	227	23.19	0.18	1243	8696
D2	1.83	121	265	23.87	0.23	1241	8680

* Stress in CCC-node under column

On the other hand, the compressive stress in concrete does not show a significant change as the rebar percentage decreases. As the force in the rebars doesn't show a significant difference, the balancing compressive force in the concrete in the CCC-node also doesn't change drastically. The failure load reduces from A1 to D2. An interesting observation in this parametric study is that although the failure mode remains punching the crack pattern changes as the percentage decreases. Figure 5.2 shows that the predominant crack in the original pile cap, A1 (2.62%), begins under the column and propagates along the symmetry faces towards the bottom face with a curved shape. Although the pile cap soffit is cracked, the crack width is relatively smaller than the major crack. Pile cap D2 (1.83%) also exhibits wide cracks in the interface between the column and pile cap. However, the propagation towards the soffit follows a straight line rather than curved. These connect the predominant crack at the bottom of the pile cap tracing the corner of the pile. Moreover, two distinct vertical bending cracks are observed on the outer face of the pile cap. Despite the slight difference in crack pattern however, the failure mode remains punching for all specimens.

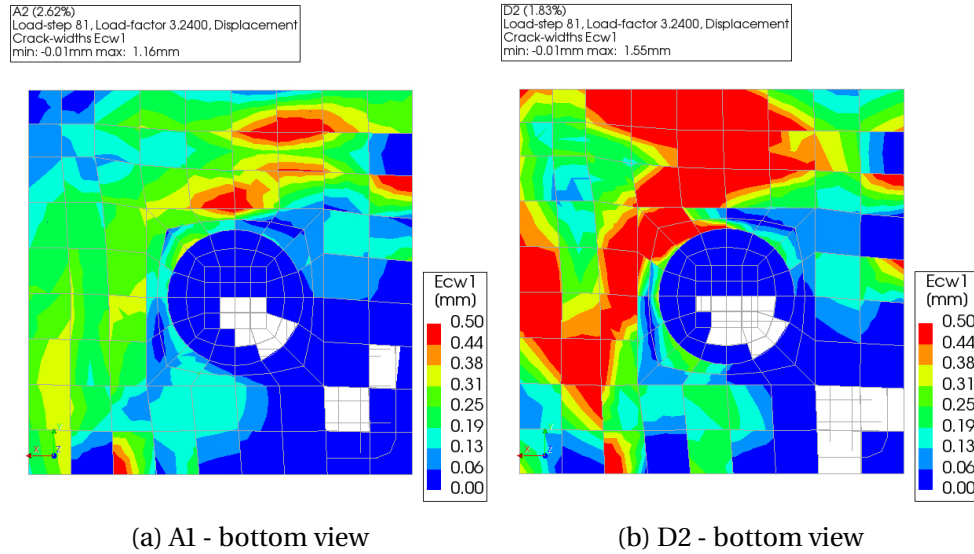


Figure 5.2: Crack pattern at failure for pile caps with different rebar percentage

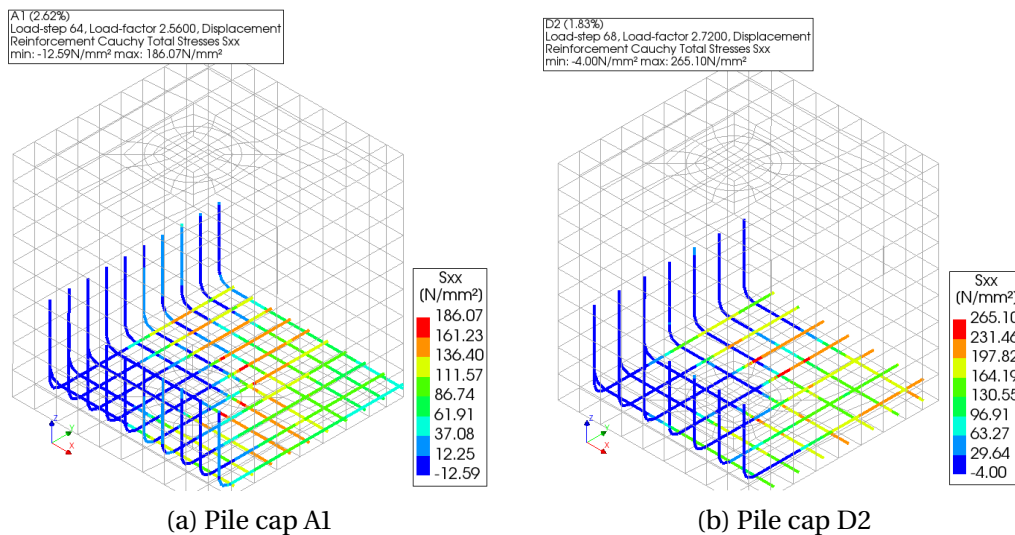


Figure 5.3: Stress in main rebar at ULS for pile caps with different rebar percentage

The cost effect of rebar percentage optimization has also been explored as shown in Appendix D. The total cost of pile cap A1, B2, C2 and D2 are €2848, €2829, €2790 and €2752 respectively. This is translated as a 0.21% reduction in cost per 1m reduction in rebar length or 0.05% reduction in cost per 1kg reduction in rebar weight. This is far lesser than the cost reduction obtained by optimizing the pile cap geometry.

The process emission associated to the production of reinforcement bars is 2.8 kg CO₂/kg. Although the degree of recycling of rebars is high, 90-100%, it still results in a footprint of 0.43 kg CO₂/kg [67]. A rough estimation of the CO₂ footprint in specimen D2 as compared to A2 shows a 183 kg reduction which is lower than the CO₂ reduction obtained by lowering the depth in specimen C1.

5.3 Number of flank reinforcement

Flank reinforcement provide confinement and prevent bulging out of concrete when crack initiates. Hence, it is expected to contribute to the capacity of pile caps. The original pile cap had 12 flank reinforcements. Three alterations were subsequently designed with 8, 4 and 0 flanks to compare their effects on the behaviour of the pile cap.

Figure 5.4 shows that the lower the number of flanks, the higher the stress in the available flanks. Moreover, Table 5.3 demonstrates that lowering the number of flank rebars increases the stress in the longitudinal reinforcement while slightly increasing the stress in concrete. There is a 46% difference in the stress in the rebar between the original pile cap and D4 (no flank). This shows that the flank reinforcements play an important role in reducing the stress in the longitudinal rebars.

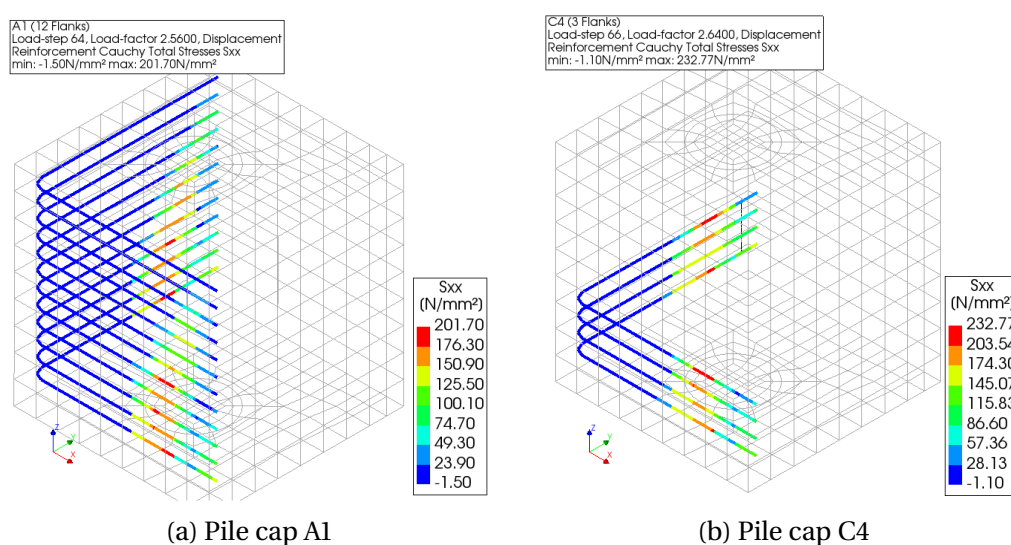


Figure 5.4: Stress in flank rebar at ULS for pile caps with different number of flanks

Although the failure load decreases from A1 to D3, the difference between the two pile caps is only 1.3%. Thus, it can be inferred that load carrying capacity is not significantly affected by flank reinforcement. Furthermore, while the crack width increases, the failure mode remains punching for all pile caps. The change in crack pattern shows a similar trend as decreasing pile cap depth where the cracks along the symmetry face become wider as the number of flank rebars decreases. This is because the confinement provided by the flank rebars decreases which results in the concrete bulging out and subsequently resulting in more cracking.

Table 5.3: Comparison between results for pile cap of various number of flank re-bars

Name	Flank No.	S_{xx} at SLS (MPa)	S_{xx} at ULS (MPa)	S_3^* at ULS (MPa)	Crack Width (mm)	Lever Arm (mm)	Failure Load (kN)
A1	12	85	186	23.38	0.13	1168	9237
B3	8	86	188	23.32	0.13	1148	9217
C3	4	106	233	23.72	0.16	1146	9166
D3	0	124	272	24.71	0.18	1143	9114

* Stress in CCC-node under column

5.4 Concrete quality

The compressive strength in the original pile cap was 30MPa. Three pile caps with 40MPa, 35MPa and 25MPa were then designed to evaluate the effect of concrete quality. As the compressive strength increases, the lever arm decreases and load carrying capacity is improved as expected.

Figure 5.5 shows the load deflection diagram of the four specimens. It can be observed that as the the failure load decreases as the compressive strength decreases. This lower capacity can be attributed to lower tensile strength.

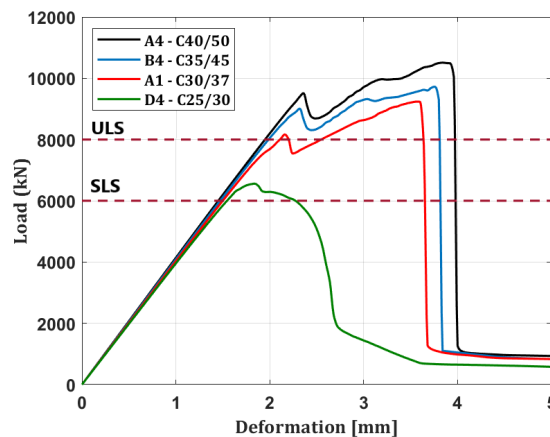


Figure 5.5: Load-deflection graph of pile caps with various concrete quality

Table 5.4 shows that as concrete quality increases, the stress in the rebar decreases significantly at ULS. This is because the failure load shows a substantial (14%) increase as the concrete quality is changed from 30 to 40MPa. Thus, at ULS load (8000 kN), cracks have not fully developed yet in pile cap A4 and B4 to activate the rebars.

Table 5.4: Comparison between results for pile cap of various concrete quality

Name	$f_{ck}/f_{ck,cube}$ (MPa)	S_{xx} at SLS (MPa)	S_{xx} at ULS (MPa)	S_3^* at ULS (MPa)	Crack Width (mm)	Lever Arm (mm)	Failure Load (kN)
A4	40/50	15	33	21	0.02	1271	10509
B4	35/45	17	38	21.00	0.03	1266	9473
A1	30/37	85	186	23.38	0.13	1168	9237
D4	25/30	-	-	-	-	-	6558

* Stress in CCC-node under column

A closer look at the crack pattern reveals that the failure mode changes from corner shear to punching shear failure as the concrete quality decreases from 40MPa to 30MPa. Figure 5.6 compares the cracks on the side and bottom faces of pile cap A4 and A1. The crack pattern and failure mode of A1 is discussed in section 5.2. In pile cap A4, wide cracks appear along the symmetry faces uniformly. Moreover, wide crack occur along the corner of the pile which is the hall mark of corner shear failure.

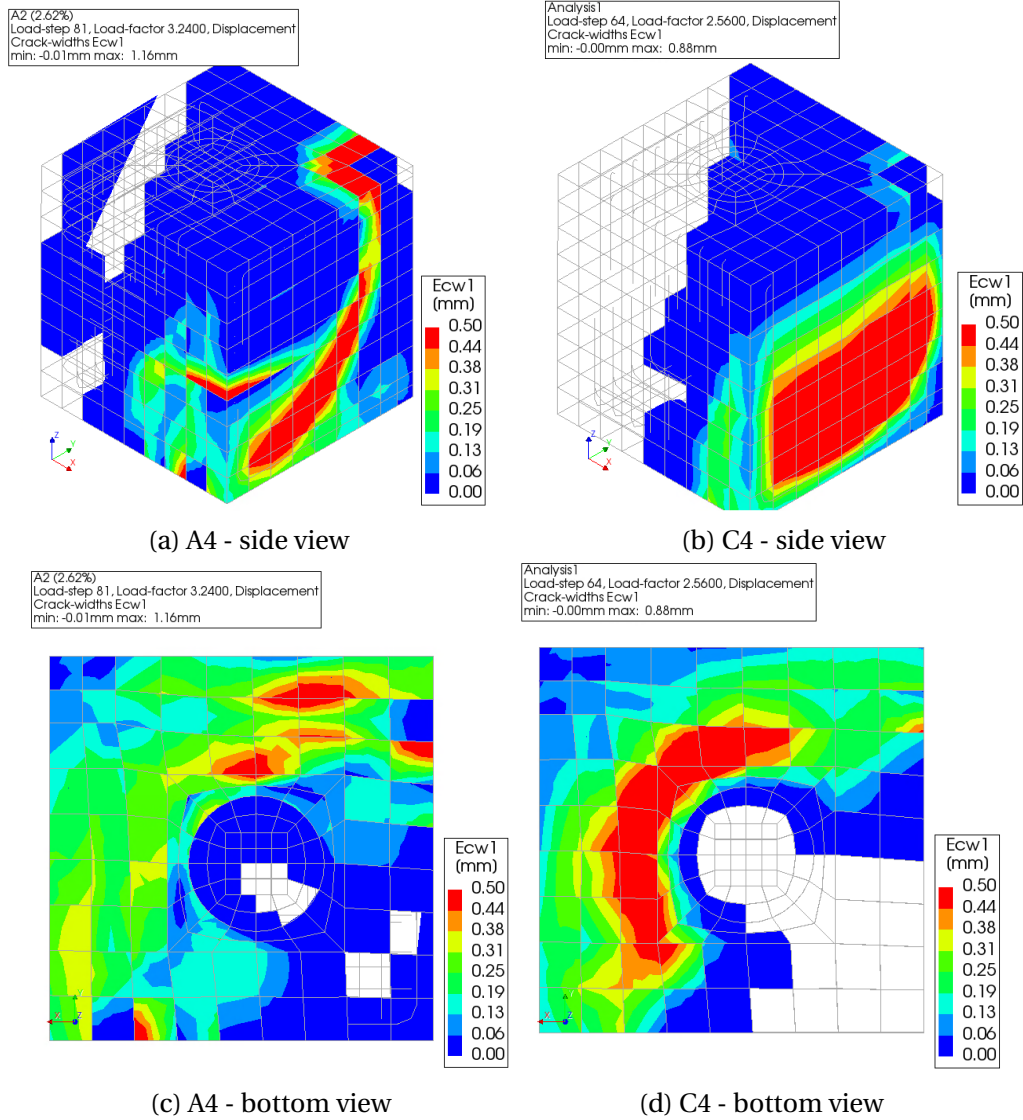


Figure 5.6: Crack pattern at ULS for pile caps with different concrete quality

6. Proposal for experimental research

6.1 Purpose of experimental study

The purpose of the experimental research is to validate the key findings of this thesis. This can be summarized into two key questions:

1. Can punching failure be accurately predicted by FEM?
 - The comparison between the experiment and numerical models in [chapter 3](#) includes four out of the five pile cap failure modes. Pile caps with punching shear failure modes have not been included due to lack of experimental data. So this must be investigated by comparing experimental data to the numerical model and STM calculation.
2. Can the optimization observed in the numerical models also be achieved in reality?
 - The parametric study in [chapter 5](#) shows that reducing certain parameters of a pile cap can still result in a safe design. Safe design means the failure load is greater than the design load and all unity checks are less than 1. As this is a key finding of this thesis, it must be corroborated by experiments. Hence, the effect of the four parameters explored in this thesis which are pile cap geometry, bottom reinforcement percentage, number of flanks and concrete quality must be investigated.

6.2 Experimental specimens

6.2.1 Experiment Set 1

To investigate the first question, a scaled down version of pile cap NFB-1 has been selected as it is expected to have punching failure based on numerical simulation. Since conducting the experiment on a full-scale pile cap will be expensive and impractical due to limited facilities, a scaled down specimen shall be used. The original pile cap has a dimension of 2.6m x 2.6m x 1.4m which was scaled down by a factor of 1/3 to 0.9m x 0.9m x 0.5m. This scale is determined by taking the weight of the specimen and expected load carrying capacity into account as the former determines the required lifting equipment and the latter determines the loading machine.

The span-to-depth ratio and reinforcement percentage (bottom, flank and top rebar) are kept similar to the original pile cap to obtain punching failure. The concrete quality (C30/37) and reinforcement class (B500) were unchanged. The detailed properties of this specimen are shown in [Figure 6.1](#). The test shall be repeated on three specimens to obtain reliable results and limit the variability of brittle failure in experiment.

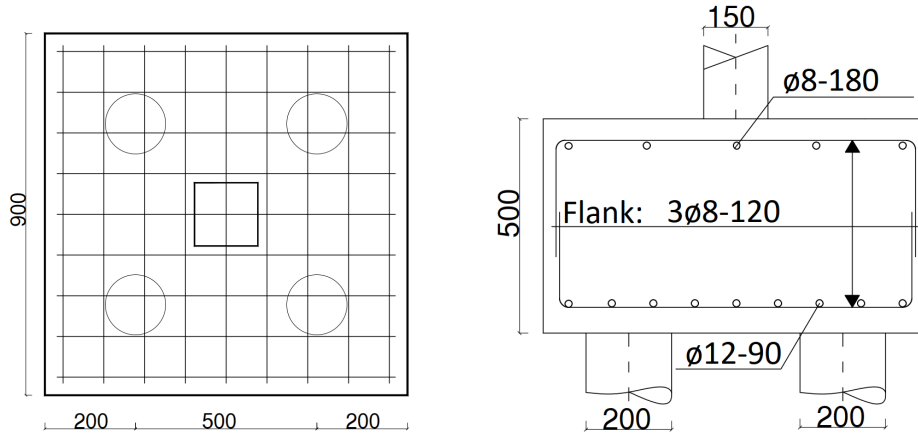
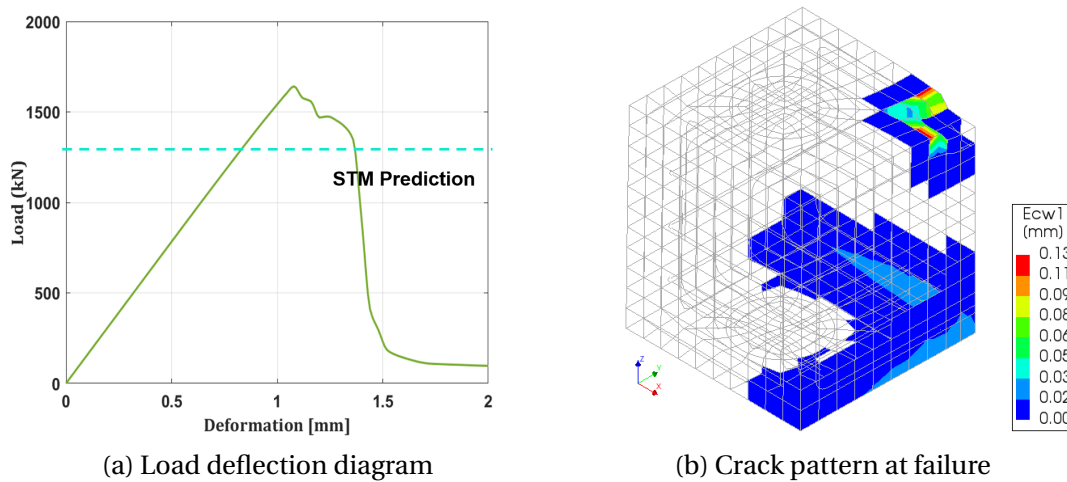


Figure 6.1: Geometry of scaled NFB-1

A numerical model of this specimen has been developed to show the expected failure mode and load capacity and the results are shown in Figure 6.2. The model was developed using the numerical choices discussed in Table 4.2 with mean values of material properties. The failure load is observed to be 1640 kN. Moreover, the pile cap fails in punching shear as the crack pattern and deformation under the column resemble the full scale NFB-1. The concrete under the column is punched through at failure as shown in Figure 6.2b.



(a) Load deflection diagram

(b) Crack pattern at failure

Figure 6.2: Expected failure mode and load capacity of scaled NFB-1

Moreover, the Wassenar excel sheet was used to predict the failure load using the STM. Similar to the numerical model, mean material properties were used and material and load factors were not considered to make the results comparable with the experiment. While the usual STM approach is to find a safe design for specific ULS and SLS loads, the reverse approach is used to determine the load carrying capacity of the pile cap. Once the predetermined geometry and reinforcement details were defined, the load that resulted in a safe design was calculated with iteration. Safe design was defined as the load at which all the unity checks are less than 1.

Hence, for the scaled NFB-1, the failure load is determined to be 1320 kN which is denoted as STM prediction in Figure 6.2a. The corresponding unity checks at this load are shown in Table 6.1. It can be observed that the anchorage length is the most critical parameter. This means the depth of the pile cap is not enough to provide sufficient anchorage length. Thus, failure would occur due to slip (debonding) if the applied load exceeds 1320 kN.

Table 6.1: Unity check of scaled NFB-1 at calculated failure load using STM

Unity Check	
Crack Width	0.49
Tension in the Tie	0.49
Compression in CCC node	0.91
Compression in CTT node	0.65
Anchorage length	0.98

This preliminary calculation already shows that the numerical result is more favorable than the STM. However, the experiment is expected to result in lower failure load than the numerical model. This is because FEM is observed to overestimate the load capacity of pile caps that have brittle failure as discussed in subsection 3.3.2. On the other hand, the STM results are expected to be lower than that of the experiment. Therefore, the experiment capacity would be between 1320 and 1640 kN.

6.2.2 Experiment Set 2

To answer the second question, the scaled NFB-1 and 4P-N-C3 from subsection 3.3.2 have been selected as representative samples as they have brittle and ductile failure respectively. For the scaled NFB-1, the results of experiment set 1 shall be used as reference.

The geometry of pile cap 4P-N-C3 is shown in Figure 3.25. The experimental results of this pile cap are already obtained by Lucia et al [58] and specified in Appendix B. The load deflection diagram is shown in Figure 6.3 and the failure mode is determined as flexure. The initial cracks are observed to appear on the lateral faces and propagate through the base towards the pile cap center. An increase in resistance and ductility is observed post yielding of main reinforcement (P_{yB}) as the load is taken up by the shear reinforcement. Once the the shear reinforcement yields (P_{yV}), failure ultimately occurs when the reinforcement ruptures.

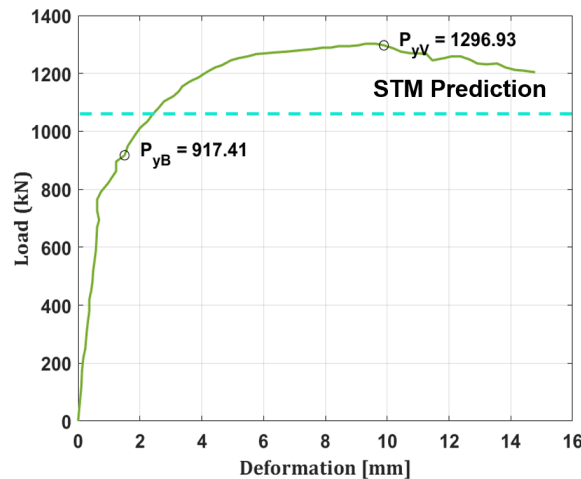


Figure 6.3: Expected experimental load deflection diagram of 4P-N-C3

As this experiment set investigates optimization of different parameters in pile caps, each parameter shall have 2 specimens. These experimental variants are similar to those studied in chapter 5: geometry, bottom reinforcement percentage, number of flanks and concrete quality. The brief properties of all specimens is shown in Table 6.2. The detailed properties and overview of experiment sets 1 and 2 are presented in Table 6.3 and Table 6.4

The names of each specimen describe its respective characteristic. The first letter denotes the failure mode - Punching (P) or Flexure (F) while the second letter denotes the altered parameter - Geometry (G), re-bar percentage (R), number of flanks (F) or concrete quality (C). The last character denotes the specimen number - one or two.

Table 6.2: Variable parameters in Experiment Set 2

Altered Parameter	Pile cap	Value	Pile cap	Value
Depth	NFB-1 (Original)	0.5m	4P-N-C3 (Original)	0.45m
	P-G-1	0.4m	F-G-1	0.40m
	P-G-2	0.3m	F-G-2	0.35m
Rebar percentage	NFB-1 (Original)	0.14%	4P-N-C3 (Original)	0.06%
	P-R-1	0.12%	F-R-1	0.04%
	P-R-2	0.11%	F-R-2	0.03%
Number of Flank	NFB-1 (Original)	4	4P-N-C3 (Original)	5
	P-F-1	2	F-F-1	2
	P-F-2	0	F-F-2	0
Concrete quality	NFB-1 (Original)	C30/37	4P-N-C3 (Original)	C30/37
	P-C-1	C25/30	F-C-1	C25/30
	P-C-2	C35/45	F-C-2	C35/45

The depth reduction per specimen is 0.1m for NFB-1 and 0.05m for 4P-N-C3. The variation in the rebar percentage is concurrent to the parametric study in [chapter 5](#) as the number and diameter of the bottom reinforcement is reduced. The number of flank have been reduced in a way that the last specimen will have no flanks to make a direct comparison between pile caps with and without flanks. Furthermore, the concrete grade has been increased to C35/45 and decreased to C25/30.

STM calculations and numerical models must be developed for all specimens similar to the original scaled down NFB-1 discussed in [subsection 6.2.1](#) to make comparisons between the experimental, analytical and numerical results.

Table 6.3: Experiment set 1 and 2 overview (1/2)

Pile cap	Geometry			Bottom Rebar		Flank Rebar		Top Rebar		Concrete quality
	Dimension	Cover, c_{nom}	w/d	Quantity	Percentage	Quantity	Percentage	Quantity	Percentage	
EXPERIMENT SET 1										
NFB-1 (Full Scale)	2600x2600x1400	0.065m	1.95	19 \varnothing 25 @125	0.14%	12 \varnothing 12 @100	0.04%	15 \varnothing 12 @150	0.03%	C30/37
NFB-1 (Scale Down)	900x900x500	0.056m		9 \varnothing 12 @90		4 \varnothing 8 @120		5 \varnothing 8 @180		
EXPERIMENT SET 2										
<i>Geometry</i>										
P-G-1	900x900x400	0.056m	2.52	Same as original [NFB-1 Scale Down]						
P-G-2	900x900x300	0.056m	3.55							
<i>Rebar percentage</i>										
P-R-1	Same as original [NFB-1 Scale Down]			8 \varnothing 12 @100	0.12%	Same as original [NFB-1 Scale Down]				
P-R-2				7 \varnothing 12 @120	0.11%					
<i>Flank rebar</i>										
P-F-1	Same as original [NFB-1 Scale Down]					2 \varnothing 8 @120	0.02%	Same as original [NFB-1 Scale Down]		
P-F-2						-	-			
<i>Concrete quality</i>										
P-C-1	Same as original [NFB-1 Scale Down]									C25/30
P-C-2										C35/45

Table 6.4: Experiment set 1 and 2 overview (2/2)

Pile cap	Geometry			Bottom Rebar			Shear Rebar, A_{sv}		Concrete quality
	Dimension	Cover, c_{nom}	w/d	A_{sb} Quantity	A_{sh} Quantity	Percentage	Quantity	Percentage	
EXPERIMENT SET 2									
4P-N-C3 (Original)	1150x1150x450	0.05m	2.88	4 ϕ 10 + 2 ϕ 12	5 ϕ 8	0.06%	5 ϕ 8	0.05%	C30/37
<i>Geometry</i>									
F-G-1	1150X1150X400	0.05m	3.29	Same as original [4P-N-C3]					
F-G-2	1150X1150X350	0.05m	3.83						
<i>Rebar percentage</i>									
F-R-1	Same as original [4P-N-C3]			4 ϕ 10	5 ϕ 8	0.04%	Same as original [4P-N-C3]		
F-R-2				4 ϕ 8	4 ϕ 8	0.03%			
<i>Shear rebar</i>									
F-F-1	Same as original [4P-N-C3]						2 ϕ 8	0.02%	Same as original
F-F-2							-	-	
<i>Concrete quality</i>									
F-C-1	Same as original [4P-N-C3]								C25/30
F-C-2									C35/45

6.3 Preliminary study

6.3.1 Mix Design and Initial Tests

The specified environmental class of all pile caps is XC2. The maximum permissible water-to-cement ratio for this class is 0.6 according to NEN-EN 206:2014 [68]. However, the exact w/c ratio will depend on the water absorption of the coarse and light aggregate as well as the type of cement used. The cement used must be one of the recommended ones in section D.2.1(2) of NEN-EN 206:2014 [68]. Moreover, the minimum required cement content is 280 kg/m^3 for C25/30 and C30/37. The measuring equipment must meet the specifications of section 9.6.2.2 of the standard and must have an accuracy of $\pm 2\%$. Measurements of each material must be done according to NEN-EN 45501 [69]. Slump test shall be conducted on the concrete mixture to check the consistency of concrete according to NEN-EN 12350-2 [70].

While these specifications are mentioned here as guidelines, the specific mix design shall be developed by the concrete plant and the mix shall be delivered by truck mixer. The total required volume of concrete for Experiment set 1 and 2 is nearly 100 m^3 out of which 10 m^3 has a grade of C25/30, 10 m^3 has a grade of 35/45 and the remaining 80 m^3 has a grade of C30/37. This includes both pile cap specimens and cubic samples.

Once the concrete mixture is obtained, six control cube specimens with dimension 150mm must be extracted from each pile cap mix according to NEN-EN 12350-1 [70]. These will be used to determine the properties of concrete at 28 days. The samples must be cured for 24 hours and then stored under the same conditions as the real size pile caps until test is done.

Cubic compressive strength, f_{cu} , shall be determined using compression test according to NEN-EN 12390-3 [71] on three of the specimens. The test result must be derived from the average of the results. The compressive strength of each specimen must meet the criteria $f_{ci} \geq (f_{ck} - 4) \text{ N/mm}^2$. Moreover, the average strength of the group sample should also fulfil $f_{cm} \geq (f_{ck} + 1) \text{ N/mm}^2$ [68].

Splitting tensile strength test shall be performed on the remaining three specimens to determine the tensile strength of the concrete and result measurements must be carried out according to NEN-EN 12390-6 [71]. The individual and average results must conform to the following criteria $f_{cti} \geq (f_{ctk} - 0.5) \text{ N/mm}^2$ and $f_{ctm} \geq (f_{ctk} + 0.5) \text{ N/mm}^2$ respectively [68].

Ribbed reinforcement bars of grade B500 must be used for all experiments. Tensile test must be performed on the reinforcing bars following NEN-EN 10080:2005 [72]. The yielding and ultimate stress and their corresponding strains must be measured and recorded.

6.3.2 Experimental Set-up

A. Loading

The four piles and column shall be simulated with loading plates with the respective dimensions. Spherical support and two-stage roller shall be positioned under each pile to set the rotation and horizontal translation free respectively. This ensures the results would not be affected by unexpected resistance due to horizontal and rotational restraint.

Loading shall be applied centrally on the column via a hydraulic piston with a capacity of 3000 kN. Each specimen shall be loaded up to failure at a constant deformation rate with pauses at regular intervals to measure crack width and crack pattern. However, including two or three cycles of loading and unloading in combination with acoustic emission measurements might provide a better understanding of the behaviour of pile caps.

B. Vertical displacement and strain

The vertical displacement shall be measured using Linear Variable Data Transformer (LVDT). LVDT is electro-mechanical transducer that measures linear displacement by converting the rectilinear motion of an object into a corresponding electrical signal. It is easy to mount and extremely robust with low risk of damage. It also has strong and stable sensors with long life-time. It's single axis sensitivity also prevent effects of other axes not to be recorded or affect the results on the axis of interest. LVDT shall be used to measure the vertical deformation of the pile cap soffit (at mid-span) and the side of the pile cap. Moreover, a minimum of 17 LDVT (5 on the bottom and 12 on the four faces), each with measurement ranges of $\pm 20\text{mm}$, shall be placed on the pile cap as shown in shown in Figure 6.4d and Figure 6.4b. The first letter signifies the where the LDVT is placed - the pile cap (P). The second letter indicates the specific location of each LDVT - on the bottom (B) or the face (F) of the pile cap. The last character denotes the number of the LDVT.

The strains of the bottom reinforcement shall be measured using strain embedded gauges. A minimum of 20 strain gauges are recommended to record the strains along the length of the reinforcement verses load. The designated nomenclature indicates the position of each strain gauge. The first letter signifies where the gauge is placed - on the reinforcement (R) or the strut (S). The second letter indicates the specific location of the gauge - in the x-direction (X) or y-direction (Y) on the reinforcement. The last character denotes the number of the strain gauge. The placement of strain gauges is shown in Figure 6.4a and Figure 6.4c.

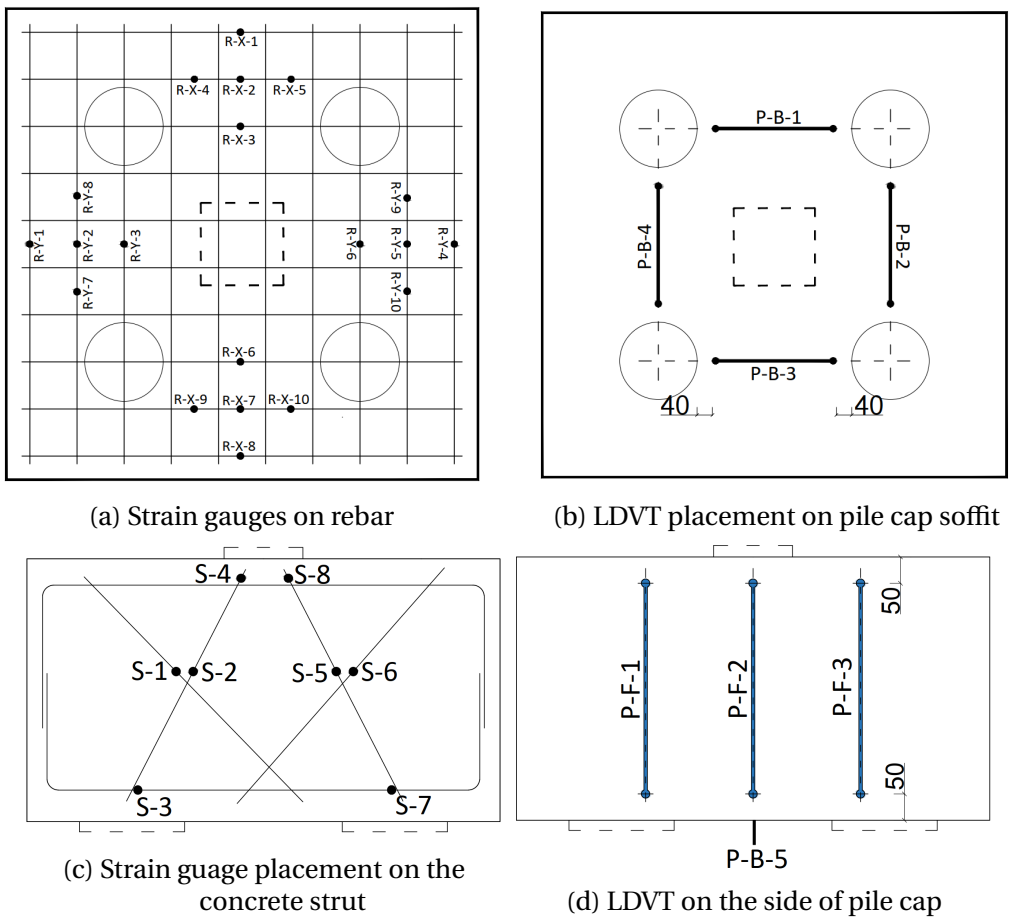


Figure 6.4: Placement of LDVTs and Strain Gauges

Reinforcement bar of $\varnothing 8\text{mm}$ shall be placed along and perpendicular to the compression strut

as shown in [Figure 6.4c](#). These rebars shall be tied to the top and bottom reinforcement and only serve to place strain gauge which measure compression and tensile strains in the region. This approach of measuring strains in the strut was used by Miguel et al [73] on three-pile pile caps and the presence of these rebars is proven not to affect the structural behaviour of the pile cap or the experimental results. Therefore, S-1 and S-5 will measure the tensile strain in the compression strut. S-2 and S-6 will measure the compression strain in the strut while S-3 and S-7 will measure the strain in the lower nodal zone (CTT node). S-4 and S-8 will measure the strains in the upper nodal zone (CCC node). Measurements of the compressive strains and nodal zones were not conducted in any of the experiments investigated in [subsection 2.5.2](#). Thus, this will be one of the added values of these proposed experiments.

Alternatively optical strain sensors can also be used to measure strain as they provide more accurate results. Optical strain sensors do not need electricity for operation and are therefore immune to electromagnetic interference. However, they are very delicate, highly sensitive to temperature and cannot be reused. Thus, a temperature sensor must be installed to allow for mathematical compensation to compare the data and subtract the temperature effects.

C. Crack pattern and width

In addition to the strain in the strut and nodes, another consistently missing data in all experiments explored in [subsection 2.5.2](#) was the crack width. While these experiment have studied the cracking pattern to understand the failure mechanism, the cracking width was not recorded which meant a comparison between the numerical model and STM calculation was not possible. Hence, an added value of these proposed experiments will be a recorded crack width data.

Visual inspections shall be performed to take measurements of the crack width and study the crack pattern. Loading shall be paused regularly and the crack width shall be measured using crack width card and visible cracks shall be indicated with markers. These measurement shall be taken for every 30kN for pile cap 4P-N-C3 and 100kN for NFB-1. These load spans are determined by taking the expected loading capacity into account.

Optionally, Digital Image Correlation (DIC) can also be used to study the crack pattern and maximum crack-width of the pile caps. This can be done by removing the LDVT on two adjacent faces, painting them white and covering them with a number of black spots. Once loading commences, three images of these sides shall be captured for every 20kN load applied.

Once the experiment is completed, the images can be post-processed using the GOM correlate software to study the crack pattern and crack widths. GOM Correlate software is based on the parametric concept that ensures all the process stages are traceable. In this software, parameters such as measurement series, calibration parameters and surface components are initialized by the user [74]. The results from the GOM software shall then be compared to the measurements from the visual inspection and LVDT deformations and validated.

D. Summary of required materials

The necessary equipment for these experiments are,

- Hydraulic jack with a capacity of 3000 kN
- Strain gauges and Linear Variable Data Transformers
- Crack width card and crack magnifier
- Loading plates, concrete mixer, molds for test samples
- Compression testing machine and splitting tensile devise

- Universal electro-mechanical machine for tensile test on rebar
- Digital Image Correlation (DIC) [*Optional*]

E. Measurements to be taken

The applied load and corresponding deflection shall be recorded to obtain the load deflection diagram. Central deflection at the bottom pile surface shall be recorded using LDVT P-B-5. The load at which the crack is initiated and the peak load shall also be measured. Measured strain from each gauge and LDVT shall also be recorded. Table 6.5 shows a summary of parameters that will be measured per pile cap. The crack pattern of each pile cap shall also be drawn on the soffit and the four faces on a projected plane such as Figure 6.5a. For each step that the loading is paused, the visible cracks shall be drawn to study the crack propagation and obtain the crack pattern as shown in the example in Figure 6.5b.

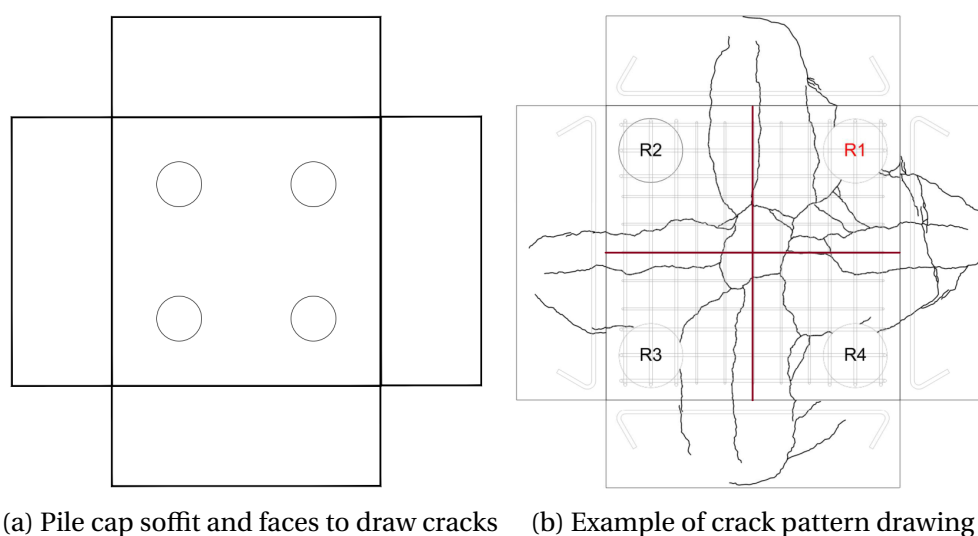


Figure 6.5: Schematic representation of crack pattern to be drawn

The results from the experiment shall then be compared with the numerical models and STM calculations. The material properties used in both shall be mean values to obtain comparable results with the experiment. The calculated capacity of the scale-down NFB-1 and the original 4P-N-C3 pile cap using STM is shown to be 1640 kN and 1060 kN respectively. On the other hand, the FEM models predict a nearly 1640 kN loading capacity for the former and 1350 kN for the latter.

Hence, assuming the STM calculations to be the reference value (ULS load), a pile cap with higher failure load will be considered as safe. The optimization study in Experiment set 2 is therefore expected to show that lowering the depth, flank or bottom rebar percentage can still result in safe design since all specimens are expected to have higher load carrying capacity. Reduction in concrete grade however is expected to change the failure mechanism and the failure load to be lower than the design load.

Table 6.5: Measurements to be taken per pile cap

Load (kN)	Deflection (mm)	Max. Crack Width (mm)		Deformation in Pile Cap						
		On soffit	On face	P-B-1	P-B-2	P-B-3	P-B-4	P-F-1	P-F-2	P-F-3
100										
200										
300										
400										
500										
600										
700										
800										
...										
P_{ult}										
Cracking load										
Failure load										

Load (kN)	Strain in Rebar																			
	R-X-1	R-X-2	R-X-3	R-X-4	R-X-5	R-X-6	R-X-7	R-X-8	R-X-9	R-X-10	R-Y-1	R-Y-2	R-Y-3	R-Y-4	R-Y-5	R-Y-6	R-Y-7	R-Y-8	R-Y-9	R-Y-10
100																				
200																				
300																				
400																				
500																				
600																				
700																				
800																				
...																				
P_{ult}																				

6.3.3 Analysis of test results

The load-displacement curve of each pile cap shall be drawn using the values from [Table 6.5](#). It can also be used to determine the failure mode along with the observed cracking pattern as it will provide important data such as if the reinforcement yielded before failure or not and if there were tension stiffening after yielding.

The cracking pattern progression will help understand the crack evolution since initiation, the opening and closing of cracks during loading and unloading and the cracks at failure. Understanding this will help determine the failure mechanism.

The strain in the reinforcement shall be used to determine the forces and stresses in the tensile tie. This can then be compared to the calculated values using STM. The measured strains in the CCC and CTT nodes shall also be used to determine the stresses in the respective nodal zones. The lever arm can be calculated using the location of the tensile tie and the upper nodal zone (CCC node). These values can directly be compared to the results of the analytical calculation and numerical model.

7. Conclusion and Recommendation

7.1 Conclusion

The main objective of this research was to understand how non-linear finite element analysis can be used to improve the current design of pile caps. This research question was broken down into four sub questions. Thus, the conclusions deduced from the results of this research are summarised as follows:

1. In this thesis the accuracy of finite element modeling of pile caps was assessed by comparing the structural response of 5 benchmark experiments. The results show that failure mechanism, crack propagation and crack pattern can accurately be captured by the FEM model for all pile caps regardless of the failure mode. However, the accuracy of the load carrying capacity depends on the failure modes of the pile cap. The cracking, yielding and failure loads are predicted more accurately for pile caps with ductile failure. The difference between the failure loads in the FEM and the experiment is 5 - 7% for ductile failures while it varies between 25 - 42% for brittle failures. Hence, the numerical model is expected to result in safe predictions for pile caps with ductile failure mechanisms while it over estimates the capacity of pile caps with brittle failure.
2. The accuracy of the load deformation diagram depends on the geometry of the model used. Modelling pile caps using quarter of the geometry results in an initial peak behaviour that doesn't match experimental results as it assumes a perfectly symmetrical structure. This initial peak occurs because the model over estimates the load where post cracking stiffness occurs by 30% - 35%. However, the quarter model is still a good approach as it reduces computation time by 10 - 12 hours. It also accurately captures the crack pattern and failure mode of pile caps. Hence, keeping the initial peak in mind, the quarter model can be used to model pile caps.
3. The total strain cracking model estimates the load carrying capacity and predicts the crack pattern more accurately than the Kotsovos model. The latter underestimates the concrete tensile strength and exhibits a highly brittle behaviour in tension which results in the FEM model significantly underestimating the cracking load (by nearly 30%) while over estimating the failure load (by almost 20%) compared to the experiment. Unlike the total strain cracking model, the Kotsovos model does not take the concrete contribution to the tensile strength post-cracking.
4. The effect of confinement on the whole structure shall be considered in the design of pile caps. Confinement increases the strength of concrete structure and the critical strain which subsequently alters the effective stress-strain relationship. Although, the effect of confinement on crack pattern and failure mode of pile caps is observed to be minimal, it affects the stress and strains in the compressive strut resulting in a 30% and 10% reduction respectively.
5. Employing Shima bond-slip to model the reinforcement bars increase the carrying capacity of the FEM model by nearly 8% while the load at which post cracking stiffness is observed

is lower than embedded reinforcement. This is because a strain in the cracked elements activates un-cracked elements as the Shima model allows relative displacement between the reinforcement and concrete which increases the progression of cracks in the pile cap. This lowers the load at which fully developed cracks occur along the length of the symmetry face.

6. Comparison of numerical models with analytical calculations show that STM overestimates the stresses in the concrete by 40% – 70%, the stresses in the reinforcement at ULS and SLS by 50% – 65% as well as the crack width by 60 – 65%. This is because the effect of flank reinforcement and post cracking contribution of concrete are ignored in the STM. Moreover, the effect of confinement is only considered in the CCC node and not throughout the pile cap. Numerical model results are also closer to the experimental results than analytical calculations by 50% on average.

7. The parametric study of pile cap with punching failure shows that reducing the pile cap depth by 0.1m increases stress in the reinforcement by 25 - 35% since cracking occurs earlier as the depth of the pile cap decreases and the bottom reinforcement is activated earlier. The load carrying capacity reduces by 2 - 8% but remains greater than the design load.

8. Reduction of the bottom reinforcement by 10% in a pile cap with punching failure reduces the failure load slightly (2 - 8%) and increases the stress in the reinforcement and concrete (10 - 20%). However, it does not change the failure mechanism and the failure load remains higher than the design load.

9. The effect of flank reinforcement on the load carrying capacity and failure mechanism of a pile cap with punching failure is negligible. However, a 50% decrease in the number of flanks increases the stress in the bottom reinforcement by 20 - 25%. Furthermore, the crack along the symmetry face become wider as the number of flank rebars decreases since the confinement provided by the flank rebars is reduced which results in the concrete bulging out subsequently causing more cracking.

10. Changing the concrete grade affects the load carrying capacity of pile caps and the failure mechanism significantly. For a pile cap with punching failure, the failure load shows a 14% increase as the concrete quality is increased from 30MPa to 40MPa. The failure mode also changes from punching shear to corner shear failure. On the other hand, reducing the concrete grade from 30MPa to 25MPa results in an unsafe design as the failure load is lower than the design load. The failure mode changes from punching shear to flexural induced punching.

11. The proposed experiments on NFB-1 will have a punching failure and the failure load is expected to be between 1320 and 1640 kN. Moreover, the parametric study experiment is expected to show that lowering the pile cap geometry, rebar percentage and flank reinforcement result in a safe design where the failure load is higher the design load and the unity checks are less than one. On the other hand, reducing the concrete quality is expected to result in an unsafe design and change the failure mechanism from punching shear to flexure induced punching.

12. STM does not provide information about the crack pattern at failure and the failure mode is judged based on the critical unity check. Both, punching and crushing of concrete are caused by compressive stress exceeding the strength of concrete below the column, hence it can also not distinguish between the two. Furthermore, it ignores the contribution of concrete in tension after cracking (softening branch) and the confining effect of flank reinforcement, underestimating the pile cap capacity and leading to uneconomical design. Therefore, improving the current design approach using FEM can lead to saving on material and execution costs.

7.2 Recommendation

A few recommendation are made for future researchers to develop on this thesis and further investigate how to better capture the structural response of pile caps using FEM and the effect of various parameters on pile caps.

1. The results of this thesis show that the load deflection diagram of pile caps with ductile failure are better predicted with numerical models than those with brittle failure. The difference in the load deflection graph of the numerical model and experiment can be attributed to the load at which reduction in stiffness occurs. In the former, change in stiffness in the load deflection graph occurs when the cracking has developed along the full symmetry length of the pile cap soffit. This is not the case in the experiment as stiffness reduction occurs before fully developed cracks are obtained. Subsequently, the numerical model over estimates the load carrying capacity of brittle pile caps. Although various models have been developed by using the full pile cap and lowering the fracture energy, these have not resulted in an accurate model. Hence, further investigation must be done to find numerical techniques that can model brittle failure better.
2. The parametric study is conducted on a pile cap with punching failure. Thus, the effect of optimization on pile caps with other failure modes remain unknown. An investigation into this aspect should therefore be conducted to see if similar results can be obtained and the findings of this thesis can be generalized to all pile caps.
3. The parametric study in this thesis show that optimization of pile caps with punching failure is possible by lowering the pile cap depth, or the number of bottom and flank rebar. This results in a safe design as load capacity remain higher than the design load. However, the effect of these parameters have been investigated independently. Studies to understand the combinations of these optimisations would greatly help to understand if and how different optimisations affect each other and how this would affect the structural response of the pile cap.
4. The scope of this thesis was limited to modelling four-pile square pile caps loaded centrally. Thus, broadening this context, more geometric shapes and eccentrically loaded pile caps should be investigated. Adebar et al. [40] has investigated regular polygons and Lucia et al. [58] has conducted experiments on eccentrically loaded pile caps with bi-axial and uni axial bending. Moreover, all pile caps in the experiments and numerical models were loaded monotonically until failure. Thus, the effect of cyclic loading (loading and unloading) can be further explored. This would help to understand if FEM can be used to model all types of pile caps.
5. The parametric study in this research explored a limited number of specimens optimized in geometry, rebar percentage and concrete quality. Since all specimens particularly those with lower geometry and rebar percentage resulted in a safe design, there still remains room for more optimization. Hence, a numerical investigation can be conducted to see how far optimization of these parameters can be done. An in-depth look into this would help explain how far these parameters can be lowered before safety becomes an issue.
6. The current STM calculation does not account for the contribution of flank reinforcement and concrete contribution to the tensile strength post-cracking. Hence, future designs of pile caps should take these parameters into account to obtain a safe design without underestimating the capacity of the pile cap. This would result in lesser use of materials and subsequently lowers the overall cost.

Bibliography

- [1] M. Sushilkumar , I. Ramakant. “Comparision of Moments for Pile Cap Design”. In: *Soil Mechanics and Foundation Engineering* 56.6 (2019), pp. 414–419.
- [2] ACI. “Building Code Requirements for Structural Concrete and Commentary”. In: *American Concrete Institute* (2008).
- [3] J. Clarke. “Behaviour and design of pile caps with four piles”. In: *Technical report of the Cement and Concrete Association* 42.42–489 (1973).
- [4] S. Ahmed, A. Shah, S. Zaman. “Evaluation of the Shear Strength of Four Pile Cap Using Strut and Tie Model (STM)”. In: *Chinese Journal Institute of Eng.* 32.2 (2009), pp. 243–249.
- [5] CEN. “Eurocode 2: Design of concrete structures–part 1-1: General rules and rules for buildings. EN 1992-1-1:2005”. In: *Thomas Telford Publishing* (2005).
- [6] S. Mustafa. “Optimization of reinforcement in pile caps using DIANA: Comparison of manual calculation with 2D and 3D models”. In: *ABT* (2019).
- [7] J. Srivastava. “Optimization of reinforcement in 4-pile pilecap using DIANA”. In: *ABT* (2019).
- [8] C. O. COBc. “EC 2 In de Praktijk Rekenvoorbeelden”. In: *Betonvereniging* (2010).
- [9] DIANA FEA, J. Manie. “User’s manual – release 10.3”. In: *DIANA FEA bv* (2019).
- [10] W. Ritter. “Die bauweise hennebique (the hennebique construction method)”. In: *Die Bauweise Hennebique, Schweizerische Bauzeitung* 7.33 (1899), pp. 41–61.
- [11] F. Leonhardt. “Reducing the shear reinforcement in reinforced concrete beams and slab”. In: *Mag. Concrete Research* 17.53 (1965), p. 187.
- [12] B. Thurlimann, P. Marti J. Pralong. “Advanced lecture for Civil Engineer”. In: *Institut fur Bautechnik und Konstruktion* 17.53 (1983), pp. 160–162.
- [13] H. Kupfer. “Expansion of Morsch’s truss analogy by application of the principle of minimum strain energy”. In: *CEB Bulletin* 17.40 (1964), pp. 50–52.
- [14] J. Schlaich, K. Schäfer, M. Jennewein. “Design and detailing of structural concrete using strut-and-tie models”. In: *PCI Journal* (1987), pp. 75–150.
- [15] C. Williams, D. Deschenes, O. Bayrak. “Strut-and-Tie Model Design Examples for Bridges: Final Report”. In: *The University of Texas at Austin* (2012).
- [16] P. Baniya, S. Guner. “Specialized strut-and-tie method for rapid strength prediction of bridge pier caps”. In: *Engineering Structures* 198.6 (2019), pp. 1–9.
- [17] P. Adebar, L. Zhou. “Design of Deep Pile Caps by Strut-and-Tie Models”. In: *ACI Structural Journal* 93.4 (1996), pp. 1–12.
- [18] FIB. “FIB Model Code for Concrete Structures 2010”. In: *International Federation for Structural Concrete* (2010).
- [19] Y.M. Yun, H.S. Chae, J.A. Ramirez. “A Three-Dimensional Strut-and Tie Model for a Four-Pile Reinforced Concrete Cap”. In: *Journal of Advanced Concrete Technology* 17 (July 2019), pp. 365–380.
- [20] A. Mathern, G. Chantelot. “Strut-and-tie modelling of reinforced concrete pile caps”. In: *Chalmers University of Technology* (2010).

- [21] J. Schlaich, K. Schafer. "Design and detailing of structural concrete using strut-and-tie models". In: *The Structural Engineer* 69.6 (1991), pp. 113–125.
- [22] S. Dey, M.M. Karthik. "Modelling four-pile cap behaviour using three-dimensional compatibility strut-and-tie method". In: *Engineering Structures* 198 (Aug. 2019), pp. 365–380.
- [23] D. Ngo, A.C. Scordelis. "Finite Element Analysis of Reinforced Concrete Beams". In: *ACI Journal Proceedings* 64 (1967), pp. 152–163.
- [24] A.H. Nilson. "Internal Measurement of Bond Slip". In: *ACI Journal Proceedings* 52 (1972), pp. 439–441.
- [25] H.A. Franklin. "Non-Linear Analysis of Reinforced Concrete Frames and Panels". In: *University of California* (1970).
- [26] J.G. Rots, J. Blaauwendraad. "Crack Models for Concrete: Discrete or Smeared? Fixed, Multi-Directional or Rotating?" In: *HERON* 34.1 (1989).
- [27] Y.R. Rashid. "Analysis of Prestressed Concrete Pressure Vessels". In: *Nuclear Engineering and Design* 7.4 (1968), pp. 334–344.
- [28] Z.P. Bazant, P.G. Gambarova. "Rough cracks in reinforced concrete". In: *ASCE journal of the structural engineering* 4 (1980), pp. 819–842.
- [29] T. Claus. "Non-Linear Finite Element Analysis of Shear Critical Reinforced Concrete Beams". In: *TU Delft University of Technology* 2 (2009).
- [30] R.G. Selby and F.J. Vecchio. "A constitutive model for analysis of reinforced concrete solids". In: *Can. J. Civ. Eng* 24 (1997), pp. 460–470.
- [31] M.A.N. Hendriks, A. de Boer, B. Belletti. "Guidelines for nonlinear finite element analysis of concrete structures". In: *Rijkswaterstaat Technisch Document (RTD), Rijkswaterstaat Centre for Infrastructure, RTD,1016:2012* (2017).
- [32] S.C. Jain, J.B. Kennedy. "Yield Criterion for Reinforced Concrete Slabs". In: *Journal of Structural Division, ASCE* 100.ST3 (1974), pp. 631–644.
- [33] S. Balakrishnan, D.W. Murray. "Concrete Constitutive Model for NLFEM Analysis of Structures". In: *Journal of Structural Engineering* 114.7 (1988), pp. 1449–1466.
- [34] M. Engen, M. Hendriks, J.A. Øverli. "Non-linear finite element analyses applicable for the design of large reinforced concrete structures". In: *European Journal of Environmental and Civil Engineering* (2017).
- [35] M.D. Kotsovos. "A mathematical description of the strength properties of concrete under generalized stress". In: *Magazine of Concrete Research* 108.31 (1979), pp. 151–158.
- [36] C. Turgut, L. Jason, L. Davenn. "Structural-scale modeling of the active confinement effect in the steel-concrete bond for reinforced concrete structures". In: *Finite Elements in Analysis and Design* 172 (2020), pp. 1–15.
- [37] N. Øystad-Larsena, E. Erduranb, A. M. Kaynia. "Evaluation of effect of confinement on the collapse probability of reinforced concrete frames subjected to earthquakes". In: *Procedia Engineering* 199 (2017), pp. 784–789.
- [38] R.G. Selby, F.J. Vecchio. "A constitutive model for analysis of reinforced concrete solids". In: *Can. J. Civ. Eng.* 24 (1997), pp. 460–470.
- [39] P.S. Huyakorn, E.P. Springer, V. Givanasen and T.D. Wadsworth. "Three-dimensional finite element techniques for simulating unconfined flow with seepage faces". In: *Water Resources Research* 2.13 (1986).
- [40] P. Adebar, D. Kuchma, M.P. Collins. "Strut-and-Tie Models for the Design of Pile Caps: An Experimental Study". In: *ACI- Structural Journal* 87.1 (1990), pp. 81–92.
- [41] ACI. "Building Code Requirements for Structural Concrete and Commentary". In: *American Concrete Institute* (2005).
- [42] Concrete Reinforcing Steel Institute. Engineering Practice Committee. "CRSI Handbook". In: *Concrete Reinforcing Steel Institute* (1978).
- [43] H. Sezen. "Seismic Behavior and Modeling of Reinforced Concrete Building Columns". In: *Ph.D. Thesis. University of California* (2002).

- [44] S. Höper, U. Kowalsky, D. Dinkler. “Micro-structure related modelling of ultra-high-performance fibre reinforced concrete (UHPFRC) subjected to cyclic tensile loading”. In: *Journal of Structural Engineering* 18.1 (2018), pp. 371–382.
- [45] M. Saatcioglu, J.M. Alsiwat, G. Ozcebe. “Hysteretic Behavior of Anchorage Slip in Reinforced Concrete Members”. In: *Journal of Structural Engineering* 118.9 (1992), pp. 2421–2438.
- [46] TGB Betonconstructies. “Regulations for concrete - Structural requirements and calculation methods”. In: *TGB Concrete structures* (1995).
- [47] N.B. Hobbs, P. Stein. “An investigation into the stress distribution in pile caps with some notes on design”. In: *Proceedings of the Institution of Civil Engineers* (1957), pp. 599–628.
- [48] J.L. Blévoit, R. Frémy. “Semelles sur Pieux”. In: *Institute Tech. du Bâtiment et des Travaux Publics* 20.230 (1967), pp. 223–295.
- [49] G. Sabnis, A.B. Gogate. “Investigation of Thick Slap (Pile Cap) Behaviour”. In: *ACI Journal* (1984).
- [50] K. Suzuki, K. Otsuki, T. Tsubata. “Influence of bar arrangement on ultimate strength of four-pile caps”. In: *Transactions Japanese Concrete Institute* (1998), pp. 195–202.
- [51] K. Suzuki, K. Otsuki, T. Tsubata. “Experimental Study on Bending Strength of Four Pile Caps”. In: *Transactions Japanese Concrete Institute* (1991), pp. 195–225.
- [52] C.S. Iyer, P. Krishna. “Nonlinear Finite Element Analysis of Reinforced Concrete Four-Pile Caps”. In: *Engineering Structures* 57.4 (1995), pp. 605–622.
- [53] K. Suzuki, K. Otsuki, T. Tsubata. “Influence of Edge Distance on Failure Mechanism of Pile Caps”. In: *Transactions Japanese Concrete Institute* 22 (2000), pp. 361–367.
- [54] K. Suzuki, K. Otsuki, T. Tsubata. “Experimental study on corner shear failure of pile caps”. In: *Transactions Japanese Concrete Institute* 23 (2001), pp. 303–310.
- [55] Q. Gu, C. Sun, S. Peng. “Experimental Study on Deep Four-Pile Caps with Different Reinforcement Layouts Based on 3D Strut-and-Tie Analogy”. In: *Key Engineering Materials* 400-402 (2008), pp. 917–922.
- [56] T. Wang, L.D. Lijun, K. Yin. “Experimental study of failure mechanism of thick pile caps”. In: *IOP Publishing* (2017).
- [57] J. Cao, A.G. Bloodworth. “Shear Capacity of Reinforced Concrete Pile Caps”. In: *IABSE (International Association for Bridge and Structural Engineering)* (2007), pp. 1–8.
- [58] L. Miguel-Tortola, P.F. Miguel, L. Pallarés. “Strength of pile caps under eccentric loads: Experimental study and review of code provisions”. In: *Engineering Structures* 182 (2019), pp. 251–267.
- [59] CEN. “Eurocode 2: Design of concrete structures—part 1-1: General rules and rules for buildings. EN 1992-1-1:2004”. In: *Thomas Telford Publishing* (2013).
- [60] P. Evangelidou. “Probabilistic nonlinear finite element analysis of reinforced concrete beams without shear reinforcement”. In: *Civil Engineering and Geosciences, TU Delft* (2016).
- [61] E. Morten Engen, M.A.N. Hendriks, J.A. Øverli. “Solution strategy for non-linear finite element analyses of large reinforced concrete structures”. In: *Structural Concrete* 2.3 (2015), pp. 389–397.
- [62] J.W. Park, D. Kuchma, R. Souza. “Strength Predictions of Pile Caps by a Strut-and-Tie Model Approach”. In: *Canadian Journal of Civil Engineering* 35.12 (2008), pp. 1399–1413.
- [63] ACI. “Building Code Requirements for Structural Concrete and Commentary”. In: *American Concrete Institute* (2014).
- [64] ir. Jan-Willem. “Project Nieuwbouw Feringa Building Berekening deel C 1.1: Sterkteberekening in-situ betonconstructie fundering”. In: *ABT bv* (2018).
- [65] ir. F.P.M. van Gerven. “Nieuwbouw Kloosterboer vastgoed Eemhaven te Rotterdam Fundering Low Bay”. In: *ABT bv* (2020).

- [66] National Ready Mixed Concrete Association. "Concrete CO₂ Fact Sheet". In: *ABT bv* (2008), pp. 2–13.
- [67] G.P. Hammond, C.I. Jones. "Embodied energy and carbon in construction mater". In: *Proc. Institute of Civil Engineering* 2.161 (2008), pp. 87–98.
- [68] Technische Commissie CEN/TC. "NEN-EN 206:2016+A1:2016+NEN 8005:2014+C1:2017 Beton". In: *CEN 2* (2014), pp. 57–96.
- [69] Technische Commissie CEN/TC. "Metrological aspects of non-automatic weighing instruments". In: *NEN-EN 45501:2015, CEN 2* (2015).
- [70] Technische Commissie CEN/TC. "Testing concrete mortar - Part 1: Sampling and testing equipment". In: *NEN-EN 12350-1: 2019, CEN 2* (2019).
- [71] Technische Commissie CEN/TC. "Testing of hardened concrete - Part 3: Compressive strength of test pieces". In: *NEN-EN 12390-3: 2019, CEN 2* (2019).
- [72] Technische Commissie CEN/TC. "Steel for reinforcing concrete - Weldable reinforcing steel - General". In: *NEN-EN 10080: 2005, CEN 2* (2005).
- [73] M.G. Miguel, T. Takeya, J.S. Giongo. "Structural behaviour of three-pile caps subjected to axial compressive loading". In: *Materials and Structures* 41 (2007), pp. 85–98.
- [74] S. Singh. "Influence of Interface and Type of Strain Hardening Cementitious Composite (SHCC) on Crack Control in SHCC-Concrete Hybrid Beams". In: *TU Delft Repository* (2019), pp. 40–46.

A. Past ABT Projects Overview

Table A.1: Pile caps from past ABT projects

Name	Geometry (mm)	Reinforcement Percentage (ρ)	Rebar Layout*	Flank Reinf	Lever Arm (mm)	Design Load (kN)	Crack Width	Reported Results		
								Shear Reinf	Anchorage Length	Stress in Rebar
<i>Nieuwbouw Feringa Building</i>										
NFB-1	2600X2600X1400	0.28%	G	\varnothing 12@100	956	7500	0.35	✗	✓	✓
NFB-2	2600X2600X1000	0.40%	G	\varnothing 12@100	680	-	-	✗	✓	✓
<i>Feniks Rotterdam**</i>										
Feniks - C	3000X3000X1400	0.25%	G	7 \varnothing 20	860	8800	-	✗	✓	✓
Feniks - H	3000X3000X1400	0.23%	G	\varnothing 12@150	860	9243	-	✗	✓	✓
<i>Ahoy ICC Rotterdam</i>										
Ahoy – D1	2050X2050X1200	0.29%	G	10 \varnothing 20	835	5202	0.4	✗	✓	✓
Ahoy – E1	2600X2600X1200	0.41%	G	7 \varnothing 25	904	4922	0.38	✗	✓	✓
Ahoy – K1	2750X2750X1640	0.19%	G	-	1260	2306	0.37	✗	✓	✓
Ahoy – M1	3000X3000X1200	0.26%	G	-	880	3474	0.38	✗	✓	✓
Ahoy – N1	3750X3750X1200	0.34%	G	-	1070	3544	0.43	✗	✓	✓
Ahoy – R1	2050X2050X1640	0.19%	G	-	1150	4119	0.39	✗	✓	✓

* G = grid, BS = Bundled Square

** Feniks project was initially calculated using the sectional method and the reinforcements were later checked according to Eurocode

B. Experimental Data

Table B.1: Pile cap data from experiments

Name	Geometry (LxWxH)	Rebar Percentage (ρ)	Failure Mode*	Rebar Layout**	Failure Load (kN)	Pile Design***	Reported Results				
							Crack Width	Load Graph	Strain in Rebar	Stress in Rebar	Crack Pattern
<i>Sam and Iyer [52]</i>											
SS1	330X330X152	0.20%	p	G	250.43	STM	✗	✗			
SS2	330X330X152	0.14%	p	G	244.65	STM	✗	✗			
SS3	330X330X152	0.18%	p	G	247.99	STM	✗	✗			
SS4	330X330X152	0.28%	p	G	225.75	STM	✗	✗			
SS5	330X330X152	0.54%	p	G	263.56	STM	✗	✗			
SS6	330X330X152	0.80%	p	G	280.24	STM	✗	✗			
<i>Suzuki et al. [50]***</i>											
BP-20-2	900X900X200	0.47%	f + c	G	480	SM	✗	✓			
BPC-20-2	900X900X200	0.47%	f + p	BS	529	SM	✗	✓			
BP-25-2	900X900X250	0.44%	c	G	755	SM	✗	✓			
BPC-25-2	900X900X250	0.44%	f + p	BS	813	SM	✗	✓			

* c = Corner Shear Failure; f = Flexural; p = Punching Shear Failure

** G = grid; BS = Bundled Square

*** SM = Sectional Method; STM = Strut and Tie Model

**** Though all experimental pile caps are designed using sectional method, the failure load was predicted using the strut and tie model of ACI 318-05 and CSA A23.3

Name	Geometry (LxWxH)	Rebar Percentage (ρ)	Failure Mode*	Rebar Layout**	Failure Load (kN)	Pile Design***	Reported Results				
							Crack Width	Load Graph	Strain in Rebar	Stress in Rebar	Crack Pattern
BP-20-30-2	800X800X200	0.39%	f + c	G	480	SM	✗	✓			
BPC-20-30-2	800X800X200	0.39%	f	BS	495	SM	✗	✓			
BP-30-30-2	800X800X300	0.31%	f + c	G	907	SM	✗	✓			✓
BPC-30-30-2	800X800X300	0.31%	f + c	BS	1029	SM	✗	✓			
BP-30-25-2	800X800X300	0.31%	c	G	725	SM	✗	✓			
BPC-30-25-2	800X800X300	0.31%	f + c	BS	872	SM	✗	✓			
BDA-70X90-2	700X900X300	0.36%	f + c	G	755	SM	✗	✓			
BDA-80X90-2	800X900X300	0.31%	f + c	G	853	SM	✗	✓			
BDA-90X90-2	900X900X300	0.28%	f + c	G	921	SM	✗	✓			
BDA-100X90-2	1000X900X300	0.25%	f + c	G	931	SM	✗	✓			
<i>Suzuki et al. [53]****</i>											
BDA-20-25-70-1	700X700X200	0.27%	f	G	294	SM	✗	✓	✓		✓
BDA-20-25-80-1	800X800X200	0.24%	f	G	304	SM	✗	✓			
BDA-20-25-90-1	900X900X200	0.21%	f	G	333	SM	✗	✓	✓		✓
BDA-30-25-70-1	700X700X300	0.24%	f + c	G	662	SM	✗	✓	✓		✓
BDA-30-25-80-1	800X800X300	0.21%	f + c	G	696	SM	✗	✓			
BDA-30-25-90-1	900X900X300	0.19%	f + c	G	764	SM	✗	✓	✓		✓
BDA-40-25-70-1	700X700X400	0.23%	c	G	1019	SM	✗	✓	✓		✓
BDA-40-25-80-1	800X800X400	0.23%	f	G	1117	SM	✗	✓			
BDA-40-25-90-1	900X900X400	0.23%	f	G	1176	SM	✗	✓	✓		✓
<i>Gu et al. [55]</i>											
CT4-1	600X600X300	0.42%	p	G	700	STM	✗	✓		✓	✓
CT4-2	600X600X300	0.42%	p	BS	700	STM	✗	✓		✓	✓
<i>Wang et al. [56]</i>											
ZJCT1	600X600X300	0.42%	f + c	G	810	STM	✗	✗			
CT1	600X600X300	0.42%	f + c	G	700	STM	✗	✗			

* c = Corner Shear Failure; f = Flexural; p = Punching Shear Failure

** G = grid; BS = Bundled Square

*** SM = Sectional Method; STM = Strut and Tie Model

**** Though all experimental pile caps are designed using sectional method, the failure load was predicted using the strut and tie model of ACI 318-05 and CSA A23.3

Name	Geometry (LxWxH)	Rebar Percentage (ρ)	Failure Mode*	Rebar Layout**	Failure Load (kN)	Pile Design***	Reported Results				
							Crack Width	Load Graph	Strain in Rebar	Stress in Rebar	Crack Pattern
<i>Lucia et al. [58]</i>											
4P-N-A1	1150X1150X250	0.47%	f + p	BS	613.9	STM	✗	✓			✓
4P-N-A2	1150X1150X250	0.65%	f + p	G	821.7	STM	✗	✓			
4P-N-A3	1150X1150X250	0.65%	f + p	G	981.5	STM	✗	✓			✓
4P-N-B1	1150X1150X350	0.20%	f + p	BS	756.2	STM	✗	✓			✓
4P-N-B2	1150X1150X350	0.27%	f + p	G	872.6	STM	✗	✓			✓
4P-N-B3	1150X1150X350	0.27%	f + p	G	1127.8	STM	✗	✓			✓
4P-N-C1	1150X1150X450	0.12%	f	BS	957.5	STM	✗	✓			✓
4P-N-C2	1150X1150X450	0.17%	f + p	G	1173.9	STM	✗	✓			
4P-N-C3	1150X1150X450	0.17%	f	G	1317.3	STM	✗	✓			✓

* c = Corner Shear Failure; f = Flexural; p = Punching Shear Failure

** G = grid; BS = Bundled Square

*** SM = Sectional Method; STM = Strut and Tie Model

C. DIANA Script

```

newProject( "Directory/Name", 100 )
setModelAnalysisAspects( [ "STRUCT" ] )
setModelDimension( "3D" )
setDefaultMeshOrder( "QUADRATIC" )
setDefaultMesherType( "HEXQUAD" )
setDefaultMidSideNodeLocation( "ONSHAP" )
##### DEFINING VARIABLES

import math
pi = math.pi
Confinement = 'Y'           #Y if confinement is applied and N if not
Rebar = 'E'                 #E if rebar is embedded or S if truss bond slip model
Flank = 'Y'                 #Yes (Y) if there is flank or No (N) if not
Column = 'N'                #Yes (Y) if column has reinforcement and No (N) if not
Res = 'Y'                   #Y if residual compression and tension strength are
                             #different than zero and N if it's zero
Safety_factor = 'M'        #M for mean, K for characteristic and D for Design
                             #material properties

###Pile Cap
Length_pilecap = 1.2       #Pile cap Length
Width_pilecap = 1.2        #Pile cap width
Height_pilecap = 0.7       #Pile cap height

###Piles
Radius_pile = 0.1          #Pile radius
Pile_Dist_Left = 0.3       #Distance of the pile center from the edge in the x direction
Pile_Dist_Bottom = 0.3     #Distance of the pile center from the edge in the y direction

###Column
Length_col = 0.3           #Column Length
Width_col = 0.3            #Column Width
Height_col = 0.3           #Column Height
Col_Dist_Left = 0.45       #Column edge distance from the edge in the x direction
Col_Dist_Bottom = 0.45    #Column edge distance from the edge in the y direction

###Steel plate
Stl_pl_thick = 0.5         #thickness of the steel plate thickness
Stl_pl_density = 7850      #density of the steel plate
Stl_pl_poisson = 0.3       #poisson ratio for steel plate
E_plate = 800e+9

###Flank Reinforcement
No_flank = 5               ##Number of flank reinforcement
Flank_dis = 0.11           ##Distance between flank reinforcement
Flank_dia = 0.008         ##Diameter of flank reinforcement
Flank_area = pi*(Flank_dia**2)*0.25 ##Flank Reinforcement area

###Pilecap Reinforcement
Conc_bot_cover = 0.05      ##Concrete cover at the bottom
Reinf_dia_bottom = 0.016   ##Bottom Reinforcement diameter
Reinf_dia_top = 0.008      ##Top Reinforcement diameter
Rebar_area_bot = pi*(Reinf_dia_bottom**2)*0.25 ##Bottom Reinforcement area
Rebar_area_top = pi*(Reinf_dia_top**2)*0.25   ##Top Reinforcement area
No_bot_reinf = 5           ##Total number of bot reinforcement over half of pilecap
dis_x_1 = 0.12             ##bot rebar center to center distance in the x direction
dis_y_1 = 0.12             ##bot rebar center to center distance in the y direction
No_top_reinf = 5           ##Number of top reinforcement over half of pilecap
dis_x_2 = 0.12             ##Top rebar center to center distance in the x direction
dis_y_2 = 0.12             ##Top rebar center to center distance in the y direction
Conc_side_cover = Conc_bot_cover + 1*Reinf_dia_bottom + Flank_dia ##Concrete cover on the side of
the piles
Rebar_position = Conc_bot_cover + 1.5*Reinf_dia_bottom + Flank_dia ##Position of the first
Longitudinal rebar
Rebar_position_top = Conc_bot_cover + 3.5*Reinf_dia_bottom + Flank_dia
Anch_length = 0.3          ##Vertical length of anchorage rebar
Anch_angle = pi/2          ##Inclined angle of anchorage rebar

###Concrete properties
Elin = 15e+9
Poison = 0.15
Density = 2500
#Characteristic
fck = 30e+6

```

```

Gf_k = 73*(fck/10**6)**0.18
Gc_k = 250*Gf_k
Eck = 2.15e+10*(fck/10**7)**(1/3)
#Mean
fcm = fck + 8e+6
fctm = 0.3*(fck**(2/3))*100
fctk = 0.7*fctm
Gf_m = 73*(fcm/10**6)**0.18
Gc_m = 250*Gf_m
Ecm = 2.15e+10*((fcm/10**7)**(1/3))
#Design
fcd = fck/1.5
fctd = fctk/1.5
Gf_d = 73*(fcd/10**6)**0.18
Gc_d = 250*Gf_d
Ecd = 2.15e+10*(fcd/10**7)**(1/3)

Res_comp = 10000          ##Residual compression strength in N/M2
Res_tens = 1000          ##Residual tension strength N/M2

###Rebar
Es = 200e+9
fym = 552.34e+6
fum = 594e+6
A = fum/fym
fyk = 0.9057*fym
fuk = A*fyk
fyd = fyk/1.15
fud = A*fyd
e1_m = 0.05 - (fym/Es)    ##Yeild Strain (mean)
e2_m = e1_m+0.001        ##Ultimate strain (mean)
e1_d = 0.05 - (fyd/Es)   ##Yeild Strain (design)
e2_d = e1_d+0.001        ##Ultimate strain (design)
e1_k = 0.05 - (fyk/Es)   ##Yeild Strain (characteristic)
e2_k = e1_k+0.001        ##Ultimate strain (characteristic)

###Mesh
Mesh_Size = 0.09         ##Element size for pile and column height mesh

###Additional inputs for truss bond slip model
Bot_rebar_per = pi*Reinf_dia_bottom          ###Perimeter of bottom reinforcement
Top_rebar_per = pi*Reinf_dia_top             ###Perimeter of top reinforcement
Flank_rebar_per_3 = pi*Flank_dia             ###Perimeter of bottom reinforcement
Norm_stiffness = (100*Ecd/Mesh_Size)         ###Normal stiffness modulus Shear_stiffness =
0.1*Norm_stiffness                          ###Shear stiffness modulus

##### CREATING GEOMETRY
###Pile cap
createSheet( "Pile cap", [[ 0, 0, 0 ],[ Length_pilecap/2, 0, 0 ],[ Length_pilecap/2, Width_pilecap/2,
0 ],[ 0, Width_pilecap/2, 0 ]] )

###Piles
createSheetCircle( "pile 1", [ Pile_Dist_Left, Pile_Dist_Bottom, 0 ], [ 0, 0, 1 ], Radius_pile )
createPolyline( "polygon 1", [[ Pile_Dist_Left - Ext_rect_size/2, Pile_Dist_Bottom - Ext_rect_size/2,
0 ],[ Pile_Dist_Left + Ext_rect_size/2, Pile_Dist_Bottom - Ext_rect_size/2, 0 ],[ Pile_Dist_Left +
Ext_rect_size/2, Pile_Dist_Bottom + Ext_rect_size/2, 0 ],[ Pile_Dist_Left - Ext_rect_size/2,
Pile_Dist_Bottom + Ext_rect_size/2,0 ]], True )
createPolyline( "polygon 2", [[ Pile_Dist_Left - Int_rect_size/2, Pile_Dist_Bottom - Int_rect_size/2,
0 ],[ Pile_Dist_Left + Int_rect_size/2, Pile_Dist_Bottom - Int_rect_size/2, 0 ],[ Pile_Dist_Left +
Int_rect_size/2, Pile_Dist_Bottom + Int_rect_size/2, 0 ],[ Pile_Dist_Left - Int_rect_size/2,
Pile_Dist_Bottom + Int_rect_size/2,0 ]], True )
createLine( "Line 1", [ Pile_Dist_Left + Int_rect_size/2, Pile_Dist_Bottom + Int_rect_size/2, 0 ], [
Pile_Dist_Left + Radius_pile * math.cos(pi/4), Pile_Dist_Bottom + Radius_pile * math.cos(pi/4), 0 ] )
createLine( "Line 2", [ Pile_Dist_Left + Radius_pile * math.cos(pi/4), Pile_Dist_Bottom + Radius_pile
* math.cos(pi/4), 0 ], [ Pile_Dist_Left + Ext_rect_size/2, Pile_Dist_Bottom + Ext_rect_size/2, 0 ] )
mirror( [ "Line 1", "Line 2" ], [ Pile_Dist_Left, 0, 0 ], [ True, False, False ], True )
mirror( [ "Line 1", "Line 2", "Line 3", "Line 4" ], [ 0, Pile_Dist_Bottom, 0 ], [ False, True, False
], True )
projection( SHAPEFACE, "Pile cap", [[ Length_pilecap/2, Width_pilecap/2, 0 ]], [ "pile 1", "polygon
1", "polygon 2", "Line 1", "Line 2", "Line 3", "Line 4", "Line 5", "Line 6", "Line 7", "Line 8" ], [
0, 0, -1 ], True )
removeShape( [ "pile 1", "polygon 1", "polygon 2", "Line 1", "Line 2", "Line 3", "Line 4", "Line 5",
"Line 6", "Line 7", "Line 8" ] )
extrudeProfile( [ "Pile cap" ], [ 0, 0, Height_pilecap ] )

```

```

createSheetCircle("pile", [Pile_Dist_Left, Pile_Dist_Bottom, -Stl_pl_thick], [0, 0, 1], Radius_pile)
rotate(["pile"], [Pile_Dist_Left, Pile_Dist_Bottom, -Stl_pl_thick], [0, 0, 1], pi/4)
extrudeProfile(["pile"], [0, 0, Stl_pl_thick])
createPolyline("polygon 2", [[ Pile_Dist_Left - Int_rect_size/2, Pile_Dist_Bottom - Int_rect_size/2,
-Stl_pl_thick],[ Pile_Dist_Left + Int_rect_size/2, Pile_Dist_Bottom - Int_rect_size/2, -Stl_pl_thick
],[ Pile_Dist_Left + Int_rect_size/2, Pile_Dist_Bottom + Int_rect_size/2, -Stl_pl_thick ],[
Pile_Dist_Left - Int_rect_size/2, Pile_Dist_Bottom + Int_rect_size/2,-Stl_pl_thick ]], True )
createLine( "Line 1", [ Pile_Dist_Left + Int_rect_size/2, Pile_Dist_Bottom + Int_rect_size/2, -
Stl_pl_thick ], [ Pile_Dist_Left + Radius_pile * math.cos(pi/4), Pile_Dist_Bottom + Radius_pile *
math.cos(pi/4), -Stl_pl_thick ] )
mirror( [ "Line 1" ], [ Pile_Dist_Left, 0, -Stl_pl_thick ], [ True, False, False ], True )
mirror( [ "Line 1", "Line 8"], [ 0, Pile_Dist_Bottom, -Stl_pl_thick ], [ False, True, False ], True )

projection( SHAPEFACE, "pile", [[Pile_Dist_Left, Pile_Dist_Bottom, -Stl_pl_thick ]], [ "polygon 2",
"Line 1", "Line 10", "Line 8", "Line 9" ], [ 0, 0, -1 ], True )
removeShape( [ "polygon 2", "Line 1", "Line 10", "Line 8", "Line 9" ] )

createPointBody("point 1", [Pile_Dist_Left, Pile_Dist_Bottom, -Stl_pl_thick])
projection(SHAPEFACE, "pile", [[Pile_Dist_Left, Pile_Dist_Bottom, -Stl_pl_thick]], ["point 1"], [0, 0,
-1], True)
removeShape(["point 1"])

###Column
createSheet( "Column", [[ Col_Dist_Left, Col_Dist_Bottom, Height_pilecap ],[ Col_Dist_Left +
Length_col/2, Col_Dist_Bottom, Height_pilecap ],[ Col_Dist_Left + Length_col/2, Col_Dist_Bottom +
Width_col/2, Height_pilecap ],[ Col_Dist_Left, Col_Dist_Bottom + Width_col/2, Height_pilecap ]] )
extrudeProfile( [ "Column" ], [ 0, 0, Height_col ] )

addSet(SHAPESET, "Shapes 1")
rename(SHAPESET, "Shapes 1", "Bottom Rebar")
createLine( "HR_bot_1", [ Conc_side_cover, Rebar_position, Conc_bot_cover ], [ Length_pilecap / 2 ,
Rebar_position, Conc_bot_cover ] )
createLine( "VR_bot_1", [ Rebar_position, Conc_side_cover, Conc_bot_cover + Reinf_dia_bottom], [
Rebar_position, Width_pilecap / 2 , Conc_bot_cover + Reinf_dia_bottom] )
createArc( "h_bend_bot_1", [ Conc_side_cover, Rebar_position , Conc_bot_cover + Reinf_dia_bottom*2.5 ]
, [ 0, 1, 0 ], [ 0, 0, -1 ], 2.5*Reinf_dia_bottom, 0, pi/2 )
createArc( "vbend_bot_1", [ Rebar_position, Conc_side_cover, Conc_bot_cover + Reinf_dia_bottom*3.5], [
-1, 0, 0 ], [ 0, 0, -1 ], 2.5*Reinf_dia_bottom, 0, pi/2 )
createLine( "h_ext_bot_1", [ Conc_side_cover - 2.5*Reinf_dia_bottom, Rebar_position, Conc_bot_cover +
Reinf_dia_bottom * 2.5 ], [ (Anch_length / math. tan(Anch_angle)) + Conc_side_cover -
2.5*Reinf_dia_bottom, Rebar_position, Anch_length + Conc_bot_cover + Reinf_dia_bottom * 2.5 ] )
createLine( "v_ext_bot_1", [ Rebar_position, Conc_side_cover - 2.5*Reinf_dia_bottom , Conc_bot_cover +
Reinf_dia_bottom*3.5], [ Rebar_position, (Anch_length / math. tan(Anch_angle)) + Conc_side_cover -
2.5*Reinf_dia_bottom , Anch_length + Conc_bot_cover + Reinf_dia_bottom * 3.5 ] )
arrayCopy(["HR_bot_1", "h_bend_bot_1", "h_ext_bot_1"], [0, dis_y_1 , 0], [0, 0, 0], [0, 0, 0],
No_bot_reinf - 1)
arrayCopy(["VR_bot_1", "vbend_bot_1", "v_ext_bot_1"], [dis_x_1, 0, 0], [0, 0, 0], [0, 0, 0],
No_bot_reinf - 1)

addSet(SHAPESET, "Shapes 1")
rename(SHAPESET, "Shapes 1", "Top Rebar")
createLine( "HR_top_1", [ Conc_side_cover, Rebar_position_top, Height_pilecap -Conc_bot_cover ], [
Length_pilecap / 2 , Rebar_position_top, Height_pilecap - Conc_bot_cover] )
createLine( "VR_top_1", [ Rebar_position_top, Conc_side_cover, Height_pilecap - Conc_bot_cover -
Reinf_dia_top], [ Rebar_position_top, Width_pilecap / 2 , Height_pilecap - Conc_bot_cover -
Reinf_dia_top] )
createArc( "h_bend_top_1", [ Conc_side_cover, Rebar_position_top , Height_pilecap - Conc_bot_cover -
Reinf_dia_top*2.5 ], [ 0, 1, 0 ], [ 0, 0, -1 ], 2.5*Reinf_dia_top, pi/2 , pi/2)
createArc( "vbend_top_1", [ Rebar_position_top, Conc_side_cover, Height_pilecap - Conc_bot_cover -
Reinf_dia_top*3.5], [ -1, 0, 0 ], [ 0, 0, -1 ], 2.5*Reinf_dia_top, pi/2 , pi/2)
createLine( "h_ext_top_1", [ Conc_side_cover - 2.5*Reinf_dia_top, Rebar_position_top, Height_pilecap -
Conc_bot_cover - Reinf_dia_top * 2.5 ], [ (Anch_length / math. tan(Anch_angle)) + Conc_side_cover -
2.5*Reinf_dia_top, Rebar_position_top, Height_pilecap - Anch_length - Conc_bot_cover - Reinf_dia_top *
2.5 ] )
createLine( "v_ext_top_1", [ Rebar_position_top, Conc_side_cover - 2.5*Reinf_dia_top , Height_pilecap
- Conc_bot_cover - Reinf_dia_top*3.5], [ Rebar_position_top, (Anch_length / math. tan(Anch_angle)) +
Conc_side_cover - 2.5*Reinf_dia_top , Height_pilecap - Anch_length - Conc_bot_cover - Reinf_dia_top *
3.5 ] )
arrayCopy(["HR_top_1", "h_bend_top_1", "h_ext_top_1"], [0, dis_y_2 , 0], [0, 0, 0], [0, 0, 0],
No_top_reinf - 1)
arrayCopy(["VR_top_1", "vbend_top_1", "v_ext_top_1"], [dis_x_2, 0, 0], [0, 0, 0], [0, 0, 0],
No_top_reinf - 1)

```

```

#createLine( "Flank_x", [ Conc_side_cover, Conc_bot_cover , Rebar_position], [ Length_pilecap / 2 ,
Conc_bot_cover , Rebar_position] )

if Flank == 'Y':
    addSet(SHAPESET, "Shapes 1")
    rename(SHAPESET, "Shapes 1", "Flank")
    createline( "Flank_hor_1", [ Conc_side_cover -Flank_dia , Conc_bot_cover + Flank_dia * 0.5 ,
Rebar_position + Flank_dia ], [ Length_pilecap / 2 , Conc_bot_cover + Flank_dia * 0.5, Rebar_position
+ Flank_dia] )
    createline( "Flank_ver_1", [ Conc_bot_cover + Flank_dia * 0.5, Conc_side_cover - Flank_dia,
Rebar_position + Flank_dia], [ Conc_bot_cover + Reinf_dia_bottom * 0.5, Width_pilecap/2,
Rebar_position + Flank_dia] )
    createArc( "Flank_bend_1", [ Conc_side_cover -Flank_dia, Conc_side_cover -Flank_dia ,
Rebar_position + Flank_dia] , [ 0, 0, 1 ], [ -1, 0, 0 ], 1.5*Flank_dia, 0, pi/2 )
    arrayCopy(["Flank_hor_1", "Flank_ver_1", "Flank_bend_1"], [0, 0, Flank_dis], [0, 0, 0], [0, 0, 0],
No_flank - 1)

##### ASSIGN MATERIAL
###Concrete
addMaterial("Concrete_LE", "CONCR", "LEI", [])
setParameter("MATERIAL", "Concrete_LE", "LINEAR/ELASTI/YOUNG", Elin)
setParameter("MATERIAL", "Concrete_LE", "LINEAR/ELASTI/POISON", Poison)
setParameter("MATERIAL", "Concrete_LE", "LINEAR/MASS/DENSIT", Density)
assignMaterial("Concrete_LE", SHAPE, [ "Column" ])

addMaterial("Concrete_NL", "CONCR", "TSCR", [])
setParameter("MATERIAL", "Concrete_NL", "LINEAR/ELASTI/POISON", Poison)
setParameter("MATERIAL", "Concrete_NL", "LINEAR/MASS/DENSIT", Density)
setParameter("MATERIAL", "Concrete_NL", "MODTYP/TOTCRK", "ROTATE")
setParameter("MATERIAL", "Concrete_NL", "TENSIL/TENCRV", "HORDYK")
if Safety_factor == 'M':
    setParameter("MATERIAL", "Concrete_NL", "LINEAR/ELASTI/YOUNG", Ecm)
    setParameter("MATERIAL", "Concrete_NL", "TENSIL/TENSTR", fctm)
    setParameter("MATERIAL", "Concrete_NL", "TENSIL/GF1", Gf_m)
elif Safety_factor == 'K':
    setParameter("MATERIAL", "Concrete_NL", "LINEAR/ELASTI/YOUNG", Eck)
    setParameter("MATERIAL", "Concrete_NL", "TENSIL/TENSTR", fctk)
    setParameter("MATERIAL", "Concrete_NL", "TENSIL/GF1", Gf_k)
elif Safety_factor == 'D':
    setParameter("MATERIAL", "Concrete_NL", "LINEAR/ELASTI/YOUNG", Ecd)
    setParameter("MATERIAL", "Concrete_NL", "TENSIL/TENSTR", fctd)
    setParameter("MATERIAL", "Concrete_NL", "TENSIL/GF1", Gf_d)
setParameter("MATERIAL", "Concrete_NL", "TENSIL/POISRE/POIRED", "DAMAGE")
setParameter("MATERIAL", "Concrete_NL", "COMPRS/COMCRV", "PARABO")
if Safety_factor == 'M':
    setParameter("MATERIAL", "Concrete_NL", "COMPRS/COMSTR", fcm)
    setParameter("MATERIAL", "Concrete_NL", "COMPRS/GC", Gc_m)
elif Safety_factor == 'K':
    setParameter("MATERIAL", "Concrete_NL", "COMPRS/COMSTR", fck)
    setParameter("MATERIAL", "Concrete_NL", "COMPRS/GC", Gc_k)
elif Safety_factor == 'D':
    setParameter("MATERIAL", "Concrete_NL", "COMPRS/COMSTR", fcd)
    setParameter("MATERIAL", "Concrete_NL", "COMPRS/GC", Gc_d)
setParameter("MATERIAL", "Concrete_NL", "COMPRS/REDUCT/REDCRV", "VC1993")
setParameter("MATERIAL", "Concrete_NL", "COMPRS/REDUCT/REDMIN", 0.6)
if Res == 'Y':
    setParameter(MATERIAL, "Concrete_NL", "TENSIL/RESTST", Res_tens)
    setParameter(MATERIAL, "Concrete_NL", "COMPRS/RESCST", Res_comp)
    setParameter(MATERIAL, "Concrete_NL", "COMPRS/REDUCT/REDCRV", "NONE")
if Confinement == 'Y':
    setParameter("MATERIAL", "Concrete_NL", "COMPRS/CONFIN/CNFCRV", "VECCHI")
elif Confinement == 'N':
    setParameter(MATERIAL, "Concrete_NL", "COMPRS/CONFIN/CNFCRV", "NONE")
addGeometry( "Element geometry 6", "SOLID", "STRSOL", [ ] )
rename( GEOMET, "Element geometry 6", "geom_concrete" )
assignMaterial("Concrete_NL", SHAPE, [ "Pile cap" ])

setElementClassType( SHAPE, [ "Pile cap", "Column" ], "STRSOL" )
assignGeometry( "geom_concrete", SHAPE, [ "Pile cap", "Column" ] )

addMaterial( "rebar_embedded", "REINFO", "VMISES", [ ] )
setParameter( MATERIAL, "rebar_embedded", "LINEAR/ELASTI/YOUNG", Es )
setParameter( MATERIAL, "rebar_embedded", "PLASTI/YLDTYP", "KAPSIG" )

```

```

if Safety_factor == 'M':
    setParameter( MATERIAL, "rebar_embedded", "PLASTI/HARDI2/KAPSIG", [ 0, fym, e1_m, fum, e2_m, 0 ] )
elif Safety_factor == 'K':
    setParameter(MATERIAL, "rebar_embedded", "PLASTI/HARDI2/KAPSIG", [0, fyk, e1_k, fuk, e2_k, 0])
elif Safety_factor == 'D':
    setParameter(MATERIAL, "rebar_embedded", "PLASTI/HARDI2/KAPSIG", [0, fyd, e1_d, fud, e2_d, 0])

if Rebar == 'S':
    addMaterial("bot_rebar_bondslip", "REINFO", "REBOND", [])
    setParameter(MATERIAL, "bot_rebar_bondslip", "REBARS/ELASTI/YOUNG", Es)
    setParameter(MATERIAL, "bot_rebar_bondslip", "REBARS/POISON/POISON", Rebar_poison)
    setParameter(MATERIAL, "bot_rebar_bondslip", "REBARS/MASS/DENSIT", Rebar_density)
    setParameter(MATERIAL, "bot_rebar_bondslip", "REBARS/PLATYP", "VMISES")
    setParameter(MATERIAL, "bot_rebar_bondslip", "REBARS/PLASTI/TRESSH", "KAPSIG")
    setParameter(MATERIAL, "bot_rebar_bondslip", "REBARS/PLASTI/KAPSIG", [])
    if Safety_factor == 'M':
        setParameter( MATERIAL, "bot_rebar_bondslip", "REBARS/PLASTI/KAPSIG", [ 0, fym, e1_m, fum, e2_m,
0 ] )
    elif Safety_factor == 'K':
        setParameter(MATERIAL, "bot_rebar_bondslip", "REBARS/PLASTI/KAPSIG", [0, fyk, e1_k, fuk, e2_k,
0])
    elif Safety_factor == 'D':
        setParameter(MATERIAL, "bot_rebar_bondslip", "REBARS/PLASTI/KAPSIG", [0, fyd, e1_d, fud, e2_d,
0])
    setParameter(MATERIAL, "bot_rebar_bondslip", "RESLIP/DSNY", Norm_stiffness)
    setParameter(MATERIAL, "bot_rebar_bondslip", "RESLIP/DSSX", Shear_stiffness)
    setParameter(MATERIAL, "bot_rebar_bondslip", "RESLIP/SHFTYP", "BONDS4")
    if Safety_factor == 'M':
        setParameter(MATERIAL, "bot_rebar_bondslip", "RESLIP/BONDS4/SLPVAL", fcm-8e+6)
    elif Safety_factor == 'K':
        setParameter(MATERIAL, "bot_rebar_bondslip", "RESLIP/BONDS4/SLPVAL", fck - 8e+6)
    elif Safety_factor == 'D':
        setParameter(MATERIAL, "bot_rebar_bondslip", "RESLIP/BONDS4/SLPVAL", fcd - 8e+6)
    setParameter(MATERIAL, "bot_rebar_bondslip", "RESLIP/BONDS4/DIAMET", Reinf_dia_bottom)
    setParameter(MATERIAL, "bot_rebar_bondslip", "RESLIP/BONDS4/TAUFAC", 0.75)

    copy(MATERIAL, "bot_rebar_bondslip", "flank_rebar_bondslip")
    setParameter(MATERIAL, "flank_rebar_bondslip", "RESLIP/BONDS4/DIAMET", Flank_dia)

#Element data
if Rebar == 'S':
    addElementData( "Element data 1" )
    setParameter( DATA, "Element data 1", "./INTERF", [] )
    setParameter( DATA, "Element data 1", "INTERF", "BEAM" )

#Geometry
addGeometry( "Element geometry 1", "RELINE", "REBAR", [] )
rename( GEOMET, "Element geometry 1", "top_geom_embedded" )
setParameter(GEOMET, "top_geom_embedded", "REIEMB/RDITYP", "RCROSS")
setParameter(GEOMET, "top_geom_embedded", "REIEMB/CROSSE", Rebar_area_top)

if Rebar == 'E':
    addGeometry( "Element geometry 1", "RELINE", "REBAR", [] )
    rename( GEOMET, "Element geometry 1", "bot_geom_embedded" )
    setParameter(GEOMET, "bot_geom_embedded", "REIEMB/RDITYP", "RCROSS")
    setParameter(GEOMET, "bot_geom_embedded", "REIEMB/CROSSE", Rebar_area_bot)

    addGeometry( "Element geometry 1", "RELINE", "REBAR", [] )
    rename( GEOMET, "Element geometry 1", "flank_geom_embedded" )
    setParameter(GEOMET, "flank_geom_embedded", "REIEMB/RDITYP", "RCROSS")
    setParameter(GEOMET, "flank_geom_embedded", "REIEMB/CROSSE", Flank_area)

elif Rebar == 'S':
    addGeometry("Element geometry 1", "RELINE", "REBAR", [])
    rename(GEOMET, "Element geometry 1", "bot_geom_bondslip_x")
    setParameter(GEOMET, "bot_geom_bondslip_x", "REITYP", "REITRU")
    setParameter(GEOMET, "bot_geom_bondslip_x", "REITYP", "CIRBEA")
    setParameter(GEOMET, "bot_geom_bondslip_x", "CIRBEA/CIRCLE", Reinf_dia_bottom)
    setParameter(GEOMET, "bot_geom_bondslip_x", "ORIENT/ZAXIS", [0, 1, 0])

    copy(GEOMET, "bot_geom_bondslip_x", "bot_geom_bondslip_y")
    setParameter(GEOMET, "bot_geom_bondslip_y", "ORIENT/ZAXIS", [1, 0, 0])

    addGeometry("Element geometry 1", "RELINE", "REBAR", [])

```

```

rename(GEOMET, "Element geometry 1", "flank_geom_bondslip_x")
setParameter(GEOMET, "flank_geom_bondslip_x", "REITYP", "REITRU")
setParameter(GEOMET, "flank_geom_bondslip_x", "REITYP", "CIRBEA")
setParameter(GEOMET, "flank_geom_bondslip_x", "CIRBEA/CIRCLE", Flank_dia)
setParameter(GEOMET, "flank_geom_bondslip_x", "ORIENT/ZAXIS", [0, 1, 0])

copy(GEOMET, "flank_geom_bondslip_x", "flank_geom_bondslip_y")
setParameter(GEOMET, "flank_geom_bondslip_y", "ORIENT/ZAXIS", [1, 0, 0])

bot_rebar_list = []
for i in range(No_bot_reinf):
    j = i+1
    new_name = "HR_bot_{}".format(j)
    new_name_2 = "VR_bot_{}".format(j)
    new_name_3 = "h_bend_bot_{}".format(j)
    new_name_4 = "h_ext_bot_{}".format(j)
    new_name_5 = "v_ext_bot_{}".format(j)
    new_name_6 = "vbend_bot_{}".format(j)
    bot_rebar_list.append(new_name)
    bot_rebar_list.append(new_name_2)
    bot_rebar_list.append(new_name_3)
    bot_rebar_list.append(new_name_4)
    bot_rebar_list.append(new_name_5)
    bot_rebar_list.append(new_name_6)

top_rebar_list = []
for i in range(No_top_reinf):
    j = i+1
    new_name = "HR_top_{}".format(j)
    new_name_2 = "VR_top_{}".format(j)
    new_name_3 = "h_bend_top_{}".format(j)
    new_name_4 = "h_ext_top_{}".format(j)
    new_name_5 = "v_ext_top_{}".format(j)
    new_name_6 = "vbend_top_{}".format(j)
    top_rebar_list.append(new_name)
    top_rebar_list.append(new_name_2)
    top_rebar_list.append(new_name_3)
    top_rebar_list.append(new_name_4)
    top_rebar_list.append(new_name_5)
    top_rebar_list.append(new_name_6)

flank_rebar_list = []
for i in range(No_flank):
    j = i+1
    new_name = "Flank_hor_{}".format(j)
    new_name_2 = "Flank_ver_{}".format(j)
    new_name_3 = "Flank_bend_{}".format(j)
    flank_rebar_list.append(new_name)
    flank_rebar_list.append(new_name_2)
    flank_rebar_list.append(new_name_3)

convertToReinforcement(top_rebar_list)
assignMaterial("rebar_embedded", SHAPE, top_rebar_list)
assignGeometry("top_geom_embedded", SHAPE, top_rebar_list)
resetElementData(SHAPE, top_rebar_list)

if Rebar == 'E':
    convertToReinforcement(bot_rebar_list)
    assignMaterial("rebar_embedded", SHAPE, bot_rebar_list)
    assignGeometry("bot_geom_embedded", SHAPE, bot_rebar_list)
    resetElementData(SHAPE, bot_rebar_list)

    convertToReinforcement(flank_rebar_list)
    assignMaterial("rebar_embedded", SHAPE, flank_rebar_list)
    assignGeometry("flank_geom_embedded", SHAPE, flank_rebar_list)
    resetElementData(SHAPE, flank_rebar_list)

elif Rebar == 'S':
    convertToReinforcement( bot_rebar_list )
    assignMaterial( "bot_rebar_bondslip", SHAPE, bot_rebar_list )
    assignGeometry( "bot_geom_bondslip_x", SHAPE, bot_rebar_list )
    assignElementData("Element data 1", SHAPE, bot_rebar_list)

bot_rebar_list_2 = []

```

```

for i in range(No_bot_reinf):
    j = i + 1
    new_name = "VR_bot_{}".format(j)
    new_name_2 = "v_ext_bot_{}".format(j)
    new_name_3 = "vbend_bot_{}".format(j)
    bot_rebar_list_2.append(new_name)
    bot_rebar_list_2.append(new_name_2)
    bot_rebar_list_2.append(new_name_3)
assignGeometry("bot_geom_bondslip_y", SHAPE, bot_rebar_list_2)

convertToReinforcement( flank_rebar_list )
assignMaterial( "flank_rebar_bondslip", SHAPE, flank_rebar_list )
assignGeometry( "flank_geom_bondslip_x", SHAPE, flank_rebar_list )
assignElementData("Element data 1", SHAPE, flank_rebar_list)

flank_rebar_list_2 = []
for i in range(No_flank):
    j = i + 1
    new_name = "Flank_ver_{}".format(j)
    flank_rebar_list_2.append(new_name)
assignGeometry("bot_geom_bondslip_y", SHAPE, flank_rebar_list_2)

##Pile
addGeometry("Element geometry 1", "SOLID", "STRSOL", [])
rename(GEOMET, "Element geometry 1", "Steel_plate")
addMaterial( "Steel_plate", "MCSTEL", "ISOTRO", [] )
setParameter( MATERIAL, "Steel_plate", "LINEAR/ELASTI/YOUNG", E_plate )
setParameter( MATERIAL, "Steel_plate", "LINEAR/ELASTI/POISSON", Stl_pl_poisson )
setParameter( MATERIAL, "Steel_plate", "LINEAR/MASS/DENSIT", Stl_pl_density )
setElementClassType( SHAPE, [ "pile" ], "STRSOL")
assignMaterial( "Steel_plate", SHAPE, [ "pile" ] )
assignGeometry( "Steel_plate", SHAPE, [ "pile" ] )

##### CREATING TYING
createSurfaceTying( "Load Tying", "Load Tying" )
setParameter( GEOMETRYTYING, "Load Tying", "AXES", [ 1, 2 ] )
setParameter( GEOMETRYTYING, "Load Tying", "TRANSL", [ 0, 0, 1 ] )
setParameter( GEOMETRYTYING, "Load Tying", "ROTATI", [ 0, 0, 0 ] )
attachTo( GEOMETRYTYING, "Load Tying", "SLAVE", "Column", [[ Col_Dist_Left + Width_col/4,
Col_Dist_Bottom + Width_col/4, Height_col + Height_pilecap ] ] )
attachTo( GEOMETRYTYING, "Load Tying", "MASTER", "Column", [[ Length_pilecap/2, Width_pilecap/2,
Height_col + Height_pilecap ] ] )

##### BOUNDARY CONDITIONS
addSet( GEOMETRY SUPPORTSET, "Load Support" )
createPointSupport( "Load Support", "Load Support" )
setParameter( GEOMETRY SUPPORT, "Load Support", "AXES", [ 1, 2 ] )
setParameter( GEOMETRY SUPPORT, "Load Support", "TRANSL", [ 0, 0, 1 ] )
setParameter( GEOMETRY SUPPORT, "Load Support", "ROTATI", [ 0, 0, 0 ] )
attach( GEOMETRY SUPPORT, "Load Support", "Column", [[ Length_pilecap/2, Width_pilecap/2, Height_col +
Height_pilecap ] ] )

createPointSupport("BC_support", "BC_support")
setParameter(GEOMETRY SUPPORT, "BC_support", "AXES", [1, 2])
setParameter(GEOMETRY SUPPORT, "BC_support", "TRANSL", [0, 0, 1])
setParameter(GEOMETRY SUPPORT, "BC_support", "ROTATI", [0, 0, 0])
attach(GEOMETRY SUPPORT, "BC_support", "pile", [[Pile_Dist_Left, Pile_Dist_Bottom, -Stl_pl_thick ]])

addSet( GEOMETRY SUPPORTSET, "Symmetry" )
createSurfaceSupport( "Symmetry_Length", "Symmetry" )
setParameter( GEOMETRY SUPPORT, "Symmetry_Length", "AXES", [ 1, 2 ] )
setParameter( GEOMETRY SUPPORT, "Symmetry_Length", "TRANSL", [ 1, 0, 0 ] )
setParameter( GEOMETRY SUPPORT, "Symmetry_Length", "ROTATI", [ 0, 0, 0 ] )
attach( GEOMETRY SUPPORT, "Symmetry_Length", "Pile cap", [[ Length_pilecap/2, Width_pilecap/4,
Height_pilecap/2 ] ] )
attach( GEOMETRY SUPPORT, "Symmetry_Length", "Column", [[ Length_pilecap/2, (Width_pilecap/2 -
Length_col/4), Height_col/2 + Height_pilecap ] ] )
#attach( GEOMETRY SUPPORT, "Symmetry_Length", "Column", [[ Length_pilecap/2, (Width_pilecap/2 -
Col_rec_int), Height_col/2 + Height_pilecap ] ] )

createSurfaceSupport( "Symmetry_Width", "Symmetry" )
setParameter( GEOMETRY SUPPORT, "Symmetry_Width", "AXES", [ 1, 2 ] )
setParameter( GEOMETRY SUPPORT, "Symmetry_Width", "TRANSL", [ 0, 1, 0 ] )
setParameter( GEOMETRY SUPPORT, "Symmetry_Width", "ROTATI", [ 0, 0, 0 ] )

```

```

attach( GEOMETRY SUPPORT, "Symmetry_Width", "Pile cap", [[ Length_pilecap/4, Width_pilecap/2,
Height_pilecap/2 ] ] )
attach( GEOMETRY SUPPORT, "Symmetry_Width", "Column", [[ Length_pilecap/2 - Height_col/4,
Width_pilecap/2, Height_col/2 + Height_pilecap ] ] )
#attach( GEOMETRY SUPPORT, "Symmetry_Width", "Column", [[ Length_pilecap/2 - (Col_rec_int + 0.1),
Width_pilecap/2, Height_col/2 + Height_pilecap ] ] )

createPointSupport( "Symmetry_Rebar_Length", "Symmetry" )
setParameter( GEOMETRY SUPPORT, "Symmetry_Rebar_Length", "AXES", [ 1, 2 ] )
setParameter( GEOMETRY SUPPORT, "Symmetry_Rebar_Length", "TRANSL", [ 1, 0, 0 ] )
setParameter( GEOMETRY SUPPORT, "Symmetry_Rebar_Length", "ROTATI", [ 0, 0, 0 ] )
attach( GEOMETRY SUPPORT, "Symmetry_Rebar_Length", "HR_bot_1", [[ Length_pilecap/2, Rebar_position,
Conc_bot_cover ] ] )
attach( GEOMETRY SUPPORT, "Symmetry_Rebar_Length", "HR_bot_2", [[ Length_pilecap/2, Rebar_position +
dis_y_1, Conc_bot_cover ] ] )
attach( GEOMETRY SUPPORT, "Symmetry_Rebar_Length", "HR_bot_3", [[ Length_pilecap/2, Rebar_position +
2*dis_y_1, Conc_bot_cover ] ] )
attach( GEOMETRY SUPPORT, "Symmetry_Rebar_Length", "HR_bot_4", [[ Length_pilecap/2, Rebar_position +
3*dis_y_1, Conc_bot_cover ] ] )
attach( GEOMETRY SUPPORT, "Symmetry_Rebar_Length", "HR_bot_5", [[ Length_pilecap/2, Rebar_position +
4*dis_y_1, Conc_bot_cover ] ] )

createPointSupport( "Symmetry_Flank_Length", "Symmetry" )
setParameter( GEOMETRY SUPPORT, "Symmetry_Flank_Length", "AXES", [ 1, 2 ] )
setParameter( GEOMETRY SUPPORT, "Symmetry_Flank_Length", "TRANSL", [ 1, 0, 0 ] )
setParameter( GEOMETRY SUPPORT, "Symmetry_Flank_Length", "ROTATI", [ 0, 0, 0 ] )
attach( GEOMETRY SUPPORT, "Symmetry_Flank_Length", "Flank_hor_1", [[ Length_pilecap / 2 ,
Conc_bot_cover + Flank_dia * 0.5, Rebar_position + Flank_dia] ] )
attach( GEOMETRY SUPPORT, "Symmetry_Flank_Length", "Flank_hor_2", [[ Length_pilecap / 2 ,
Conc_bot_cover + Flank_dia * 0.5 + Flank_dis, Rebar_position + Flank_dia ] ] )
attach( GEOMETRY SUPPORT, "Symmetry_Flank_Length", "Flank_hor_3", [[ Length_pilecap / 2 ,
Conc_bot_cover + Flank_dia * 0.5 + 2*Flank_dis, Rebar_position + Flank_dia ] ] )
attach( GEOMETRY SUPPORT, "Symmetry_Flank_Length", "Flank_hor_4", [[ Length_pilecap / 2 ,
Conc_bot_cover + Flank_dia * 0.5 + 3*Flank_dis, Rebar_position + Flank_dia ] ] )
attach( GEOMETRY SUPPORT, "Symmetry_Flank_Length", "Flank_hor_5", [[ Length_pilecap / 2 ,
Conc_bot_cover + Flank_dia * 0.5 + 4*Flank_dis, Rebar_position + Flank_dia ] ] )

createPointSupport( "Symmetry_Rebar_Width", "Symmetry" )
setParameter( GEOMETRY SUPPORT, "Symmetry_Rebar_Width", "AXES", [ 1, 2 ] )
setParameter( GEOMETRY SUPPORT, "Symmetry_Rebar_Width", "TRANSL", [ 0, 1, 0 ] )
setParameter( GEOMETRY SUPPORT, "Symmetry_Rebar_Width", "ROTATI", [ 0, 0, 0 ] )
attach( GEOMETRY SUPPORT, "Symmetry_Rebar_Width", "VR_bot_1", [[ Rebar_position, Width_pilecap/2,
Conc_bot_cover + Reinf_dia_bottom ] ] )
attach( GEOMETRY SUPPORT, "Symmetry_Rebar_Width", "VR_bot_2", [[ Rebar_position + dis_x_1,
Width_pilecap/2, Conc_bot_cover + Reinf_dia_bottom ] ] )
attach( GEOMETRY SUPPORT, "Symmetry_Rebar_Width", "VR_bot_3", [[ Rebar_position + 2*dis_x_1,
Width_pilecap/2, Conc_bot_cover + Reinf_dia_bottom ] ] )
attach( GEOMETRY SUPPORT, "Symmetry_Rebar_Width", "VR_bot_4", [[ Rebar_position + 3*dis_x_1,
Width_pilecap/2, Conc_bot_cover + Reinf_dia_bottom ] ] )
attach( GEOMETRY SUPPORT, "Symmetry_Rebar_Width", "VR_bot_5", [[ Rebar_position + 4*dis_x_1,
Width_pilecap/2, Conc_bot_cover + Reinf_dia_bottom ] ] )

createPointSupport( "Symmetry_Flank_Width", "Symmetry" )
setParameter( GEOMETRY SUPPORT, "Symmetry_Flank_Width", "AXES", [ 1, 2 ] )
setParameter( GEOMETRY SUPPORT, "Symmetry_Flank_Width", "TRANSL", [ 0, 1, 0 ] )
setParameter( GEOMETRY SUPPORT, "Symmetry_Flank_Width", "ROTATI", [ 0, 0, 0 ] )
attach( GEOMETRY SUPPORT, "Symmetry_Flank_Width", "Flank_ver_1", [[ Conc_bot_cover + Reinf_dia_bottom
* 0.5, Width_pilecap/2, Rebar_position + Flank_dia] ] )
attach( GEOMETRY SUPPORT, "Symmetry_Flank_Width", "Flank_ver_2", [[ Conc_bot_cover + Reinf_dia_bottom
* 0.5 + Flank_dis, Width_pilecap/2, Rebar_position + Flank_dia] ] )
attach( GEOMETRY SUPPORT, "Symmetry_Flank_Width", "Flank_ver_3", [[ Conc_bot_cover + Reinf_dia_bottom
* 0.5 + 2*Flank_dis, Width_pilecap/2, Rebar_position + Flank_dia] ] )
attach( GEOMETRY SUPPORT, "Symmetry_Flank_Width", "Flank_ver_4", [[ Conc_bot_cover + Reinf_dia_bottom
* 0.5 + 3*Flank_dis, Width_pilecap/2, Rebar_position + Flank_dia] ] )
attach( GEOMETRY SUPPORT, "Symmetry_Flank_Width", "Flank_ver_5", [[ Conc_bot_cover + Reinf_dia_bottom
* 0.5 + 4*Flank_dis, Width_pilecap/2, Rebar_position + Flank_dia] ] )

##### ADD LOAD
addSet( GEOMETRY LOAD SET, "Displacement" )
createPointLoad( "Displacement", "Displacement" )
setParameter( GEOMETRY LOAD, "Displacement", "LODTYP", "DEFORM" )
setParameter( GEOMETRY LOAD, "Displacement", "DEFORM/SUPP", "Load Support" )
setParameter( GEOMETRY LOAD, "Displacement", "DEFORM/TR/VALUE", -0.001 )
setParameter( GEOMETRY LOAD, "Displacement", "DEFORM/TR/DIRECT", 3 )

```

```
attach( GEOMETRYLOAD, "Displacement", "Column", [[Length_pilecap/2, Width_pilecap/2, Height_col + Height_pilecap ] ] )
```

```
##### MESH
```

```
setElementSize( [ "Pile cap" , "Column"], Mesh_Size, -1, True )  
setMesherType( [ "Pile cap", "Column" ], "HEXQUAD" )  
clearMidSideNodeLocation( [ "Pile cap", "Column" ] )
```

```
##Pile 1
```

```
setEdgeMeshSeed( "Pile cap", [[ Pile_Dist_Left, Pile_Dist_Bottom + Int_rect_size, Height_pilecap ],[  
Pile_Dist_Left, Pile_Dist_Bottom + Int_rect_size, 0 ],[ Pile_Dist_Left - Int_rect_size,  
Pile_Dist_Bottom, Height_pilecap ],[ Pile_Dist_Left - Int_rect_size, Pile_Dist_Bottom, 0 ],[  
Pile_Dist_Left, Pile_Dist_Bottom - Int_rect_size, Height_pilecap ],[ Pile_Dist_Left, Pile_Dist_Bottom  
- Int_rect_size, 0 ],[ Pile_Dist_Left + Int_rect_size , Pile_Dist_Bottom, Height_pilecap  
],[Pile_Dist_Left + Int_rect_size, Pile_Dist_Bottom, 0 ],[ Pile_Dist_Left, Pile_Dist_Bottom +  
Ext_rect_size/2, Height_pilecap ],[ Pile_Dist_Left, Pile_Dist_Bottom + Ext_rect_size/2, 0 ],[  
Pile_Dist_Left - Ext_rect_size/2, Pile_Dist_Bottom, Height_pilecap ],[ Pile_Dist_Left -  
Ext_rect_size/2, Pile_Dist_Bottom, 0 ],[ Pile_Dist_Left, Pile_Dist_Bottom - Ext_rect_size/2,  
Height_pilecap ],[ Pile_Dist_Left, Pile_Dist_Bottom - Ext_rect_size/2, 0 ],[ Pile_Dist_Left +  
Ext_rect_size/2, Pile_Dist_Bottom , Height_pilecap ],[ Pile_Dist_Left + Ext_rect_size/2,  
Pile_Dist_Bottom , 0 ],[ Pile_Dist_Left - Int_rect_size/2, Pile_Dist_Bottom, Height_pilecap ],[  
Pile_Dist_Left, Pile_Dist_Bottom + Int_rect_size/2, Height_pilecap ],[ Pile_Dist_Left +  
Int_rect_size/2, Pile_Dist_Bottom, Height_pilecap ],[ Pile_Dist_Left, Pile_Dist_Bottom -  
Int_rect_size/2, Height_pilecap ],[ Pile_Dist_Left - Int_rect_size/2, Pile_Dist_Bottom, 0 ],[  
Pile_Dist_Left, Pile_Dist_Bottom + Int_rect_size/2, 0 ],[ Pile_Dist_Left + Int_rect_size/2,  
Pile_Dist_Bottom, 0 ],[ Pile_Dist_Left, Pile_Dist_Bottom - Int_rect_size/2, 0 ]], Mesh_no_pile )  
setEdgeMeshSeed( "Pile cap", [[ Pile_Dist_Left + (Radius_pile* math.cos(pi/4) + Int_rect_size/2)/2,  
Pile_Dist_Bottom + (Radius_pile* math.cos(pi/4) + Int_rect_size/2)/2, Height_pilecap ],[  
Pile_Dist_Left + (Radius_pile* math.cos(pi/4) + Int_rect_size/2)/2, Pile_Dist_Bottom + (Radius_pile*  
math.cos(pi/4) + Int_rect_size/2)/2, 0 ],[ Pile_Dist_Left - (Radius_pile* math.cos(pi/4) +  
Int_rect_size/2)/2, Pile_Dist_Bottom + (Radius_pile* math.cos(pi/4) + Int_rect_size/2)/2,  
Height_pilecap],[ Pile_Dist_Left - (Radius_pile* math.cos(pi/4) + Int_rect_size/2)/2, Pile_Dist_Bottom  
+ (Radius_pile* math.cos(pi/4) + Int_rect_size/2)/2, 0 ],[ Pile_Dist_Left - (Radius_pile*  
math.cos(pi/4) + Int_rect_size/2)/2, Pile_Dist_Bottom - (Radius_pile* math.cos(pi/4) +  
Int_rect_size/2)/2, Height_pilecap ],[ Pile_Dist_Left - (Radius_pile* math.cos(pi/4) +  
Int_rect_size/2)/2, Pile_Dist_Bottom - (Radius_pile* math.cos(pi/4) + Int_rect_size/2)/2, 0 ],[  
Pile_Dist_Left + (Radius_pile* math.cos(pi/4) + Int_rect_size/2)/2, Pile_Dist_Bottom - (Radius_pile*  
math.cos(pi/4) + Int_rect_size/2)/2, Height_pilecap ],[ Pile_Dist_Left + (Radius_pile* math.cos(pi/4)  
+ Int_rect_size/2)/2, Pile_Dist_Bottom - (Radius_pile* math.cos(pi/4) + Int_rect_size/2)/2, 0 ],[  
Pile_Dist_Left + (Radius_pile* math.cos(pi/4) + Ext_rect_size/2)/2, Pile_Dist_Bottom + (Radius_pile*  
math.cos(pi/4) + Ext_rect_size/2)/2, Height_pilecap ],[ Pile_Dist_Left + (Radius_pile* math.cos(pi/4)  
+ Ext_rect_size/2)/2, Pile_Dist_Bottom + (Radius_pile * math.cos(pi/4) + Ext_rect_size/2)/2, 0 ],[  
Pile_Dist_Left - (Radius_pile * math.cos(pi/4) + Ext_rect_size/2)/2, Pile_Dist_Bottom + (Radius_pile*  
math.cos(pi/4) + Ext_rect_size/2)/2, Height_pilecap ],[ Pile_Dist_Left + (Radius_pile * math.cos(pi/4)  
+ Ext_rect_size/2)/2, Pile_Dist_Bottom + (Radius_pile* math.cos(pi/4) + Ext_rect_size/2)/2, 0 ],[  
Pile_Dist_Left - (Radius_pile * math.cos(pi/4) + Ext_rect_size/2)/2, Pile_Dist_Bottom - (Radius_pile *  
math.cos(pi/4) + Ext_rect_size/2)/2, Height_pilecap ],[ Pile_Dist_Left - (Radius_pile * math.cos(pi/4)  
+ Ext_rect_size/2)/2, Pile_Dist_Bottom - (Radius_pile * math.cos(pi/4) + Ext_rect_size/2)/2, 0 ],[  
Pile_Dist_Left + (Radius_pile* math.cos(pi/4) + Ext_rect_size/2)/2, Pile_Dist_Bottom - (Radius_pile *  
math.cos(pi/4) + Ext_rect_size/2)/2, Height_pilecap ],[ Pile_Dist_Left + (Radius_pile* math.cos(pi/4)  
+ Ext_rect_size/2)/2, Pile_Dist_Bottom - (Radius_pile * math.cos(pi/4) + Ext_rect_size/2)/2, 0 ]],  
Mesh_no_pile_dia )
```

```
generateMesh( [] )  
hideView( "GEOM" )  
showView( "MESH" )
```

D. Cost calculation



Project: POEREN
Opdrachtgever: ABT
Onderwerp: Elementspecificatie directe kosten

Berekening directe kosten van POEREN

Re-bar percentage: 1.83%

Geometry: 2.6m x 2.6m x 1.4m

											50Eur/hr	
16.13.01	16.13.01	16.13.01	16.13.01	16.13.01	16.13.01	16.13.01	16.13.01	16.13.01	16.13.01	16.13.01	16.13.01	
	Aantal, l x b x h	variabel	berekend	vf	hoev. eenheid	manuur	mat.	o.a.	tot. arbeid	tot. mat.	tot. o.a.	totaal
	bruglat werkvloer en egaliseren		6.76		6.8 m2	0.15	1.00		1.0	7		57
	werkvloer beton C12/15		0.41		0.4 m3	3.00	95.00		1.2	39		99
	randkist		14.56		14.6 m2	0.80	12.00		11.6	175		757
	beton C20/25 incl. 3% stortverl.		9.75		9.7 m3	0.60	95.00		5.8	926		1,218
	wap.incl. 3% knipverl.	42 kg/ m3	409.02		409.0 kg			1.49			610	610
	blokjes/olie/draadnagel		7.80		7.8 m2	0.05	5.00		0.4	39		59
	nazorg beton		9.46		9.5 m3	0.02	1.00		0.2	9		19
	in te storten onderdelen		2.00		2.0 st	0.15	6.50		0.3	13		28
16.13.01	Poeren				\$ 2,848.33 /e.h	20.61	1,207.53	610.46	20.6	1,208	610	2,848
											Bedrag per m3 beton	\$ 292.20

Geometry: 2.6m x 2.6m x 1.3m

16.13.01	16.13.01	16.13.01	16.13.01	16.13.01	16.13.01	16.13.01	16.13.01	16.13.01	16.13.01	16.13.01	16.13.01	
	Aantal, l x b x h	variabel	berekend	vf	hoev. eenheid	manuur	mat.	o.a.	tot. arbeid	tot. mat.	tot. o.a.	totaal
	bruglat werkvloer en egaliseren		6.76		6.8 m2	0.15	1.00		1.0	7		57
	werkvloer beton C12/15		0.41		0.4 m3	3.00	95.00		1.2	39		99
	randkist		13.52		13.5 m2	0.80	12.00		10.8	162		703
	beton C20/25 incl. 3% stortverl.		9.05		9.1 m3	0.60	95.00		5.4	860		1,131
	wap.incl. 3% knipverl.	44 kg/ m3	398.27		398.3 kg			1.49			594	594
	blokjes/olie/draadnagel		7.80		7.8 m2	0.05	5.00		0.4	39		59
	nazorg beton		8.79		8.8 m3	0.02	1.00		0.2	9		18
	in te storten onderdelen		2.00		2.0 st	0.15	6.50		0.3	13		28
16.13.01	Poeren				\$ 2,689.82 /e.h	19.34	1,128.23	594.42	19.3	1,128	594	2,690
											Bedrag per m3 beton	\$ 297.16

Geometry: 2.6m x 2.6m x 1.2m

16.13.01	16.13.01	16.13.01	16.13.01	16.13.01	16.13.01	16.13.01	16.13.01	16.13.01	16.13.01	16.13.01	16.13.01	
	Aantal, l x b x h	variabel	berekend	vf	hoev. eenheid	manuur	mat.	o.a.	tot. arbeid	tot. mat.	tot. o.a.	totaal
	bruglat werkvloer en egaliseren		6.76		6.8 m2	0.15	1.00		1.0	7		57
	werkvloer beton C12/15		0.41		0.4 m3	3.00	95.00		1.2	39		99
	randkist		12.48		12.5 m2	0.80	12.00		10.0	150		649
	beton C20/25 incl. 3% stortverl.		8.36		8.4 m3	0.60	95.00		5.0	794		1,044
	wap.incl. 3% knipverl.	45 kg/ m3	375.99		376.0 kg			1.49			561	561
	blokjes/olie/draadnagel		7.80		7.8 m2	0.05	5.00		0.4	39		59
	nazorg beton		8.11		8.1 m3	0.02	1.00		0.2	8		16
	in te storten onderdelen		2.00		2.0 st	0.15	6.50		0.3	13		28
16.13.01	Poeren				\$ 2,514.10 /e.h	18.08	1,048.92	561.16	18.1	1,049	561	2,514
											Bedrag per m3 beton	\$ 300.90



Project: POEREN
Opdrachtgever: ABT
Onderwerp: Elementspecificatie directe kosten

Re-bar percentage: 2.36%

16.13.01	Poeren	berekend	vf	hoev. eenheid	manuur	mat.	o.a.	tot. arbeid	tot. mat.	tot. o.a.	totaal
Aantal, l x b x h		variabel		1.0 ST	2.60	2.60	1.40				
	bruglat werkvloer en egaliseren		6.76	6.8 m2	0.15	1.00		1.0	7		57
	werkvloer beton C12/15		0.41	0.4 m3	3.00	95.00		1.2	39		99
	randkist		14.56	14.6 m2	0.80	12.00		11.6	175		757
	beton C20/25 incl. 3% stortverl.		9.75	9.7 m3	0.60	95.00		5.8	926		1,218
	wap.incl. 3% knipverl.	41 kg/ m3	396.06	396.1 kg			1.49			591	591
	blokjes/olie/draadnagel		7.80	7.8 m2	0.05	5.00		0.4	39		59
	nazorg beton		9.46	9.5 m3	0.02	1.00		0.2	9		19
	in te storten onderdelen		2.00	2.0 st	0.15	6.50		0.3	13		28
16.13.01	Poeren			\$ 2,828.98 /e.h	20.61	1,207.53	591.11	20.6	1,208	591	2,829
										Bedrag per m3 beton	\$ 290.21

Re-bar percentage: 2.09%

16.13.01	Poeren	berekend	vf	hoev. eenheid	manuur	mat.	o.a.	tot. arbeid	tot. mat.	tot. o.a.	totaal
Aantal, l x b x h		variabel		1.0 ST	2.60	2.60	1.40				
	bruglat werkvloer en egaliseren		6.76	6.8 m2	0.15	1.00		1.0	7		57
	werkvloer beton C12/15		0.41	0.4 m3	3.00	95.00		1.2	39		99
	randkist		14.56	14.6 m2	0.80	12.00		11.6	175		757
	beton C20/25 incl. 3% stortverl.		9.75	9.7 m3	0.60	95.00		5.8	926		1,218
	wap.incl. 3% knipverl.	38 kg/ m3	370.13	370.1 kg			1.49			552	552
	blokjes/olie/draadnagel		7.80	7.8 m2	0.05	5.00		0.4	39		59
	nazorg beton		9.46	9.5 m3	0.02	1.00		0.2	9		19
	in te storten onderdelen		2.00	2.0 st	0.15	6.50		0.3	13		28
16.13.01	Poeren			\$ 2,790.28 /e.h	20.61	1,207.53	552.41	20.6	1,208	552	2,790
										Bedrag per m3 beton	\$ 286.24

Re-bar percentage: 1.83%

16.13.01	Poeren	berekend	vf	hoev. eenheid	manuur	mat.	o.a.	tot. arbeid	tot. mat.	tot. o.a.	totaal
Aantal, l x b x h		variabel		1.0 ST	2.60	2.60	1.40				
	bruglat werkvloer en egaliseren		6.76	6.8 m2	0.15	1.00		1.0	7		57
	werkvloer beton C12/15 (platform - 5cm)		0.41	0.4 m3	3.00	95.00		1.2	39		99
	randkist (formwork)		14.56	14.6 m2	0.80	12.00		11.6	175		757
	beton C20/25 incl. 3% stortverl.		9.75	9.7 m3	0.60	95.00		5.8	926		1,218
	wap.incl. 3% knipverl. (reinforcement)	35 kg/ m3	344.20	344.2 kg			1.49			514	514
	blokjes/olie/draadnagel (spacers/oil/)		7.80	7.8 m2	0.05	5.00		0.4	39		59
	nazorg beton (curing)		9.46	9.5 m3	0.02	1.00		0.2	9		19
	in te storten onderdelen (anchors)		2.00	2.0 st	0.15	6.50		0.3	13		28
16.13.01	Poeren			\$ 2,751.58 /e.h	20.61	1,207.53	513.71	20.6	1,208	514	2,752
										Bedrag per m3 beton	\$ 282.27